Tome 18 *Août 1980* Numero 3

うみ

La mer

昭和 55 年 8 月

日 仏 海 洋 学 会

La Société franco-japonaise
d'océanographie
Tokyo, Japon

日 仏 海 洋 学 会

投 稿 規 定

1. 報文の投稿者は本会会員に限る。
2. 原稿は簡潔にわかりやすく書き，図表を含めて印刷ページで**10ページ**以内を原則とする。原稿（正**1通，副1通**）は，（〒101）東京都千代田区神田駿河台2-3　日仏会館内　日仏海洋学会編集委員会宛に送ること。
3. 編集委員会は，事情により原稿の字句の加除訂正を行うことがある。
4. 論文（欧文，和文とも）には必ず約200語の欧文（原則として仏語）の要旨をつけること。欧文論文には欧文の要旨のほかに必ず約500字の和文の要旨をつけること。
5. 図及び表は必要なもののみに限る。図はそのまま版下になるように縮尺を考慮して鮮明に黒インクで書き，論文の図及び表には必ず英文（又は仏文）の説明をつけること。
6. 初校は原則として著者が行う。
7. 報文には1編につき50部の別刷を無料で著者に進呈する。これ以上の部数に対しては，実費（送料を含む）を著者が負担する。

RECOMMANDATIONS A L'USAGE DES AUTEURS

1. Les auteurs doivent être des membres de la Société franco-japonaise d'océanographie.
2. Les notes ne peuvent dépasser dix pages. Les manuscrits à deux exemplaires, dactylographiés sur papier fort, doivent être envoyés au Comité de rédaction de la Société frananco-japonaise d'océanographie, c/o Maison franco-japonaise, 2-3, Kanda Surugadai, Chiyoda-ku, Tokyo, 101 Japon.
3. Le Comité de rédaction se réserve le droit d'apporter, le cas échéant, des modifications mineuses aux manuscrits ainsi que de demander aux auteurs de les corriger.
4. Das résumés en langue japonaise ou langue française sont obligatoires.
5. Les figures au trait seront tracées à l'encre de Chine noire sur papier blanc ou sur calque. Les légendes des figures et des tableaux sont indispensables.
6. Les premières épreuves seront corrigées, en principe, par les auteurs.
7. Un tirage á part des articles en cinquante exemplaires est offert gratuitement aux auteurs. Ceux qui en désirent un plus grand nombre peuvent les faire établir à leurs frais.

La mer (Bulletin de la Société franco-japonaise d'océanographie)
Tome 18, N° 3, pp. 93 à 103, Août 1980

Some Detailed Consideration on Crest Profiles of Ship Waves*

Masahide TOMINAGA**

Résumé: Pour étudier l'onde de navire, on souvent se rencontre à l'intégrale de la forme

$$\zeta=\int_0^T \psi(t)e^{i\chi(t)}dt,$$

où ζ est la dénivellation de la surface d'eau et le temps T est très grand. Selon de la méthode conventionnelle de KELVIN, on développe la fonction $\chi(t)$ en série comme

$$\chi(t)=\chi(t_0)+\frac{\ddot{\chi}_0(t_0)}{2!}(t-t_0)^2+O(t-t_0)^3,$$

où $\dot{\chi}(t_0)=0$ à l'exception du cas où $\ddot{\chi}(t_0)$ est aussi nulle. Â l'étude présente, on ajoute le terme de troisième ordre $\chi(t_0)(t-t_0)^3/6!$ à la série ci-dessus.

Il résulte que la forme de la courbe de crête d'onde se déforme particulièrement quand on considère l'onde en profondeur infinie. Généralement, on peut dire qu'il est suffisant de tenir le terme de la série ci-dessus seulement jusqu'au $\ddot{\chi}(t_0)(t-t_0)^2/2!$.

1. Introduction

There have been abundant theoretical and experimental works on ship wave problem since KELVIN (1887) has given the first complete theoretical discussion. Detailed explanation of this problem appears in "Water Waves" by STOKER (1957) in the case of deep water.

Essentially, the problem of ship waves can be dealt with the so-called CAUCHY-POISSON waves of which an impulse source travels on the surface of water. If we assume the motion is irrotational, the velocity potential of wave motion due to a point source given on the origin $x=0$, $y=0$ is expressed by

$$\phi(r,\ z;\ t)=e^{i\sigma t}e^{mz}J_0(mr), \qquad (1.1)$$

where x and y are horizontal coordinates, $r^2=x^2+y^2$, and z is taken positive upward, σ is the frequency, m the wave number along r axis and t the time. $J_0(mr)$ is the Bessel function of zero order. Therefore, at a fixed point $\mathrm{P}(x,y)$ on the water surface, the elevation due to a travelling impulse is given by

$$\zeta(r,t)=K\int G(m)J_0(mr)\sin[tf(m)]dm. \qquad (1.2)$$

However, resultant effect of the moving impulse given by (1.2) during time T on the surface of water is expressed by

$$\zeta=\int_0^T \psi(t)e^{i\chi(t)}dt. \qquad (1.3)$$

Generally, T is large, and it is conventional to use Kelvin's stationary method to evaluate (1.3) asymptotically. In this case, the stationary point t_0 is given from $\dot{\chi}(t)=0$, then we use the Taylor's expansion

$$\chi(t)=\chi(t_0)+\frac{\ddot{\chi}_0}{2!}(t-t_0)^2+\frac{\dddot{\chi}_0}{3!}(t-t_0)^3+O(t-t_0)^4 \qquad (1.4)$$

where $\ddot{\chi}_0$ etc. denote $(d^2\chi/dt^2)_{t=t_0}$ etc. Generally, we hold terms of the above series up to the second on the assumption that $|\ddot{\chi}_0{}^2/\dddot{\chi}_0{}^3|$ is small compared with 1 except near the point where $\ddot{\chi}_0$ vanishes.

The crest profile (or in other words profile of constant phase of the waves) of waves produced by a moving disturbance in a deep water

* Received March 1, 1980

** Department of Marine Civil Engineering, Faculty of Engineering, Kagoshima University, Koorimoto 1-21-40, Kagoshima, 890 Japan
Present address: Nishimotomachi 2-11-44, Kokubunji-shi, Tokyo, 185 Japan

is well-known, especially when a disturbance travels with uniform velccity along a straight line. In the case of shallow water, a parameter denoted by $\delta=U/\sqrt{gh}$ where U is velocity of a disturbance, h the depth of water and g the acceleration of gravity, stipulates a form of the crest profile. These profiles for any value of δ were given early by HAVELOCK (LAMB, Hydrodynamics, p. 440, foot note).

The purpose of the present study is to elucidate how the crest profile deforms when the term $\dddot{\chi}_0(t-t_0)^3/3!$ in (1.4) is taken into consideration.

2. Fundamental analysis

When an impulsive force $I(x,y)$ is imposed on the surface of water with uniform depth h, the velocity potential ϕ due to CAUCHY-POISSON wave motion is expressed by

$$\begin{aligned}\phi(x,y,z)&=-\frac{1}{2\pi\rho}\int_{-\infty}^{\infty}J_0(mr)\cos(\sqrt{gm\tanh mh}\,t)\\&\times\frac{\cosh m(h+z)}{\cosh mh}\bar{I}(m)mdm\end{aligned}\tag{2.1}$$

where $m^2=k^2+l^2$ and $\bar{I}(m)$ is the FOURIER transformation of $I(m)$ such as

$$\bar{I}(m)=\int_{-\infty}^{\infty}\int_{-\infty}^{\infty}e^{i(kx+ly)}I(x,y)dxdy\,,\tag{2.2}$$

and its inverse transformation is given by

$$\begin{aligned}I(x,y)&=\frac{1}{4\pi^2}\int_{-\infty}^{\infty}dl\int_{-\infty}^{\infty}e^{-i(kx+ly)}\bar{I}(k,l)dkdl\\&=\frac{1}{4\pi^2}\int_0^{2\pi}\int_{-\infty}^{\infty}e^{-imr\sin(\theta+\Delta)}\bar{I}(m)mdmd\theta\\&=\frac{1}{2\pi}\int_{-\infty}^{\infty}J_0(mr)\bar{I}(m)mdm\end{aligned}\tag{2.3}$$

where $k=m\cos\theta$, $l=m\sin\theta$ and $\Delta=\tan^{-1}y/x$. Invoking the formula

$$J_0(mr)\sim\sqrt{\frac{2}{\pi mr}}\cos\left(mr-\frac{\pi}{4}\right)$$

for large mr and $\zeta_t=\phi_z(z=0)$ we have

$$\begin{aligned}\zeta&=\frac{1}{2\pi\rho\sqrt{g}}\int_{-\infty}^{\infty}m\bar{I}(m)\left(\frac{\tanh mh}{2\pi r}\right)^{1/2}\\&\times\sin\left[tf(m)+\frac{\pi}{4}\right]dm\end{aligned}\tag{2.4}$$

from (2.1), where

$$f(m)=(gm\tanh mh)^{1/2}-\frac{mr}{t}.\tag{2.5}$$

When t is large, the Kelvin's stationary method is applied to (2.4) giving

$$\begin{aligned}\zeta&\sim-\frac{m_0I(m_0)}{2\pi\rho\sqrt{g}}\left[\frac{\tanh m_0h}{rt|f''(m_0)|}\right]^{1/2}\\&\times\sin\left[tf(m_0)+\frac{\pi}{4}+\frac{\pi}{4}\operatorname{sgn}f''(m_0)\right]\end{aligned}\tag{2.6}$$

where m_0 is a root of $f'(m)=0$ or introducing $\mu=m_0h$ which is a root of

$$G(\mu)\equiv\frac{\tanh\mu+\mu\operatorname{sech}^2\mu}{2\sqrt{\mu\tanh\mu}}=\frac{r}{\sqrt{gh}\,t}.\tag{2.7}$$

Moreover, we also have

$$\begin{aligned}f(m_0)&=\sqrt{\frac{g}{h}}\left(\sqrt{\mu}\tanh\mu-\frac{r\mu}{\sqrt{gh}\,t}\right),\\f''(m_0)&=h\frac{d}{d\mu}[\sqrt{gh}\,G(\mu)]=g^{1/2}h^{3/2}\frac{dG}{d\mu}\\&=-\frac{g^{1/2}h^{3/2}}{4\mu}\left(\frac{\tanh\mu}{\mu}\right)^{1/2}J(\mu)<0,\end{aligned}$$

where

$$\left.\begin{aligned}&\frac{dG}{d\mu}=-\frac{1}{4\mu}\left(\frac{\tanh\mu}{\mu}\right)^{1/2}J(\mu),\\&\text{and}\\&J(\mu)=1+2\mu^2+2\mu\tanh\mu\\&\quad-3(\mu\tanh\mu)^2-\frac{2\mu}{\tanh\mu}+\left(\frac{\mu}{\tanh\mu}\right)^2.\end{aligned}\right\}\tag{2.8}$$

Abbreviated form of (2.6) is therefore given by

$$\zeta\sim-\frac{\bar{I}}{\pi\rho}\Psi_1(\mu)\sin\left[t\sqrt{\frac{g}{h}}H(\mu)\right],\tag{2.9}$$

with

$$\left.\begin{aligned}\Psi_1(\mu)&=\frac{\mu^{7/4}\tanh^{1/4}\mu}{g^{3/4}h^{7/4}[rtJ(\mu)]^{1/2}}\\H(\mu)&=\sqrt{\mu}\tanh\mu-r\mu/\sqrt{gh}\,t.\end{aligned}\right\}\tag{2.10}$$

If the above disturbance travels along the x-axis from Q to O in Fig. 1 with the uniform velocity U in time interval T, the resultant influences of moving disturbance is expressed

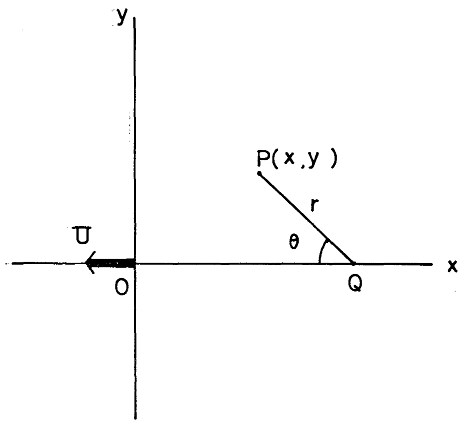

Fig. 1. A point disturbance travels from Q to O with uniform velocity U. P is on the surface of water behind the disturbance.

by integrating (2.9) with respect to t and multplying g/U as

$$\zeta\sim -Im\int_0^T \Psi(\mu)\exp i\chi(t)\,dt\,, \qquad (2.11)$$

where

$$\chi(t)=\sqrt{\frac{g}{h}}\,tH(\mu)\,,$$

$$\Psi(\mu)=\frac{g}{\pi\rho U}\Psi_1(\mu)=\frac{\bar{I}g^{1/4}\mu^{7/4}\tanh^{1/4}\mu}{\pi\rho Uh^{7/4}[rtJ(\mu)]^{1/2}},$$

and μ is time-varying.

Let again apply Kelvin's stationary method to (2.11) for large t. A stationary value of $\chi(t)$ is given by $\dot\chi(t_0)=0$ or

$$\dot\chi(t)=\sqrt{\frac{g}{h}}\left[H(\mu)+t\frac{\partial}{\partial t}H(\mu)\right]=0.$$

Invoking the relation

$$\frac{\partial}{\partial t}H(\mu)=-\mu\frac{\dot r t-r}{\sqrt{gh}t^2},$$

we get

$$\dot\chi(t)=\sqrt{\frac{g}{h}}(\sqrt{\mu\tanh\mu}-\delta\mu\cos\theta)=0,^{*} \qquad (2.12)$$

where $\delta=U/\sqrt{gh}$. Then, from (2.7) we have

* To derive (2.12) we notice (2.7) and $\dot r=U\cos\theta$.

$$\left.\begin{aligned} &t_0=r/\sqrt{gh}G(\mu),\\ &\tanh\mu/\mu=\delta^2\cos^2\theta.^{**}\end{aligned}\right\} \qquad (2.13)$$

Thus, if we retain the term $(t-t_0)^3\dddot\chi_0/3!$ in (1.4), the asymptotic evaluation of (2.11) is given by

$$\zeta\sim Im2\pi\left(\frac{2}{|\dddot\chi_0|}\right)^{1/3}\Psi(t_0)\mathrm{Ai}\left[-\left(\frac{\ddot\chi_0}{2^{1/3}\dddot\chi_0^{2/3}}\right)^2\right]$$
$$\times\exp i\left(\chi_0+\frac{\ddot\chi_0^3}{3\dddot\chi_0^2}\right), \qquad (2.14)$$

where

$$\chi_0=\chi(t_0)=\frac{r\mu}{h}\left[\frac{\delta\cos\theta}{G(\mu)}-1\right],$$

t_0 being the function of μ satisfying (2.13). See Appendix I. $\mathrm{Ai}(-w)$ is the Airy's function defined by

$$\mathrm{Ai}(-w)=\frac{1}{\pi}\int_0^\infty\cos\left(\frac{\tau^3}{3}-w\tau\right)d\tau, \qquad (2.15)$$

with

$$w=(\ddot\chi_0/2^{1/3}\dddot\chi_0^{2/3})^2.$$

The evaluations of $\ddot\chi_0$ and $\dddot\chi_0$ are cumbersome, however, the results are summerized below (see Appendix II):

$$\left.\begin{aligned} \ddot\chi_0&=-\frac{\mu U^2}{hr}E(\mu)\,,\\ \dddot\chi_0&=\frac{g^{3/2}h^{1/2}\mu^{3/2}}{r^2J(\mu)\tanh^{1/2}\mu}D(\mu)\,,\end{aligned}\right\} \qquad (2.16)$$

$$E(\mu)=\sin^2\theta$$
$$-\frac{4G(\mu)\cos\theta}{\delta J(\mu)}\left(1-\frac{G}{\delta\cos\theta}\right)^2, \qquad (2.17)$$

$$D(\mu)=12G^2(\mu)\Delta_1^2+3G(\mu)J(\mu)\left(\frac{\tanh\mu}{\mu}\right)^{1/2}\Delta_2$$
$$-16QG^2(\mu)\Delta_1^3-12G(\mu)\Delta_1\Delta_2$$
$$+\left(\frac{\tanh\mu}{\mu}\right)^{1/2}J(\mu)\Delta_3, \qquad (2.18)$$

$$\left.\begin{aligned} \Delta_1&=\delta\cos\theta-G(\mu)\\ \Delta_2&=\delta^2\sin^2\theta+2\delta G(\mu)\cos\theta-2G^2(\mu)\\ \Delta_3&=\delta^3\sin\theta\cos\theta(2+\cos\theta)+3\delta^2G(\mu)\\ &\times\sin^2\theta+6\delta G^2(\mu)\cos\theta-6G^3(\mu)\end{aligned}\right\} \qquad (2.19)$$

** In the case of deep water waves we have $\tanh\mu\approx1$, $\mu\approx1/\delta\cos\theta$ and $G(\mu)\approx1/2\sqrt{\mu}$ giving $t_0=2r/U\cos\theta$.

$$Q=\frac{\mu^{1/2}}{J(\mu)\tanh^{1/2}\mu}-\frac{\mu^{3/2}}{2\tanh^{1/2}\mu}$$

$$\times\left[J(\mu)\frac{d}{d\mu}\left(\frac{\tanh\mu}{\mu}\right)+\frac{\tanh\mu}{\mu}\frac{dJ}{d\mu}\right]. \quad (2.20)$$

Therefore, w (positive) is given by

$$w=\left(\frac{|\chi_0|^3}{2\ddot{\chi}_0{}^2}\right)^{2/3}=\left(\frac{\delta^8\cos^2\theta J^2E^3r\mu}{2hD^2}\right)^{2/3}$$

$$=\left(\frac{3r\mu}{2h}|\varepsilon|\right)^{2/3} \quad (2.21)$$

with

$$\varepsilon=\delta^8\cos^2\theta J^2E^3/3D^2. \quad (2.22)$$

The elevation is now expressed by modified equation (2.14), namely

$$\zeta\sim-\left(\frac{16}{rDJ^{1/2}}\right)^{1/3}\frac{I\mu^{5/4}G^{1/2}\tanh^{5/12}\mu}{\rho Uh^{5/3}}$$

$$\times Ai(-w)\sin\left(\chi_0+\frac{2}{3}w^{3/2}sgn\ddot{\chi}_0\right). \quad (2.23)$$

The phase of sine in this equation is transformed to

$$\chi_0+\frac{2}{3}w^{3/2}=\frac{r\mu}{h}\left(\frac{\delta\cos\theta}{G}-1-\varepsilon\right). \quad (2.24)$$

In the case of deep waves ($\mu\gg1$, $\tanh\mu\approx1$, $\delta\to0$) some of the above quantities reduce to

$$G\sim\frac{\delta\cos\theta}{2},\ J\sim1,\ \Delta_1=\mu\sim\frac{\delta\cos\theta}{2},$$

$$\Delta_2\sim\delta^2\left(1-\frac{\cos^2\theta}{2}\right),$$

$$\Delta_3\sim\delta^3\left\{\sin\theta\cos\theta(2+\cos\theta)+\frac{3}{4}\cos\theta(2-\cos^2)\right\},$$

$$Q\sim\frac{1}{\delta\cos\theta}+\frac{\delta\cos\theta}{2},$$

then,

$$\left.\begin{aligned}&D(\mu)\sim\frac{\delta^2\cos^2\theta}{4}\bar{D}(\theta),\ (\delta\to0)\\&\bar{D}(\theta)=\cos^2\theta+4\sin\theta(2+\cos\theta),\\&E\sim1-\frac{3}{2}\cos^2\theta,\\&\varepsilon\sim\frac{16}{3\bar{D}^2(\theta)\cos^2\theta}\left(1-\frac{3}{2}\cos^2\theta\right)^3.\end{aligned}\right\} \quad (2.25)$$

$$\chi_0+\frac{2}{3}w^{3/2}\sim m_0r(1-\varepsilon),$$

$$m_0=\frac{g}{U^2\cos^2\theta}.$$

In this case, the second equation of (2.16) reduces to

$$\ddot{\chi}_0=\frac{g^{3/2}h^{1/2}\mu^{3/2}}{r^2J(\mu)\tanh^{1/2}\mu}\sim\frac{g^{3/2}h^{1/2}\mu^{3/2}}{r^2}\cdot$$

$$\times\frac{\delta^2\cos^2\theta}{4}\bar{D}(\theta)=\frac{m^{3/2}U^4}{4r^2g^{1/2}}\bar{D}(\theta). \quad (2.26)$$

$\bar{D}(\theta)$ or $\ddot{\chi}_0$ never vanishes for $0\leqq\theta\leqq\pi/2$. In general (shallow water), $\ddot{\chi}_0$ also never vanishes,

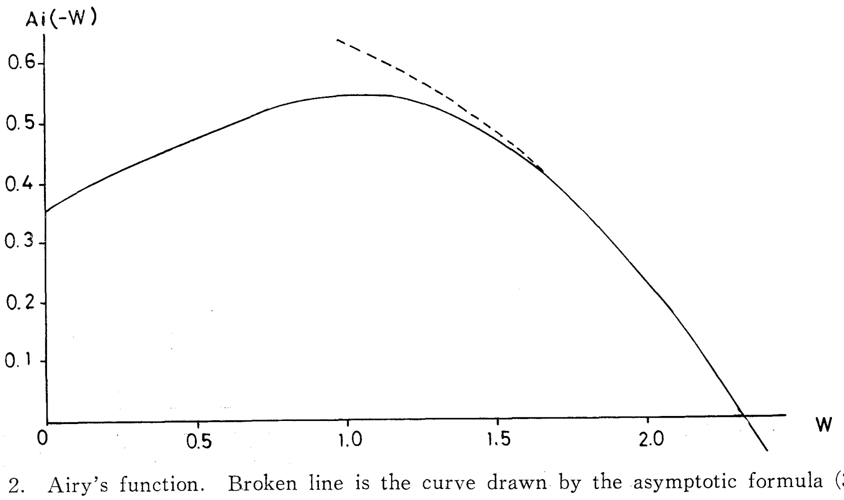

Fig. 2. Airy's function. Broken line is the curve drawn by the asymptotic formula (3.2).

therefore mathematically it is not reasonable to neglect completely the term $\dddot{\chi}_0(t-t_0)^3/3!$ in the series (1.4).

3. Crest profiles

Let us consider the last two factors in the right-hand side of (2.14) or (2.23):

$$F(w)=\mathrm{Ai}(-w)\sin\left(\chi_0+\frac{2}{3}w^{3/2}\right). \quad (3.1)$$

Airy's function can be asymptotically evaluated when actually w is larger than almost 1.7 (see Fig. 2, error is only less than 1.68 %) by

$$\mathrm{Ai}(-w)\sim\frac{1}{\sqrt{\pi}w^{1/4}}\left[\sin\left(\frac{2}{3}w^{3/2}+\frac{\pi}{4}\right)\sum_{\kappa=0}^{\infty}(-1)^{\kappa}\times c_{2\kappa}\left(\frac{2}{3}w^{3/2}\right)^{-2\kappa}-\cos\left(\frac{2}{3}w^{3/2}+\frac{\pi}{4}\right)\times\sum_{\kappa=0}^{\infty}(-1)^{\kappa}c_{2\kappa+1}\left(\frac{2}{3}w^{3/2}\right)^{-2\kappa-1}\right]^{*},$$

where

$$c_{\kappa}=\frac{(2\kappa+1)(2\kappa+3)\ldots(6\kappa-1)}{216^{\kappa}\kappa!}$$

or

$$\mathrm{Ai}(-w)\sim\frac{1}{\sqrt{\pi}w^{1/4}}\left(b_1^2+\frac{b_2^2}{w^3}\right)^{1/2}\times\sin\left(\frac{2}{3}w^{3/2}+\frac{\pi}{4}-\tan^{-1}\frac{b_2}{b_1w^{3/2}}\right), \quad (3.2)$$

where

$$b_1=1-\frac{0.08354}{w^3}+\frac{0.29185}{w^6}-\ldots,$$

$$b_2=0.10416\left(1-\frac{1.23095}{w^3}+\frac{8.46423}{w^6}-\ldots\right).$$

Therefore, from (2.14) we get

$$\zeta\sim2\sqrt{\pi}\left(\frac{2}{\dddot{\chi}_0}\right)^{1/3}\frac{\phi(\mu)}{w^{1/4}}\left(b_1^2+\frac{b_2^2}{w^2}\right)^{1/2}\times\sin\left(\chi_0+\mathrm{sng}\,\chi_0\cdot\frac{2}{3}w^{3/2}\right)\times\sin\left(\frac{2}{3}w^{3/2}+\frac{\pi}{4}-\tan^{-1}\frac{b_2}{b_1w^{3/2}}\right), \quad (3.3)$$

or using (2.21) and putting $p=\tan^{-1}(b^2/b_1w^{3/2})$, the above expression can be transformed to

$$\zeta\sim\left(\frac{2\pi}{|\ddot{\chi}_0|}\right)^{1/2}\phi(\mu)\left(b_1^2+\frac{b_2^2}{w^2}\right)^{1/2}\times\begin{cases}\cos\left[\frac{r\mu}{h}\left(\frac{\delta\cos\theta}{G}-1\right)+\frac{\pi}{4}-p\right]\\ \cos\left[\frac{r\mu}{h}\left(\frac{\delta\cos\theta}{G}-1\right)+\frac{3\pi}{4}+p\right]\end{cases}$$
$$+\left(\frac{2\pi}{|\ddot{\chi}_0|}\right)^{1/2}\phi(\mu)\left(b_1^2+\frac{b_2^2}{w^2}\right)^{1/2}\times\begin{cases}\cos\left[\frac{r\mu}{h}\left(\frac{\delta\cos\theta}{G}-1-2\varepsilon\right)+\frac{\pi}{4}-p\right]\\ \cos\left[\frac{r\mu}{h}\left(\frac{\delta\cos\theta}{G}-1-2\varepsilon\right)+\frac{3\pi}{4}+p\right],\end{cases} \quad (3.4)$$

according as $\ddot{\chi}_0>0$ or $<0(\varepsilon\lesssim0)$. Namely, when w is large, waves consist of two systems.

The constant phases of four terms in (3.4) can be defined as

$$\left.\begin{aligned}&\frac{r\mu}{h}\left(\frac{\delta\cos\theta}{G}-1\right)\pm p=\frac{ga_1^{\pm}}{U^2},\\ \text{and}\quad&\\ &\frac{r\mu}{h}\left(\frac{\delta\cos\theta}{G}-1-2\varepsilon\right)\pm p=\frac{ga_2^{\pm}}{U^2},\end{aligned}\right\} \quad (3.5)$$

where $a_1^{\pm}$ and $a_2^{\pm}$ have dimension of length. If we consider the crests, a's are given by

$$\frac{ga^{\pm}}{U^2}=\frac{8N-3}{4}\pi,\ \frac{8N-1}{4}\pi;\ N=1,2,\ldots \quad (3.6)$$

The profiles of the crests are defined by

$$\left.\begin{aligned}x&=Ut_0-r\cos\theta,\\ y&=r\sin\theta\end{aligned}\right\} \quad (3.7)$$

as shown in Fig. 1 where t_0 is given by (2.13) as the function of θ, and r's are solved from (3.5) giving

$$r=\frac{a_1^{\pm}}{2\delta^2\mu\left(\frac{\delta\cos\theta}{G}-1\right)}\times\{1+\sqrt{1\mp f_1^{\pm}(\theta)}\}, \quad (3.8)$$

from the first equation, and

* ABRAMOWITZ and STEGUN (1965): Handbook of Mathematical Functions. Dover Edition, p. 448.

$$r=\frac{a_2^{\pm}}{2\delta^2\mu\left(\dfrac{\delta\cos\theta}{G}-1-2\varepsilon\right)}\times\{1+\sqrt{1\pm f_2^{\pm}(\theta)}\}, \quad (3.9)$$

from the second equation, where the relation

$$p=\frac{b_2}{b_1 w^{3/2}}=\frac{2b_2 h}{3b_1\mu|\varepsilon|r}$$

is used and

$$f_1^{\pm}(\theta)=\frac{8b_2}{3b_1|\varepsilon|}\left(\frac{\delta\cos\theta}{G}-1\right)\left(\frac{U^2}{ga_1^{\pm}}\right)^2,$$
$$f_2^{\pm}(\theta)=\frac{8b_2}{3b_1|\varepsilon|}\left(\frac{\delta\cos\theta}{G}-1-2\varepsilon\right)\left(\frac{U^2}{ga_2^{\pm}}\right)^2. \quad (3.10)$$

Upon substituting (3.8) or (3.9) in (3.7), the profile of the first wave system in (3.4) is given by

$$\left.\begin{aligned} x&=\frac{a_1^{\pm}(\delta-G\cos\theta)}{\delta^2\mu(\delta\cos\theta-G)}\cdot\frac{1+\sqrt{1\mp f_1^{\pm}(\theta)}}{2},\\ y&=\frac{a_1^{\pm}G\sin\theta}{\delta^2\mu(\delta\cos\theta-G)}\cdot\frac{1+\sqrt{1\mp f_1^{\pm}(\theta)}}{2},\end{aligned}\right\} \quad (3.11)$$

for $\ddot{\chi}_0\gtrless 0(\varepsilon\lesseqgtr 0)$, that of the second wave system in (3.4) is given by

$$\left.\begin{aligned} x&=\frac{a_2^{\pm}(\delta-G\cos\theta)}{\delta^2\mu[\delta\cos\theta-G(1+2\varepsilon)]}\times\frac{1+\sqrt{1\mp f_2^{\pm}(\theta)}}{2},\\ y&=\frac{a_2^{\pm}G\sin\theta}{\delta^2\mu[\delta\cos\theta-G(1+2\varepsilon)]}\times\frac{1+\sqrt{1\mp f_2^{\pm}(\theta)}}{2},\end{aligned}\right\} \quad (3.12)$$

for $\ddot{\chi}_0\gtrless 0$. For the crest, we have $ga_2^{+}/U^2=(8N-1)\pi/4$ and $ga_2^{-}/U^2=(8N-3)\pi/4$ for $\ddot{\chi}_0>0$ and $\ddot{\chi}_0<0$, respectively.

When w is not large, the Airy's function does not oscillate, therefore, the constant phase of (2.23) is expressed by

$$\chi_0\pm\frac{2}{3}w^{3/2}=\frac{\mu r}{h}\left(\frac{\delta\cos\theta}{G}-1-\varepsilon\right)=\frac{ga}{U^2}, \quad (3.13)$$

the crest phase being given by $ga/U^2=(4N-1)\cdot\pi/2$, $N=1,2,\ldots$. By means of the same procedure as we derived (3.12), the crest curve when w is not large is given by

$$x=r\left(\frac{\delta}{G}-\cos\theta\right)=\frac{a(\delta-G\cos\theta)}{\delta^2\mu[\delta\cos\theta-G(1+\varepsilon)]},$$
$$y=r\sin\theta=\frac{aG\sin\theta}{\delta^2\mu[\delta\cos\theta-G(1+\varepsilon)]}. \quad (3.14)$$

4. Examples of the crest curve

[1] *Deep waves*

Using $\mu\sim\delta\cos\theta/2$, we have

$$r=\frac{a^{\pm}\cos^2\theta}{1-\varepsilon} \quad (w \text{ is not large, } |\varepsilon|<1)$$

from (3.13), therefore, (3.13) reduces to

$$\left.\begin{aligned} x&=\frac{a(2\cos\theta-\cos^3\theta)}{1-\varepsilon},\\ y&=\frac{a(\sin\theta-\sin^3\theta)}{1-\varepsilon}.\end{aligned}\right\} \quad (4.1)$$

If we neglect the terms subsequent to the second of the right-hand side of (4.1), equations of (4.1) reduce to the classical formulae dropping $1-\varepsilon$ from the denominator. However, this does not mean that $\varepsilon=0$ for any value of θ between 0° and 90°, because as we can seen from (2.21), neglect of $\ddot{\chi}_0$ corresponds to $\varepsilon\to\infty$ which occurs

Table 1. Values of ε and w: $ga^{+}/U^2=(4N-1)\cdot\pi/2$ for small value of w, $ga_1^{+}/U^2=(8N-3)\cdot\pi/4$ for large w. This table gives values for $N=1$.

$\theta°$	ε	$w=\left(\frac{9\pi}{4}\left\|\frac{\varepsilon}{1-\varepsilon}\right\|\right)^{2/3}$ (w small)	$w=\left(\frac{15\pi}{8}\left\|\frac{\varepsilon}{1-\varepsilon}\right\|\right)^{2/3}$ (w large)
0	−0.667		1.770
5	−0.151	0.950	
10	−0.056	0.520	
20	−0.0086	0.154	
35.26	0	0	
45	0.0025	0.0068	
60	0.0656	0.574	
70	0.322		1.985
75	0.749		6.760
76.55	1.000		
80	2.087		5.038
90	∞		3.262

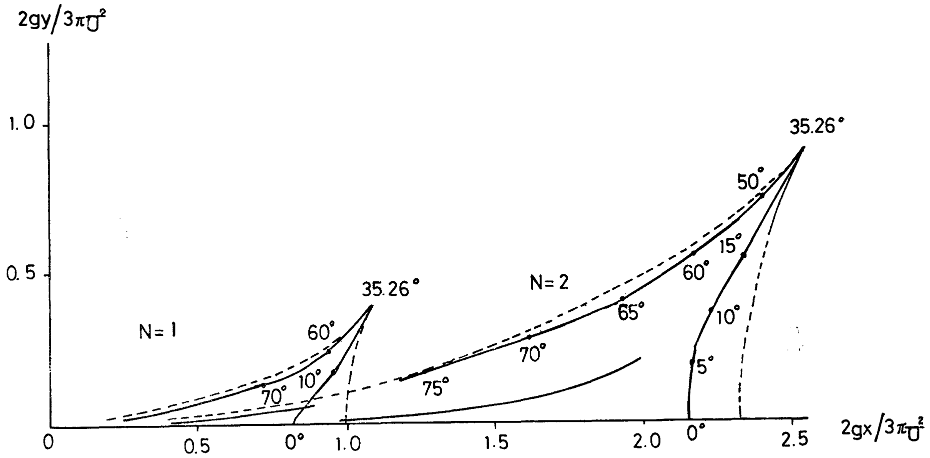

Fig. 3. Crest curves of ship wave in deep water for the first and second crests. Note the second branch of curves running near along the abscissa. Broken lines are classical crest curves drawn by the formulae (4.1) from which ε is dropped. Numbers annexed to curves are the value of θ in degree.

only when $\theta=90°$. The values of ε along the crest of deep waves is given by the fourth expression of (2.25) which are tabulated in Table 1.

Fig. 3 gives the profiles of deep ship waves for $N=1$ (the closest crest to the disturbance source) and $N=2$: the value of a for Nth crest is given by

$$a^{(N)}=\frac{(4N-1)\pi U^2}{2g}, \tag{4.2}$$

then, the unit of the abscissa and ordinate in Fig. 3 is $a=a^{(1)}=3\pi U^2/2g$, and $a^{(2)}/a=7/3$, respectively. The distance of any two successive crests is then given by

$$a^{(N+1)}-a^{(N)}=\frac{2\pi U^2}{g}$$

along the x-axis.

For the comparison, the classical curves depicted from the formulae

$$\left.\begin{aligned} x&=a(2\cos\theta-\cos^3\theta) \\ y&=a(\sin\theta-\sin^3\theta) \end{aligned}\right\} \tag{4.3}$$

which are derived on the assumption that the terms smaller than $(t-t_0)^3\dddot{\chi}_0/3!$ in (1.4) are omitted, are given in Fig. 3 with broken lines. The deformation of the curve is somewhat remarkable when θ is smaller than 20°. Position of the cusps ($\theta=35.26°$, or $\ddot{\chi}_0=0$) in the present detailed computation is the same with that due to the classical computation.

For about $\theta>70°(\ddot{\chi}_0>0)$ w becomes large, then the following equations can be got from (3.11) and (3.12) applying for deep water case:

$$\left.\begin{aligned} x&=a_1^{+}(2\cos\theta-\cos^3\theta)\frac{1+\sqrt{1-f_1(\theta)}}{2}, \\ y&=a_1^{+}(\sin\theta-\sin^3\theta)\frac{1+\sqrt{1-f_1(\theta)}}{2}, \\ f_1(\theta)&=\frac{8b_2}{3b_1|\varepsilon|}\left[\frac{4}{(8N-3)\pi}\right]^2, N=1,2,\ldots \end{aligned}\right\} \tag{4.4}$$

for the main wave system and

$$\left.\begin{aligned} x&=\frac{a_2^{+}(2\cos\theta-\cos^3\theta)}{1-2\varepsilon}\cdot \\ &\quad\times\frac{1+\sqrt{1-f_2(\theta)}}{2}, \\ y&=\frac{a_2^{+}(\sin\theta-\sin^3\theta)}{1-2\varepsilon}\cdot \\ &\quad\times\frac{1+\sqrt{1-f_2(\theta)}}{2}, \\ f_2(\theta)&=\frac{8b_2(1-2|\varepsilon|)}{3b_1|\varepsilon|}\left[\frac{4}{(8N-1)\pi}\right]^2, \\ &\qquad N=1,\ 2,\ \ldots \end{aligned}\right\} \tag{4.5}$$

for the second wave system.

From (3.6) we have

$$a_1^{(N)}=\frac{(8N-3)\pi U^2}{4g},\quad a_2^{(N)}=\frac{(8N-1)\pi U^2}{4g} \tag{4.6}$$

where + signs are dropped and $a_1^{(N)}$ and $a_2^{(N)}$ mean amplitude of Nth crest of the first and the second wave system, respectively. Ratios of $a_1^{(N)}$ and $a_2^{(N)}$ to a are given by

$$\frac{a_1^{(N)}}{a}=\frac{8N-3}{6},\quad \frac{a_2^{(N)}}{a}=\frac{8N-1}{6}. \tag{4.7}$$

The second crests for $N=1$ and 2 are drawn in Fig. 3 running along the x-axis.

[2] *Shallow waves*

According as $\delta=U/\sqrt{gh}$ approaches to 1, the crest curves extend widely, namely, angle of the sector within which the curves exist increases from $2\times 19.47°$ (deep, $\delta=0$) to, for example, $2\times 46.09°$ ($\delta=0.95$).

For the case where δ is larger than 1, a crest curve has no cusp, extending from the point of source to infinity as shown in Fig. 5 for $\delta=1.2$. The shape of the curve is almost the same with the classical one, except when $37°<\theta<40°$ where two curves separate slightly. The values of w are small in this interval (for example $w<0.254$ for $\theta<36.88°$), therefore, there are no two systems of waves represented by (3.11) and (3.12).

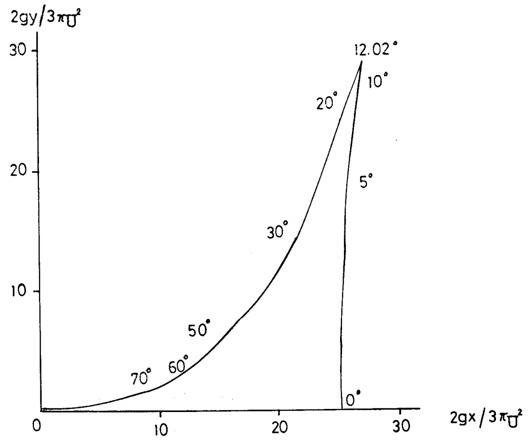

Fig. 4. Crest curve of shallow ship wave ($\delta=U/\sqrt{gh}=0.95$) for nineth crest ($N=9$). The curve is almost the same with the classical one.

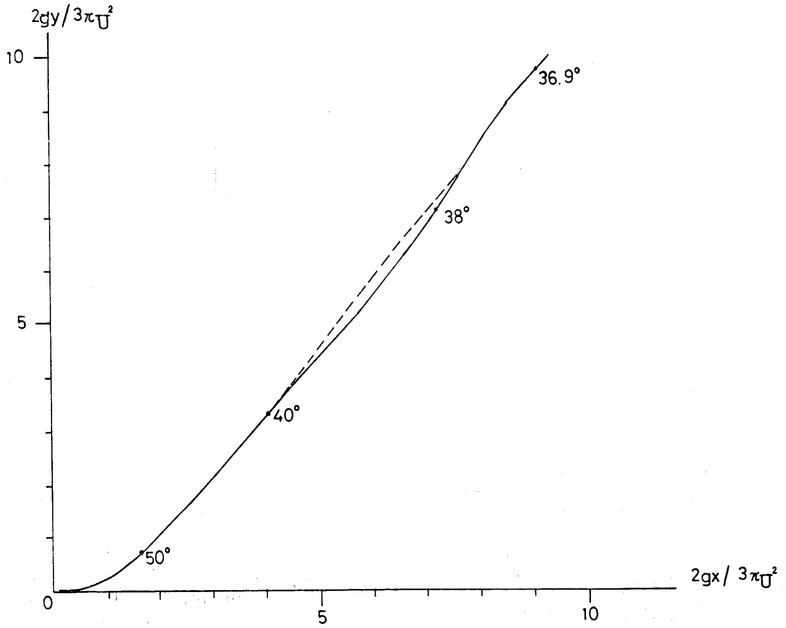

Fig. 5. Crest curve of shallow ship wave for $\delta=1.2$. Broken line indicates the slightly shifted part of classical curve.

5. Conclusions

Ship waves generating in the rear of a moving ship (a pressure impulse with infinite small horizontal scale) are represented by (1.3) in version of linear theory. The expansion of the function $\chi(t)$ included in the integrand of (1.3) around the stationary value $t=t_0$ is given by (1.4).

Conventionally, the terms of (1.4) are taken to $\ddot{\chi}_0(t-t_0)^2/2!$ except when $\ddot{\chi}_0=0$, but in the present discussion the term $\dddot{\chi}_0(t-t_0)^3/3!$ is also considered. After cumbersome calculations, the elevation due to waves are represented by (2.23), only when $\delta=U/\sqrt{gh}<1$. The latter (3.12) disappears if we neglect $\dddot{\chi}_0$.

The shape of the crest profiles somewhat differs from the classical one when $\delta=0$ or the water is deep, but slightly differs when the water is shallow ($\delta<1$). For $\delta>1$, the shape substantially does not change.

Appendix I. Proof of (1.2)

Upon substituting (1.4) in (1.3) and putting $\beta=\ddot{\chi}_0$, $\gamma=\dddot{\chi}_0$ we have for $T\to\infty$

$$\zeta=\phi(t_0)\exp i\left(\chi_0+\frac{\beta^3}{3\gamma^2}\right)$$
$$\times\int_{-t_0+\beta/\gamma}^{\infty}\exp i\left(\frac{\gamma}{6}\xi^3-\frac{\beta^2}{2\gamma}\xi\right)d\xi, \quad (1)$$

where $\xi=t-t_0+\beta/\gamma$. If the main contribution of the integral of (1) concentrates near t_0 (large), or $\xi=\beta/\gamma$, the lower limit of the integral can be substituted by $-\infty$ with small error, so that

$$\int_{-\infty}^{\infty}\exp i\left(\frac{\gamma\xi^3}{6}-\frac{\beta^2}{2\gamma}\xi\right)d\xi$$
$$=2\int_0^{\infty}\cos\left(\frac{\gamma\xi^3}{6}-\frac{\beta^2\xi}{2\gamma}\right)d\xi$$
$$=2\pi\left(\frac{2}{\gamma}\right)^{1/3}\mathrm{Ai}\left[-\left(\frac{\beta^3}{2\gamma^2}\right)^{2/3}\right]. \quad (2)$$

Substitution of (2) in (1) gives (2.14).

Appendix II. Derivations of $\ddot{\chi}_0$ and $\dddot{\chi}_0$

Comparing $\chi(t)$ on the exponential function of (1.3) and the argument of sine in (2.9), we have

$$\chi(t)=t\sqrt{\frac{g}{h}}H(\mu), \quad (3)$$

where μ is a root of (2.7) and $H(\mu)$ is given by (2.10). Then, we get

$$\dot{\chi}(t)=\sqrt{\frac{g}{h}}\left[H(\mu)+t\dot{H}(\mu)\right] \quad (4)$$

and differentiating $H(\mu)$ with respect to t we have

$$\dot{H}(\mu)=\left[G(\mu)-\frac{r}{\sqrt{gh}\,t}\right]\dot{\mu}-\mu\frac{\dot{r}t-r}{\sqrt{gh}\,t^2}$$
$$=-\mu\frac{\dot{r}t-r}{\sqrt{gh}\,t^2}, \quad (5)$$

where (2.7) is taken into consideration. Further differentiation of (5) with respect to t gives

$$\ddot{H}(\mu)=-\frac{\dot{\mu}}{\sqrt{gh}}\left(\frac{\dot{r}}{t}-\frac{r}{t^2}\right)$$
$$-\frac{\mu}{\sqrt{gh}}\left(\frac{\ddot{r}}{t}-\frac{2\dot{r}}{t^2}+\frac{2r}{t^3}\right). \quad (6)$$

Differentiating (2.7) with respect to t we have

$$\dot{\mu}=\frac{1}{\sqrt{gh}\,G'(\mu)}\left(\frac{\dot{r}}{t}-\frac{r}{t^2}\right), \quad (7)$$

$G'(\mu)$ being given by (2.8). From (4) we have

$$\ddot{\chi}(t)=\sqrt{\frac{g}{h}}\left[2\dot{H}(\mu)+t\ddot{H}(\mu)\right]. \quad (8)$$

Substituting (5) and (7) into (8), putting $t=t_0=r/\sqrt{gh}\,G(\mu)$ and using $\dot{r}=U\cos\theta$, $\ddot{r}=U^2\sin^2\theta/r$ and $\tanh\mu/\mu=\delta^2\cos^2\theta$, (8) reduces to

$$\ddot{\chi}_0=-\frac{\mu U^2}{hr}\left[\sin^2\theta-\frac{4G(\mu)\cos\theta}{\delta J(\mu)}\right.$$
$$\left.\times\left(1-\frac{G}{\delta\cos\theta}\right)^2\right]=-\frac{\mu U^2}{hr}E(\mu). \quad (9)$$

Next, differentiating (7) with respect to t we have

$$\dddot{\chi}=\sqrt{\frac{g}{h}}(3\ddot{H}+t\dddot{H}), \quad (10)$$

where

$$\dddot{H}(\mu)=-\frac{1}{\sqrt{gh}}\frac{d}{dt}\left[\dot{\mu}\left(\frac{\dot{r}}{t}-\frac{r}{t^2}\right)\right]-\frac{1}{\sqrt{gh}}\frac{d}{dt}\left[\mu\left(\frac{\ddot{r}}{t}-\frac{2\dot{r}}{t^2}+\frac{2r}{t^3}\right)\right]. \quad (11)$$

$\ddot{\mu}$ is derived from (7) giving

$$\ddot{\mu}=-\frac{4}{\sqrt{gh}}\dot{\mu}\frac{d}{d\mu}\left[\left(\frac{\mu}{T^{1/2}J}\right)\left(\frac{\dot{r}}{t}-\frac{r}{t^2}\right)\right]$$
$$=-\frac{4}{\sqrt{gh}}\left[\dot{\mu}\left\{\frac{1}{T^{1/2}J}-\frac{\mu}{TJ^2}\times\left(\frac{\dot{T}J}{2T^{1/2}}+T^{1/2}\dot{J}\right)\right\}\left(\frac{\dot{r}}{t}-\frac{r}{t^2}\right)+\frac{\mu}{T^{1/2}J}\left(\frac{\ddot{r}}{t}-\frac{2\dot{r}}{t^2}+\frac{2r}{t^2}\right)\right],$$

where $T=\tanh\mu/\mu$ and using (7) we have

$$\ddot{\mu}=\frac{4\mu}{(gh)^{1/2}T^{1/2}J}\times\left[\frac{4Q}{(gh)^{1/2}}\left(\frac{\dot{r}}{t}-\frac{r}{t^2}\right)^2-\frac{\ddot{r}}{t}+\frac{2\dot{r}}{t^2}-\frac{2r}{t^3}\right], \quad (12)$$

where

$$Q=\frac{1}{T^{1/2}J}-\frac{\mu(\dot{T}J+T\dot{J})}{2T^{3/2}J^2}.$$

For $t=t_0$, we can calculate following formulae:

$$T=\frac{\tanh\mu}{\mu}=\delta^2\cos^2\theta,$$

$$\dot{T}=\frac{1}{\mu}(1-T-\mu^2T^2),$$

$$G=\frac{1}{2T^{1/2}}(1+T-\mu^2T^2),$$

$$\frac{dG}{d\mu}=-\frac{T^{1/2}J}{4\mu},$$

$$J=4\mu^2T-(1-T-\mu^2T^2)(T^{-1}-T^{-2}-3\mu^2),$$

$$\dot{J}=4\mu(1+T-3\mu^2T^2)+2\mu(1-T-\mu^2T^2)\times\left(1-3\mu^2T+\frac{1}{\mu^2T^2}-\frac{1}{\mu^2T^3}\right).$$

From (11)* we get for $t=t_0$

$$\dddot{H}_0{}^*=-\frac{16\mu Q}{(gh)^{3/2}T^{1/2}J}P_1{}^3+\frac{12\mu}{ghT^{1/2}J}P_1P_2-\frac{\mu}{(gh)^{1/2}}P_3 \quad (13)$$

where

$$P_1=\frac{ghG}{r}\Delta_1,\ P_2=-\frac{(gh)^{3/2}G}{r^2}\Delta_2,$$

$$P_3=-\frac{(gh)^2G}{r^3}\Delta_3,$$

Δ_1, Δ_2 and Δ_3 being given by (2.18). Finally we have

$$\ddot{\chi}_0=\left(\frac{g}{h}\right)^{1/2}(3\ddot{H}_0+t_0\dddot{H}_0)$$
$$=\left(\frac{g}{h}\right)^{1/2}\left[\frac{12gh\mu G^2}{r^2T^{1/2}J}\Delta_1{}^2+\frac{3gh\mu G}{r^2}\Delta_2-\frac{16gh\mu G^2Q}{r^2T^{1/2}J}\Delta_1{}^3-\frac{12gh\mu G}{r^2T^{1/2}J}\Delta_1\Delta_2+\frac{gh\mu}{r^2}\Delta_3\right]$$
$$\equiv\frac{g^{3/2}h^{1/2}}{r^2T^{1/2}J}D(\mu),$$

where Q is given by (2.20).

References

KELVIN, L. (1887): On the waves produced by a single pulse in water of any depth or in a dispersive medium. Proc. Roy. Soc. London A, 42: 80-85.

LAMB, H. (1916): On wave patterns due to a travelling disturbance. Phil. Mag. (6) Vol. XXXI.

STOKER, J. J., (1957): Water Waves. Interscience Publishers Inc. pp. 219-243.

* Suffices 0 are used in the sense that the independent variable t is equal to t_0 in any function. $\dot{\theta}=-U\sin\theta/r$, $\ddot{\theta}=U^2\sin 2\theta/r^2$ and $\dddot{r}=-U^3\sin 2\theta(2+\cos\theta)/2r^2$.

船舶波の形状に関する一考察

冨　永　政　英

要旨: 船舶の進行してゆく後面に生ずる波については，いまさら新しい問題ではないが，普通船を点源のインパルスと仮定し，直線に沿って等速度で進むとき，水面の昇降は（1.3）のような形の積分で表わされる．船のごく近くを除いて（1.3）を計算するときケルビンの停留法を使う．その際函数 $\chi(t)$ を停留点 $\chi'(t)=0$ の根 t_0 の近くで(1.4)のように展開して右辺第２項までをとる．しかし一般に $\ddot{\chi}(t_0)$ に比し $\dddot{\chi}(t_0)$ の項は必ずしも小さくないので $|\ddot{\chi}_0{}^3/\dddot{\chi}_0{}^2|$ の影響を考慮して波形を求めると（3.4）のように２系の波が現れる．浅水の影響は $\delta=U/\sqrt{gh}$ なるパラメーターできまるが，深い波 $(\delta=0)$ のときは $\ddot{\chi}_0$ までとどめた古典理論のときといくらか異なった波形になる．浅いときは $\dddot{\chi}_0$ を考える効果は少ない．

La mer (Bulletin de la Société franco-japonaise d'océanographie)
Tome 18, N° 3, pp. 104 à 115, Août 1980

The Wind Induced Seiche Motion and Wind Set-up in a Small Closed Channel*

Nobuo MORITANI** and Tomosaburo ABE***

Abstract: The wind induced seiche motion and the wind set-up were experimentally studied in a small closed channel. It is seen that the period of the co-oscillated seiche motion caused by the periodically changing wind speed is slightly elongated by the effects of the viscosity of water. Wind stress and drag coefficient are estimated by the co-oscillated seiche's amplitude and the wind set-up based on the one dimensional linear model, neglecting the atmospheric pressure gradients and assuming the wind stress is given by $\tau_0 \sin \sigma t \cdot \sin \pi x/L$ for the seiche motion and by $\tau_0 \sin \pi x/L$ for the wind set-up, where σ coincides with the frequency of the mono-nodal seiche motion, L is length of the closed channel and τ_0 means the constant shear stress. It is seen that the effects of the air pressure cannot be neglected for the wind speed smaller than about 2 m/sec. The value of the drag coefficient $\gamma^2{}_*$, estimated by the seiche's amplitude, is in the region of 0.004~0.012 for the mean wind speed greater than about 3 m/sec, and it becomes larger for increased wind speed owing to the effects of the form resistance of the waves as seen in the case of wind set-up. These estimated values of the drag coefficient are about two or three times larger than that measured by the wind set-up or the wind profiles in the wind channel.

1. Introduction

Seiche motions in lakes, bays or harbours are induced by the variously changing external forces, such as atmospheric pressures, wind stresses, seismic disturbances of land crusts and so on. HIDAKA (1935) studied on the seiche motion induced by the periodically changing wind shear stress $\tau_0 \sin \sigma_t \sin \pi x/L$ in the rectangular basin where τ_0 is constant shear stress, σ frequency of the stress and L length of the basin. However, it is hard to apply this theoretical study to the seiche motion in the practical fields, because of its complicated shapes and the irregularly changing external forces. The present authors observed the water level in the Ushigomebori, one of the defense moat of the ancient Edo Castle, which is a roughly rectangular basin with the dimension of approximately $612 \times 60 \times 1.0$ m. Previously, they made a brief quantitative discussion on the observed seiche motion generated by the wind stress in the moat (MORITANI and ABE 1973). The estimated drag coefficient $\gamma^2{}_{10}$ using the amplitude of seiche motion is given by 2.3×10^{-3} on the average, on the assumption that the seiches are generated by the co-oscillation with the wind stress $\tau_0 \sin \sigma_t \sin \pi x/L$ (σ is frequency of the mono-nodal seiche, L length of the moat) and that they are subject to the uniform internal friction which is assumed to be $-2\rho\varepsilon\bar{u}$ (ρ is density of water, ε frictional coefficient and $\bar{u}$ the average horizontal velocity of water).

The present paper studies on the experimental investigations relating to the co-oscillated seiche motion induced by the periodically changing wind speed and wind set-up by a constant wind speed in a small closed channel, which is 2.8 cm deep, 15 cm wide and 175 cm long.

2. Theoretical Prediction

Wind stress and drag coefficient are calculated by the following three kinds of methods.

(1) Method of measuring the wind prfiles

The vertical wind profile on the water surface has very complicated properties (MITSUYASU

* Received January 10, 1980
** Tokyo Center, Japan Weather Association, Chiyoda-ku, Tokyo, 101 Japan
*** Faculty of Science, Science University of Tokyo, Shinjuku-ku, Tokyo, 162 Japan

1964). In our case, we use the formula of ROSSBY (1936) as follows,

$$\frac{V}{u_*}=5.75\ln\frac{z+z_0}{z_0}, \qquad (1)$$

where u_*; friction velocity
z_0; roughness length
z; height from water surface.

Then, the shear stress τ_s working on the water surface is given by

$$\tau_s=\rho_a u_*^2, \qquad (2)$$

where ρ_a is density of air.
The surface stress may be correlated with the wind speed as follows.

$$\tau_s=\rho_a \gamma^2 V^2 \qquad (3)$$

In the equation (3), γ^2 means the drag coefficient. From the equations (2) and (3), drag coefficient γ^2 is given by friction velocity and wind speed as follows,

$$\gamma^2=u^2_*/V^2. \qquad (4)$$

(2) Method of measuring wind set-up

Wind set-up or wind tide is induced by the constant wind over the water surface in the closed basin. As shown in Fig. 1, we take the x-axis along the mean water surface in the direction of the wind, with the z-axis upwards. We consider the rectangular basin and, assuming that the water is homogeneous, neglect the Coriolis force and the horizontal pressure gradient.

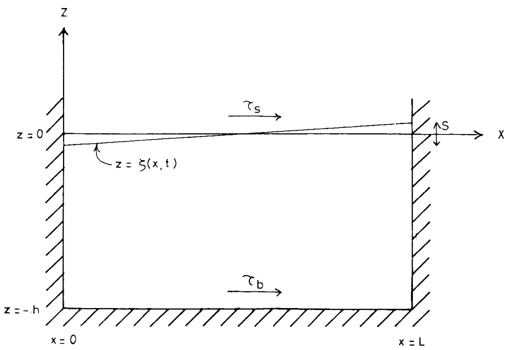

Fig. 1. A cross section of the rectangular basin. S, the wind set-up induced by the surface shear stress τ_s.

In this case, the equation of horizontal motion becomes

$$g\frac{\partial\zeta}{\partial x}=\frac{\tau_s+\tau_b}{\rho h}, \qquad (5)$$

where τ_s, τ_b are horizontal stress at surface and bottom respectively, and g the acceleration of gravity, h the water depth, ρ the water density and $\zeta(x, t)$ elevation. Integrating the equation (5) with respect to x from 0 to L, wind set-up S may be given by

$$\frac{S}{L}=\frac{n\bar{\tau}_s}{\rho g h}, \qquad (6)$$

where S is difference in elevation between two ends of the basin, n is defined as $n=1+\bar{\tau}_b/\bar{\tau}_s$ and

$$\bar{\tau}_b=\frac{1}{L}\int_0^L dx,\quad \bar{\tau}_s=\frac{1}{L}\int_0^L\frac{\tau_s}{\rho}dx. \qquad (7)$$

Next, we state wind stress as

$$\tau_s=\tau_0\sin\frac{\pi x}{L}. \qquad (8)$$

Then, the mean wind stress τ_s becomes

$$\bar{\tau}_s=\frac{\tau_0}{L}\int_0^L\sin\frac{\pi x}{L}dx=\frac{2}{\pi}\tau_0. \qquad (9)$$

Upon substituting the equation (9) into (6), the wind set-up is given by

$$S=\frac{2n\tau_0 L}{\pi\rho g h}. \qquad (10)$$

After the Keulegan's experiments (1951) in a laboratory channel, wind set-up is given by the following equations,

$$S=S_1+S_2 \qquad (11)$$

$$S_1=A\frac{V^2}{gh},\quad S_2=B\frac{(V-V_c)^2}{gh}\left(\frac{h}{L}\right)^{1/2} \qquad (12)$$

where V; wind speed,
V_c; formula velocity ($V_c=3.9$ m/s),
$A=3.30\times10^{-2}$, $B=2.08\times10^{-1}$.

In the equation (12), S_1 means set up induced by a tangential friction drag and S_2 by a form drag. The second effect is related to the surface waves. Now, we state surface stress as

$$\bar{\tau}_s=\rho_a\gamma^2\overline{V}^2, \tag{13}$$

where

$$\overline{V}^2=\frac{1}{L}\int_0^L V^2dx. \tag{14}$$

In this case, drag coefficient γ^2 becomes

$$\gamma^2=\frac{ghS}{n\rho_a V^2L}. \tag{15}$$

On the other hand, from the Keulegan's equations (11) and (12),

$$\gamma^2=\frac{\pi A\rho}{2nL}+\frac{\pi B\rho}{2nL}\left(1-\frac{V_c}{V}\right)^2\left(\frac{h}{L}\right)^{1/2} \tag{16}$$

If a computation is made of the basis of pure laminar motion, the value of n will become 1.5 (KEULEGAN 1951). On the other hand, from the observation in the model yacht pond, VAN DORN (1953) estimated as $n=1.0$. Temporarily, let us follow the latter.

(3) Method of measuring seiche's amplitude

With the same conditions stated as in the former section (2), the motion of the water mass in the rectangular basin is given by

$$\frac{\partial\bar{u}}{\partial t}+g\frac{\partial\zeta}{\partial x}=\frac{\tau_s+\tau_b}{\rho h}. \tag{17}$$

Now, we assume that bottom stress τ_b is proportional to the mean horizontal velocity $\bar{u}(x, t)$, giving

$$\frac{\tau_b}{\rho h}=-2\varepsilon\bar{u}(x,t), \tag{18}$$

where ε is frictional coefficient.

Let us assume that the surface stress can be given by

$$\tau_s=\tau_0\sin ft\cdot\sin\frac{\pi x}{L}, \tag{19}$$

where L is the length of the basin and f is the frequency of wind stress. The period of the mono-nodal seiche motion is given by the Merian's formula,

$$T=\frac{2L}{\sqrt{gh}}. \tag{20}$$

Then, its frequency becomes

$$\sigma=\frac{\pi\sqrt{gh}}{L}. \tag{21}$$

In this case, the equation of motion and the equation of continuity are given by

$$\begin{cases}\dfrac{\partial\bar{u}}{\partial t}+g\dfrac{\partial\zeta}{\partial x}+2\varepsilon\bar{u}=\dfrac{\tau_0}{\rho h}\sin ft\cdot\sin\dfrac{\pi x}{L} & (22)\\[2ex] h\dfrac{\partial\bar{u}}{\partial x}+\dfrac{\partial\zeta}{\partial t}=0. & (23)\end{cases}$$

The forced seiche motion is given by the equations (22) and (23) giving resonant condition when the frequency f tends to σ. In this case, the elevation $\zeta(x, t)$ becomes

$$\zeta(x,t)=\zeta_0(1-e^{-\varepsilon t})\sin(\sigma t+\varphi)\cos\frac{\pi x}{L}, \tag{24}$$

where

$$\varphi=\pm\frac{\pi}{2},\quad \zeta_0=\frac{\pi\tau_0}{2\rho\varepsilon\sigma L}.$$

In the steady state, elevation $\zeta(x, t)$ becomes

$$\zeta(x,t)=\zeta_0\sin(\sigma t+\varphi)\cos\frac{\pi x}{L}. \tag{25}$$

HIDAKA (1935) discussed on the seiche motion with the equation of motion

$$\frac{\partial u}{\partial t}=\frac{k}{\rho}\cdot\frac{\partial^2u}{\partial z^2}-g\frac{\partial\zeta}{\partial x}+\frac{\tau_0}{\rho h}\sin ft\cdot\sin\frac{\pi x}{L}, \tag{26}$$

where k is the coefficient of kinematical viscosity, and the boundary conditions are

$$\left(-k\frac{\partial u}{\partial z}\right)_{z=0}=\tau_s,\quad (u)_{z=h}=0,$$

$$(u)_{x=0,L}=0. \tag{27}$$

Considering the wind stress of the equation (19), the elevation in the steady state is

$$\zeta_s^*(x,t)=\zeta_0^*\times$$

$$\sin\left\{\sigma t-\left(2\pi-\tan^{-1}\frac{\sin hq+\sin q}{\sin hq-\sin q}\right)\right\}\cdot\cos\frac{\pi x}{L}, \tag{28}$$

where

$$\zeta_0{}^* = \frac{\sqrt{2}\,\pi\tau_0}{\rho\sigma^2 L} \cdot q \cdot \sqrt{\frac{\cosh q - \cos q}{\cosh q + \cos q}}, \tag{29}$$

$$q = \sqrt{\frac{\rho\sigma h^2}{2k}}. \tag{30}$$

Hence, wind stress τ is measured by the seiche's amplitude $\zeta_0\ (x,\ t)$ or $\zeta_0{}^*\ (x,\ t)$.

Now, we assume the wind stress τ_0 is given by the wind speed with the following equation,

$$\tau_0 = \rho_a \gamma_*{}^2 V_*{}^2 \tag{31}$$

where ρ_a denotes the air density, $\gamma_*{}^2$ the drag coefficient and $V_*{}^2$ the Fourier constituency of the frequency σ of the squared wind speed (V^2). So that, from the equation (31), drag coefficient $\gamma_*{}^2$ becomes

$$\gamma_*{}^2 = \frac{\tau_0}{\rho_a V_*{}^2}. \tag{32}$$

3. Experimental Procedure and Instrumentation

The apparatus are shown in Fig 2. The upstream blower in the entrance assemblage was driven by a speed motor. Rotation of the motor is controlled by a couple of the variable resistances V_1 and V_2. The former supplies mean voltage and the latter supplies fluctuating voltage on the motor, and hence we can obtain the mean wind speed and the fluctuating wind speed. The experimental channel is a closed conduit of uniform rectangular cross section 15 cm deep, 10 cm wide and 175 cm long.

The wind speed measurement: Wind speed in the experimental channel is measured by the hot-wire anemometer as shown in Fig. 3. Its sensor is made of the platinum wire-resistance of 10 μm diameter and 3 mm long, with a fast response to the turbulent wind.

Water level measurements: Seiche's amplitude and wind set-up are measured by the capacity-type wave gauge at the both ends of the experimental channel. It measures the variation of the capacity of the air-layer between sensor plate and the water surface. As the sensor has the dimension of 5 cm × 6 cm, capillary waves may be smoothed up by it (cf. Fig. 3). Moreover, it is not affected by the effects of meniscus, since the sensor does not touch on the water surface. Therefore, it can detect waves less than 1/100 cm high.

An example of the records of the wind speed and the water level is shown in Fig. 4. It is seen that the regular oscillatory motion is

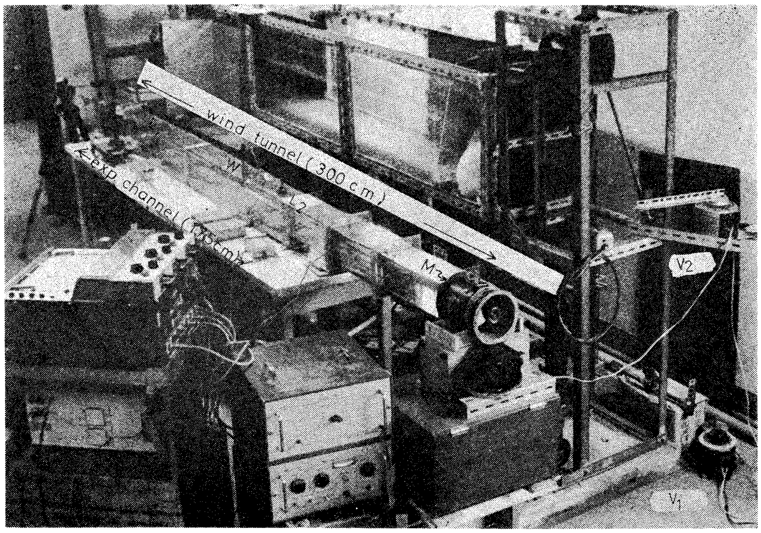

Fig. 2. Photograph of experimental apparatus. M, the blower; V_1 and V_2, the voltage regulators for the periodically changing or constant wind speed, respectively; L_1 and L_2, the sensors of the water level meter located at the both edges of the channel; and W, the sensor of the anemometer.

Sensor of the Anemometer

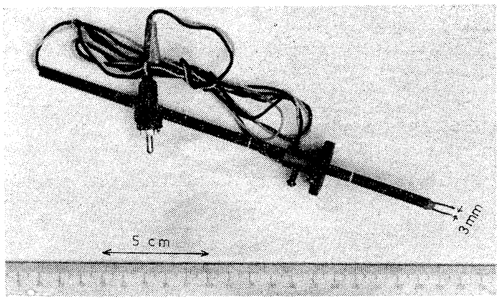

Sensor of the Water-Level Meter

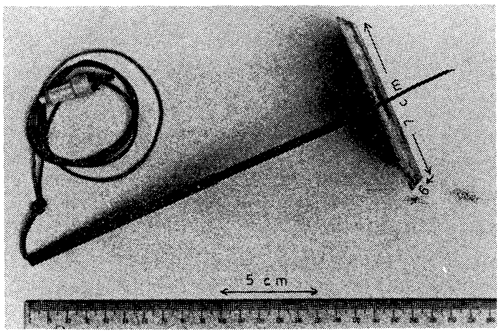

Fig. 3. Sensors of the water level meter and the hot-wire type anemometer.

induced by the changing wind speed and the mean water level is shifting according to the increase of the mean wind speed. The former oscillatory motion shows the mono-nodal seiche motion induced by the co-oscillation with the periodically changing wind speed and the latter shifting of the water level means the wind set-up induced by the averaged wind speed.

4. Observed Results and Discussions

In our experiments of the wind channel, the mono-nodal seiche motion was induced by the periodically changing wind around a constant wind speed, and the wind set-up was generated by a constant wind speed. Now, we discuss on the co-oscillated seiche motion and the wind set-up based on the one dimensional linear model.

(1) Vertical and horizontal wind profiles

Vertical wind profiles in the experimental wind channel are shown in Fig. 5. In the figure, segments of horizontal lines mean the breadth of the fluctuations of wind at the fetch length of 15, 50, 100 and 170 cm, respectively. At the

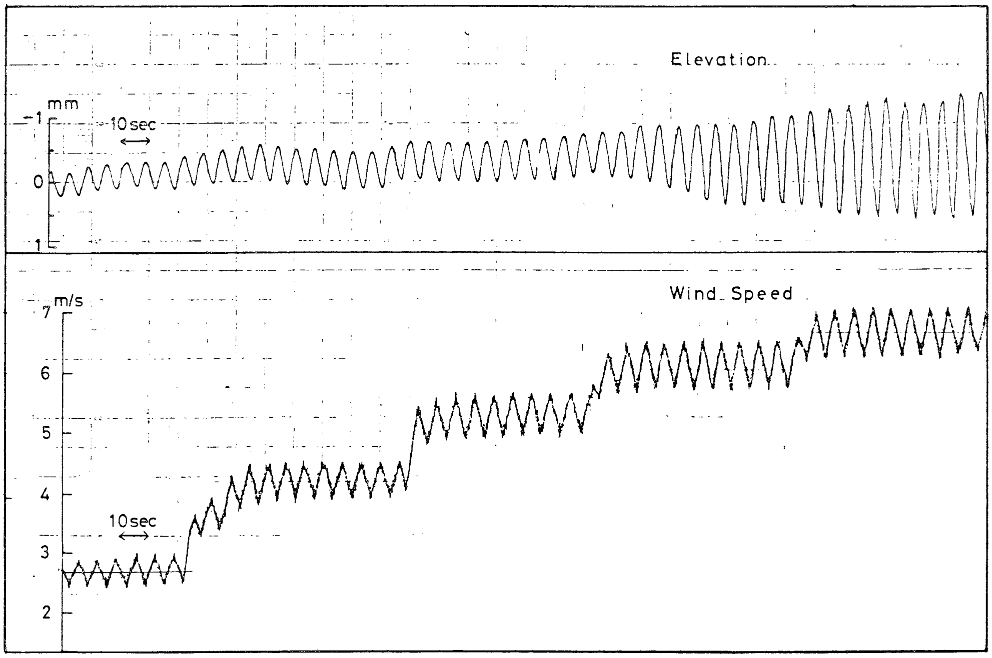

Fig. 4. Examples of the records of wind speed and water level. Upper; the deviation of water level observed at the station L_1 which is up-stream side of the channel. Lower; the wind speed observed by hot-wire type anemometer at the station W.

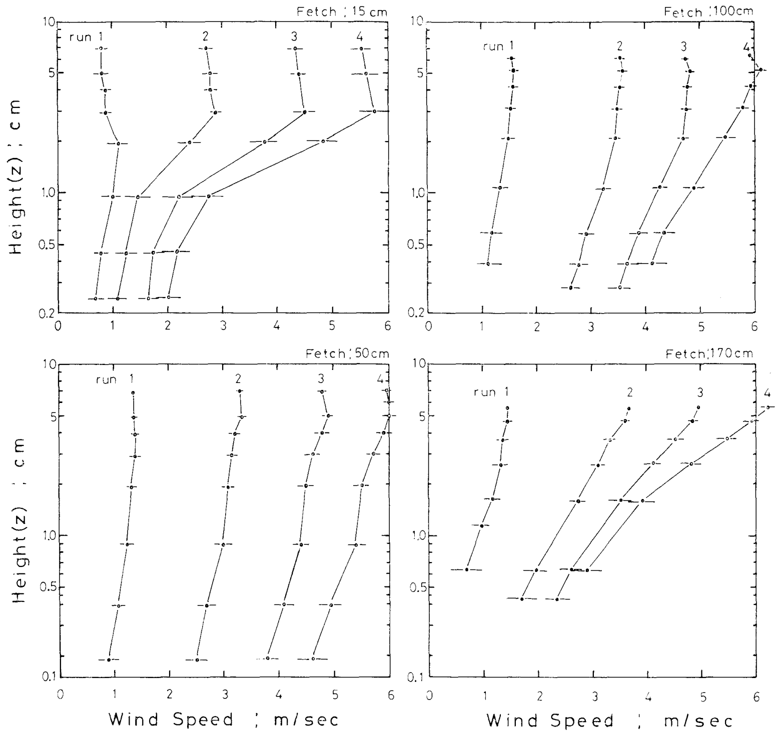

Fig. 5. Vertical wind profiles. Each solid circles show the averaged wind speed, and each horizontal segments the fluctuation of the wind speed around the averaged values.

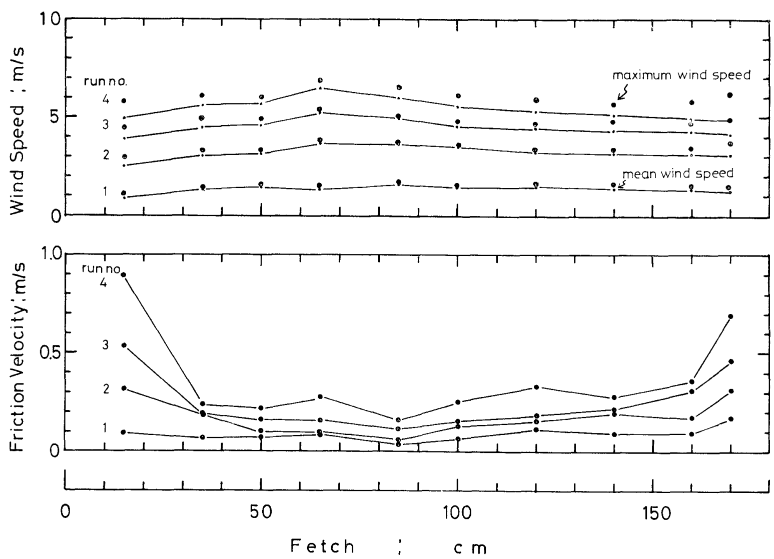

Fig. 6. Horizontal distributions of the wind speed and the friction velocity. Upper; the mean and the maximum wind speed in each cross section. Lower; the friction velocity u_*.

Table 1. The experimental constants in the channel.

Exp. Const.	ρ	ρ_a	ε	h	L	L'	$\cos \pi x/L$
Value	1.00 gr/cm^3	1.21×10^{-3}gr/cm^3	4.41×10^{-2}sec^{-1}	2.85 cm	175 cm	165 cm	0.996(x=5 cm)

fetch of 15 cm, fairly complicated wind profiles and relatively large fluctuations of wind speed are seen. Except for this case, it is seen that the gradient of the vertical wind profile becomes larger according to the increase of wind speed and the fetch length. In Fig. 6, the distribution of the wind speed and that of the friction velocity are shown. In the figure, mean and maximum wind speed are shown with the sign • and ●, respectively. Friction velocity u_* is calculated from the equation (1), using the data on the wind speed which is observed at the level lower than z=5 cm. The value of u_* is much larger in the both sides of area in the channel, and the mean wind speed is little larger in the middle part of the channel. However, it is estimated that the wind stress acting on the water surface is much smaller than the calculated value from the equation (2) at the both ends because of the effects of the both side walls of the channel.

It is considered that the wind stress acts on the whole water surface nearly at the same time for the wind speed greater than about 3 m/sec, since the length of the channel is 175 cm and the period of induced seiche motion is about 7 sec. Hence, we may assume that the effects of the pressure acting on the water surface can be neglected and the wind stress is given by the equation (8) for the wind set-up and by the equation (19) for the seiche motion, when the wind speed is greater than about 3 m/sec.

(2) Wind set-up

We observed the wind set-up induced by the constant or variable wind speed. Obtained results are discussed using the equation (10). In Table 1, our experimental constants are listed. In our case, L becomes 165 cm since elevation has been observed at the points x=5 cm and x=170 cm. And h=2.85 cm, ρ=1.00 gr/cm^3, g=980 cm/sec^2 and n states 1.00 as mentioned above. Substituting these constants into the equation (10), wind set-up becomes

$$S=0.0376\,\tau_0\,(\mathrm{cm})\,. \qquad (33)$$

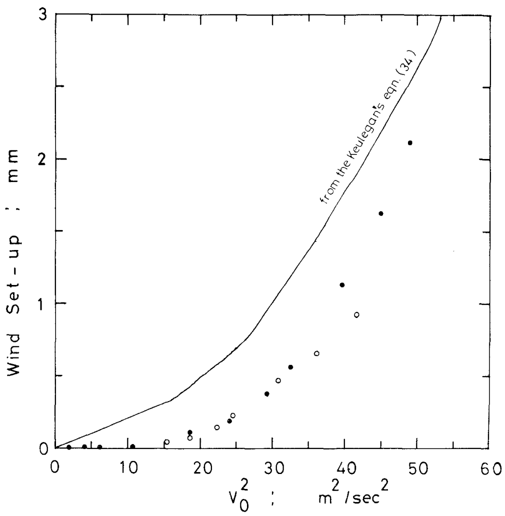

Fig. 7. Relation between the wind set-up and the wind speed V_0^2. Solid and open circles show the wind set-up S induced by the constant wind speed and the periodically changing wind speed around its mean value, respectively. The Keulegan's equation (34) is shown by the solid line.

If τ_0 is proportional to the horizontal average of the square of the wind speed V^2, S is also proportional to V^2. In Fig. 7, the observed values of the wind set-up S are plotted against V_0^2, where V_0 means the wind speed at the fetch 50 cm and the observed level z=6 cm. Solid line shows the Keulegan's equation of (11), with the values of L=165 cm and h=2.85 cm. It is given by

$$S=1.98\times10^{-3}\,V_0^2 + 1.62\times10^{-2}(V_0-3.9)^2\,(\mathrm{cm}). \qquad (34)$$

In the figure, the solid circles correspond to the data for the constant wind and the open circles for the changing wind around mean wind speed. For the region of the small value of V_0^2, it is nearly proportional to the set-up S. For the greater value of V_0^2, S is rapidly grown up. This fact owes to the effects of the form resistance of the waves.

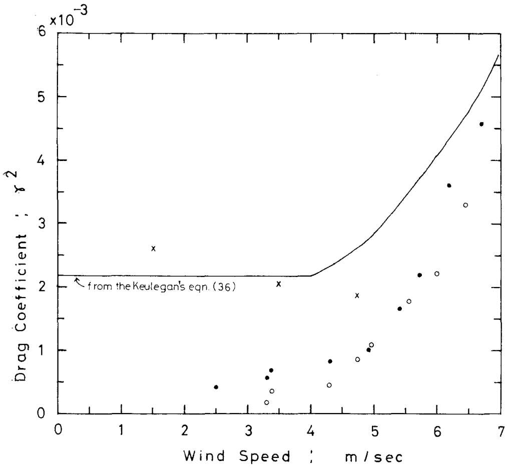

Fig. 8. Relations between the drag coefficient γ^2 and the wind speed V_0. Solid and open circles indicate the drag coefficient given by the wind set-up, and cross marks indicate those estimated by the wind profiles. Solid line shows the Keulegan's equation (36).

Substituting our experimental constants into the equation (15), the drag coefficient γ^2 is given by

$$\gamma^2 = 1.40\, S/V_0^2. \qquad (35)$$

On the other hand, Keulegan's equation (16) becomes

$$\gamma^2 = 2.18\times10^{-3} + 1.81\times10^{-2}(1-3.9/V_0)^2. \quad (36)$$

In Fig. 8, the calculated drag coefficient γ^2 from the equation (35) is plotted against wind speed V_0 with the solid circles and the Keulegan's equation (36) is also shown by the solid line. As shown in the figure, the obtained value of γ^2 is smaller than the Keulegan's value. This is mainly caused by the difference of the edge conditions of the both experimental channels, since the channel used by Keulegan is about ten times larger than ours. In the figure, the drag coefficient given by the wind profiles with the equation (1) is also shown with the sign $\times$.

(3) Wind induced seiche motion

By changing the wind speed periodically around a constant wind speed, the mono-nodal seiche motion is generated in the experimental channel, as shown in Fig. 4. We studied on the

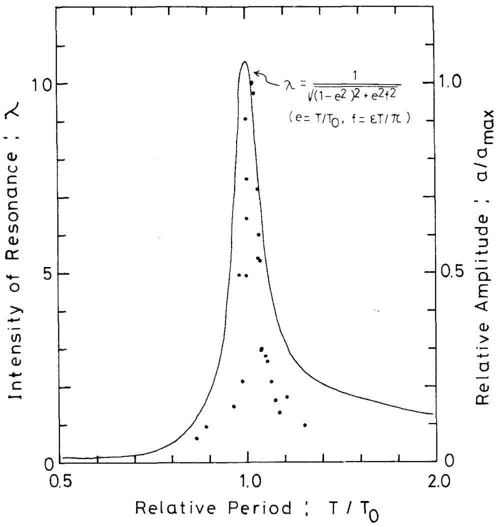

Fig. 9. Intensity of resonance. T_0 means the period given by the Merian's formula (20). Solid circles, the observed relative amplitude a/a_{max}; solid line, the theoretical curve of the intensity of resonance given by the linear model.

relations between the stress and the induced seiche motion.

(i) Intensity of resonance

The changing wind speed is given by the following formula

$$V(t) = V_0 + V_m \sin 2\pi t/T\,, \qquad (37)$$

where V_0 means constant wind speed, V_m amplitude of the changing wind speed and T period of it.

In our experiments, we estimate $V_0=4.5$ m/s, $V_m=0.45$ m/s and $T=5.0\sim9.5$ sec. With these conditions the obtained results are shown in Fig. 9. The period of the mono-nodal seiche motion in the rectangular basin may be estimated by the Merian's formula (20). In our case, the theoretical period of T_0 becomes 6.61 sec. As seen in Fig. 9, the strongest intensity of resonance occurs at the relative period of $T/T_0=1.03$. Its elongation of the period may be caused by the effects of the viscosity. The theoretical value of the elongation of the period becomes 5.2%, by taking into account the effects of viscosity after the paper of HIDAKA (1935).

(ii) Seiche's amplitude and wind stress

Assuming that the horizontal distribution of the wind stress is given by the equation (19) and neglecting the effects of the air pressure, the elevation of the resonated seiche motion is given by the equations (25) and (28). The effects of the pressure gradient will be discussed later. Using the experimental constants (see Table 1) in the equation (29), the following equation is obtained,

$$\zeta_0{}^* = 0.0281\,\tau_0 q\sqrt{\frac{\cosh q-\cos q}{\cosh q+\cos q}}\quad \text{(cm)}.$$

The damping coefficient of the seiche motion in the experimental closed channel is $\varepsilon=0.441\ \mathrm{sec}^{-1}$, so that the parameter q (denoted by the equation (30)) and the coefficient of kinematical viscosity k are given by

$$q=5.0 \quad \text{and} \quad k=0.15 \quad \text{c. g. s. - unit.}$$

In this case, from the above equation, the elevation $\zeta_0{}^*$ becomes

$$\zeta_0{}^*=0.141\,\tau_0 \quad \text{(cm)}. \qquad (38)$$

On the other hand, substituting the experimental constants into the equation (25), the elevation ζ at $x=5\,\mathrm{cm}$ becomes

$$\zeta(5,t)=0.996\,\zeta_0 \sin(0.147\,t+\varphi) \quad \text{(cm)}, \qquad (39)$$

where

$$\zeta_0=\pi\tau_0/2\rho\varepsilon\sigma L=0.220\tau_0 \quad \text{(cm)}.$$

Comparing the equation (39) with (38), it is seen that the estimated elevation ζ_0 is larger than $\zeta_0{}^*$ by about 1.5 times. The amplitude A becomes

$$A=0.996\,\zeta_0=0.219\,\tau_0 \quad \text{(cm) or}$$
$$\tau_0=4.56\,A \quad (\mathrm{gr\cdot cm^{-2}\,sec^{-2}}). \qquad (40)$$

In the equation (31), $V_*{}^2$ is given by Fourier transformation of V^2 of the equation (37), with multiplying $\cos 2\pi t/6.8$ on both sides and integrating 0 to 6.8 sec. Obtained results are as follows,

$$V_*{}^2=8(2\,V_0V_m+8\,V_m{}^2/3\pi)/3\pi. \qquad (41)$$

Observed amplitude A is plotted against the value of $V_*{}^2$. From the equations (31) and (40), amplitude becomes

$$A=0.219\,\rho_a\gamma_*{}^2V_*{}^2 \quad \text{(cm)}. \qquad (42)$$

Therefore, A is proportional to $V_*{}^2$ so long as $\gamma_*{}^2$ keeps a constant value. As shown in Fig. 10, A is approximately proportional to $V_*{}^2$. In Table 2, the conditions of the wind speed in each run number are shown. For the greater value of $V_*{}^2$ ($V_*{}^2>3\,\mathrm{m^2/sec^2}$), growth rates of the seiche's amplitude become larger. This is due to the effects of the formation of the surface waves for the greater wind speed, as seen in the case of wind set-up. We must note that relatively large amplitude occurs for the value of $V_*{}^2$ smaller than about $1.0\,\mathrm{m^2/sec^2}$.

From the equation (29), drag coefficient $\gamma_*{}^2$ can be decided from the seiche's amplitude A and $V_*{}^2$ as follows,

$$\gamma^2=3.77\times10^{-1}\,A/V_*{}^2. \qquad (43)$$

The value of $\gamma_*{}^2$ is plotted against the mean wind speed V_0 in Fig. 11. The value falls in the region of $0.004\sim0.012$ for the mean wind speed greater than about 3 m/sec, and it gradually grows up according as the wind speed increases by the effects of the form drag as seen in the wind set-up. On the other hand, for the smaller wind speed less than about 2 m/sec,

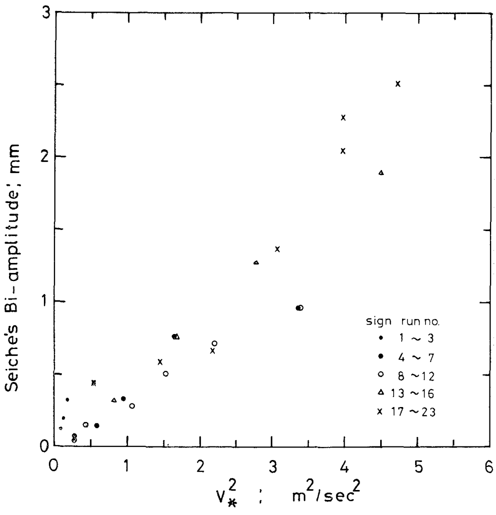

Fig. 10. Relation between the amplitude of seiche and $V_*{}^2$. The condition of wind speed in each run number is shown in Table 2.

Table 2. The conditions of the wind speed.

Run no.	1	2	3	4	5	6	7	8	9	10	11	12
V_0(m/s)	0.71	0.71	0.68	2.90	2.90	2.90	2.90	4.30	4.30	4.30	4.30	4.30
V_m(m/s)	0.25	0.19	0.13	0.10	0.20	0.32	0.55	0.75	0.50	0.35	0.25	0.10
Run no.	13	14	15	16	17	18	19	20	21	22	23	
V_0(m/s)	5.45	5.45	5.45	5.45	1.65	3.15	4.25	5.02	5.52	6.00	6.60	
V_m(m/s)	0.15	0.30	0.50	0.80	0.30	0.45	0.50	0.60	0.70	0.65	0.70	

$V(t)=V_0+V_m \sin 2\pi t/6.8$ (m/s)

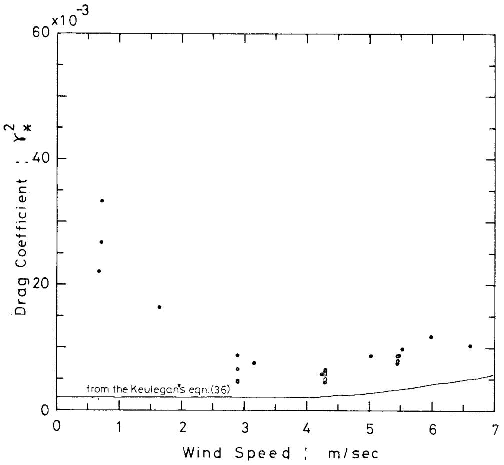

Fig. 11. Relation between the drag coefficient γ_*^2 and the wind speed. Solid circles, the estimated drag coefficient by seiche's amplitude; solid line, the Keulegan's equation (36).

γ_*^2 rapidly grows up according as the wind speed decreases. Its maximum value reaches about ten times larger than that given by the Keulegan's equation (36). The reason for this may be caused by neglecting the effects of the pressure gradient in the derivation of the equation (22).

(iii) The effects of the air pressure gradients

Now, we take into consideration the effects of the air pressure gradient. Instead of the equation (22), the equation of motion becomes

$$\frac{\partial \bar{u}}{\partial t}+g\frac{\partial \zeta}{\partial x}+2\varepsilon\bar{u}=\frac{\tau_s}{\rho h}+\frac{\partial p}{\partial x}. \qquad (44)$$

In the equation, $\partial p/\partial x$ means the air pressure gradients in the experimental channel. As the experimental channel has a constant cross section Bernoulli's theorem states

$$p(x,\ t)+\rho_a W^2(x,\ t)/2=C(t),$$

where $W(x,\ t)$ means wind speed and $C(t)$ is a function of time (t).

Upon differentiating on the both sides of the above equation with respect to x, we obtain

$$\frac{\partial p(x_1 t)}{\partial x}+\frac{\rho_a}{2\rho}\frac{\partial W^2(x,t)}{\partial x}=0.$$

Now, we devide $W^2/2$ into following two parts by using Fourier analysis,

$$W^2(x,t)/2=W_0^2/2 + W_*^2 \sin \sigma t \cos \pi x/L, \qquad (45)$$

where W_0 means a constant part and W_* is Fourier constituency of the frequency σ and the wave number π/L. In this case, the pressure gradients becomes

$$\frac{\partial p(x,t)}{\partial x}=\frac{\pi\rho_a W_*^2}{2\rho L}\sin \sigma t\cdot\sin\frac{\pi x}{L}. \qquad (46)$$

From the equations (19) and (31), surface stress τ_s is given by

$$\tau_s=\rho_a\gamma^2{}_* V^2{}_* \sin \sigma t \cdot \sin\frac{\pi x}{L}. \qquad (47)$$

Substituting the equations (46) and (47) into (44), we have

$$\frac{\partial \bar{u}}{\partial t}+g\frac{\partial \zeta}{\partial x}+2\varepsilon\bar{u} =\left(\frac{\rho_a\gamma_*^2 V_*^2}{\rho h}+\frac{\pi\rho_a W_*^2}{2\rho L}\right)\sin \sigma t \cdot \sin\frac{\pi x}{L}.$$

Then, the co-oscillated seiche induced by the surface stress and variational pressure gradient is given by

$$\zeta_0'=(\zeta_0-\zeta_p)\times(1-e^{-\varepsilon t})\sin(\sigma t-\varphi)\cdot\cos\frac{\pi x}{L}, \qquad (48)$$

where

$$\zeta_0=\frac{\rho_a\sigma\gamma_*^2V_*^2L}{2\pi\rho\varepsilon gh} \text{ and } \zeta_p=\frac{\rho_a\sigma W_*^2}{4\rho\varepsilon g}.$$

In the equation (48), ζ_0 means the elevation induced by the surface wind stress τ_s and ζ_p that induced by the pressure gradient $\partial p/\partial x$. Now, the ratio of ζ_p to ζ_o is given by,

$$R_\zeta=\frac{\zeta_p}{\zeta_0}=\frac{\pi hW_*^2}{2L\gamma_*^2V_*^2}. \qquad (49)$$

In our experimental channel taking $L=175$cm, $h=2.85$ cm and the drag coefficient $\gamma_*^2=0.00218$ by (36), the ratio R_ζ becomes

$$R_\zeta=11.7\frac{W_*^2}{V_*^2}. \qquad (50)$$

Therefore, it can be seen that ζ_p is about ten times larger than ζ_0 in our channel when W_* nearly equals to V_*. Generally, W_* may be much smaller than V_* in our experiments, so that we can assume that seiche motion is mainly induced by the surface wind stress and the effects of the pressure gradients may be neglected. However, it is necessary to consider the effects of the pressure gradients for the small wind speed.

As mentioned above, the period of the co-oscillated seiche motion is about 7 sec and the length of the channel is 175 cm. For the smaller wind speed less than about 1 m/sec, W_* may be estimated as $W_*\approx V_*$. In this case, seiche motion is mainly induced by the effects of the pressure gradient. Hence, the estimated value of the drag coefficient using the amplitude of the seiche motion is effective only for the wind speed greater than about 3 m/sec.

5. Concluding Remarks

The amplitude of the co-oscillated seiche motion, which is induced by the periodically changing wind speed, becomes greater according to the increment of wind stress τ_s, and its growth rate grows up with the increasing wind speed. The value of the drag coefficient γ_*^2, estimated by the seiche's amplitude, falls in the region of 0.004~0.012 for the mean wind speed greater than about 3 m/sec. These estimated values of the drag coefficient are about two or three times larger than that measured by the wind set-up or the wind profiles in the channel. It is seen that the effects of the air pressure gradient cannot be neglected for the wind speed smaller than about 2 m/sec in our channel. We shall leave the discussion of the effects of the pressure gradient in future.

Acknowledgement

The authors wish to express sincere thanks to the member of the Basic Research on Wind Waves (Haro Kenkyu-Kai in Japanese) for their valuable advice. Thanks are due to Mr. A. Yanai of Mejiro Gakuen Women's Junior College, Mr. A. Arai, Mr. H. Takayama and other members of Abe Laboratory in Science University of Tokyo for many significant suggestions and to the all graduated students in the laboratory for their help in the observations.

References

DEFANT, A. (1961): Physical Oceanography (II). Pergamon Press, London, p. 154-160.

HIDAKA, K. (1935): Forced standing oscillation of lake induced by periodic wind force (I), (II). Umi To Sora, **15**, 79-83; **15**, 113-119. (in Japanese)

KEULEGAN, G.H. (1951): Wind tides in small closed channels. Jour. Res. nat. Bur. Stand., **46**, 358-381.

MITSUYASU, H. (1964): On the shear stress and surface roughness of wind acting on the water surface. Coast. Engineer. Jap., **11**, 42-48. (in Japanese)

MORITANI, N. and T. ABE (1972): A geophysical consideration of water in the Ushigomebori Moat (On the seiche of the moat). Prep. 2nd Intern. Ocean Devel. Conf., **1**, 270-281.

MORITANI, N. and T. ABE (1973): A geophysical consideration of the water in the Ushigomebori Moat (On the seiche motion of the moat (II)). La mer, **11**, 196-204.

MORITANI, N. and T. ABE (1978): A geophysical consideration of the water in the Ushigomebori Moat (On the transversal seiche motion induced by the Nemuro-Hanto-Oki Earthquake on June 17, 1973). La mer, **16**, 188-197.

VAN DORN, W. G. (1953): Wind stress on an artificial pond. Jour. Mar. Res., **12**, 249-276.

小型風洞水槽における風によって誘発された静振と set-up

森 谷 誠 生， 阿 部 友 三 郎

要旨: 風によって誘発された静振と set-up について，小型水槽による実験を行った。一定風速のまわりを周期的に変動する風によって，共振的に誘発された静振の周期は，水の粘性の影響によってわずかに伸長されていることが認められた。

風の応力と drag coefficient を，共振静振の振幅および wind set-up から一次元線型モデルによって推定した。このモデルは，大気圧の圧力勾配を無視し，風の応力としては (i) 静振運動の場合には $\tau_0 \sin \sigma t \cdot \sin \pi x/L$ (ii) set-up の場合には $\tau_0 \sin \pi x/L$，と各々仮定している。ここに，σ は単節振動の振動数，L は水槽の長さ，τ_0 は風の応力（一定）である。大気圧の影響は，この水槽風洞による実験においては，風速が約 2 m/sec 以下の場合これを無視することができない。

静振の振幅から推定された drag coefficient の値 (γ_*^2) は，風速が 3 m/sec 以上のとき 0.004～0.012 の範囲にあって，その値は風速が増大するに従って大きくなっており，これは wind set-up の場合にも認められたように，表面波の形状抵抗の効果であると考えられる。これら γ_*^2 の推定値は，wind set-up ないしは風速の鉛直分布から算定された drag coefficient の値より約 2～3 倍大きめの値を示している。

La mer (Bulletin de la Société franco-japonaise d'océanographie)
Tome 18, N° 3, pp. 116 à 124, Août 1980

Measurements of Photosynthesis and Productivity of the Cultivated *Monostroma* Population*

Miyuki MAEGAWA**

Abstract: Photosynthesis and productivity of the cultivated *Monostroma latissimum* population were studied by using a newly devised assimilation chamber which continuously monitors the oxygen concentration in water. Daily gross production (P_g), net production (P_n), respiration, P_g/P_n ratio and the energy efficiency of P_g and P_n were compared under different solar radiation on fine, cloudy-fine, cloudy and rainy days.

1. Introduction

Photosynthesis of seaweeds, major primary producers in shallow coastal areas, is the important basis of the primary production in the coastal ecosystem. Thus, a considerable amount of knowledge on photosynthesis and respiration of seaweeds has been accumulated from an ecological point of view (DOTY 1971, YOKOHAMA 1973, MAEGAWA and ARUGA 1974, KING and SCHRAMM 1976, BUESA 1977). The estimation of primary production of seaweeds has generally been based on measurments of photosynthetic and respiratory rates. Population photosynthetic activity is especially important for estimating and/or analyzing production of a seaweed population. However, in many studies photosynthetic activity of seaweeds was measured by using a single frond or only parts of a frond, so that causal appreciation of the primary productivity in coastal areas in relation to their environmental factors seems impossible without appropriate information on the photosynthetic characteristics of seaweed population. In natural conditions the solar radiation seems to be one of the most important factors in determining population photosynthesis. There are, however, relatively few studies of the population photosynthesis of aquatic plants in relation to the intensity of solar radiation from an ecological point of view (ODUM 1956, EDWARDS and OWENS 1962, IKUSIMA 1966, 1967).

In the present paper the diurnal changes in population photosynthesis and productivity of cultivated *Monostroma* population, especially the relationship between various weather types and photosynthetic activity, will be described.

2. Material and Methods

The material used in this study was the green alga *Monostroma latissimum* (KÜTZING) WITTROCK, which is mostly cultivated in Japan with a method similar to that in the cultivation of the red algae *Porphyra*.

Cultivation nets for the present study were seeded artificially on September 11, 1978, and reared in the cultivation ground (34°16′N, 136°48′E) in Ago Bay, Mie Pref., where the seawater is affected somewhat by the inflow of river water but has recently been eutrophicated by sewage.

The net for *Monostroma* cultivation was made of synthetic fibers (cremona), and was about 18 m long and 1.2 m wide. At the middle of the cultivation season on January 10, 1979, the cultivation net was cut into a size of about 77 cm by 60 cm, and was spread in frames for measuring population photosynthesis and standing stock.

For measuring population photosynthesis, an assimilation chamber was constructed (Figs. 1 and 2). This chamber measured $100 \times 75 \times 25$ cm and contained about $150\,l$ seawater. The water surface of the assimilation chamber was open to the air. Fresh seawater pumped up

* Received March 2, 1980
** Fisheries Research Laboratory, Mie University, Shima, Mie Pref., 517-07 Japan

was poured into the assimilation chamber at a constant rate of 5 l/min. Seawater in the assimilation chamber was stirred by using two underwater pumps at a rate of 40 l/min, and was mixed quickly with fresh seawater pumped up in order to make the dissolved oxygen concentration as uniform as possible. Thus, most of the seawater in the assimilation chamber was circulated by the two underwater pumps and the rest of the seawater, equivalent to the volume of seawater pumped up, was allowed to flow out. Water temperature in the assimilation chamber was about 1°C higher than that pumped up from cultivation ground because of the heat from the two underwater pumps. When the frame with *Monostroma* was immersed in seawater in the assimilation chamber, it was observed that *Monostroma* population was shaken constantly by flowing seawater during a measuring period. After seawater was circulated for two hours, measurement was started. The measurement was continued for 25 hr from 06:00 a.m. to 07:00 a.m. next day.

Dissolved oxygen concentration of inflowing and outflowing seawater was measured continuously by two O_2 electrodes (Marteck Model DOA) connected to a recorder (TŌA EPR 200A). Calibration for dissolved oxygen was carried out each hour by the Winkler titration technique during a period of photosynthesis measurement. Water temperature was measured by a thermister thermometer (Marteck Model TMS). Photosynthetic oxygen production and respi-

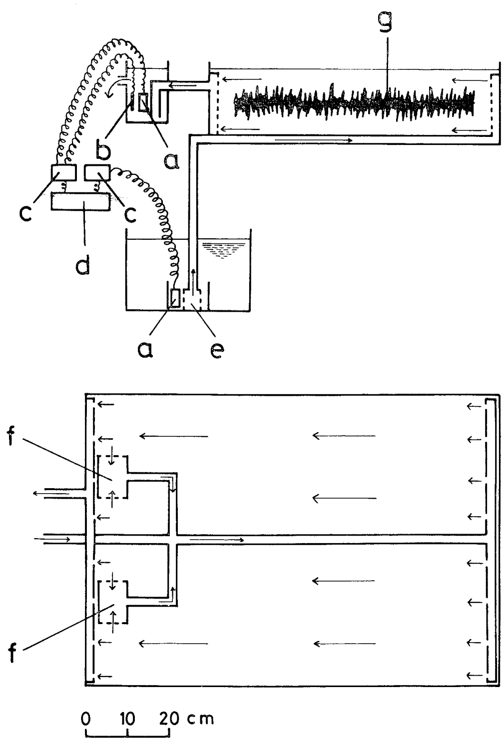

Fig. 1. Diagrams showing principal components of the apparatus (above) and assimilation chamber (below) for measuring population photosynthesis of *Monostroma*. a, O_2 electrode; b, thermister thermometer; c, analyzer unit; d, recorder; e, water pump for drawing; f, water pump for stirring; g, *Monostroma* population.

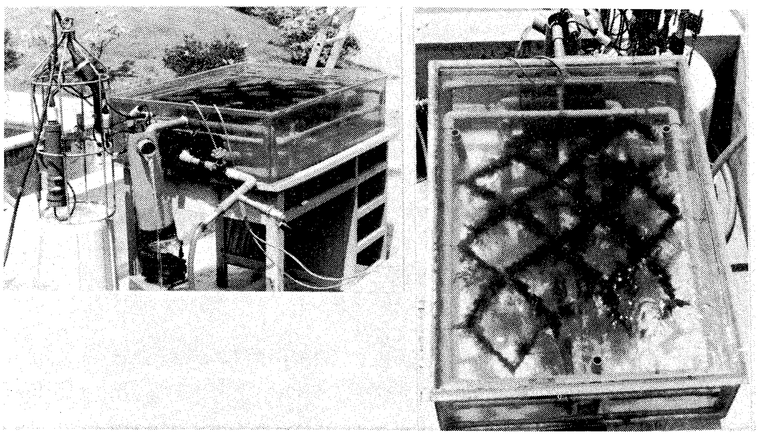

Fig. 2. Photographs of the assimilation chamber with *Monostroma* population.

ratory oxygen consumption were calculated from the record of dissolved oxygen changes. Measurements were carried out on fine (February 1–2), cloudy-fine (February 2–3), cloudy (February 18–19) and rainy (February 9–10) days.

For the measurement of standing stock, *Monostroma* fronds attached to the cultivation net were rinsed quickly with freshwater and dried overnight at 80°C, then picked out from the net and weighed.

Solar radiation was measured with a Robitch type actinometer (Tokyo Keiki Co.) set up close to the assimilation chamber, which responded to the irradiance of whole spectrum.

3. Results

Figs. 3-6 show the obtained diurnal changes in dissolved oxygen concentration of inflow and outflow seawater on four typical weather days; fine, cloudy-fine, cloudy and rainy. The oxygen concentration of outflow seawater was lower than that of inflow seawater at night because of respiration, while it was higher during the daytime because of photosynthesis.

When dissolved oxygen concentration in water is in excess of 100% saturation due to photosynthetic O_2 production of the *Monostroma* population, dissolved oxygen diffuses from water to the air through the water surface. For

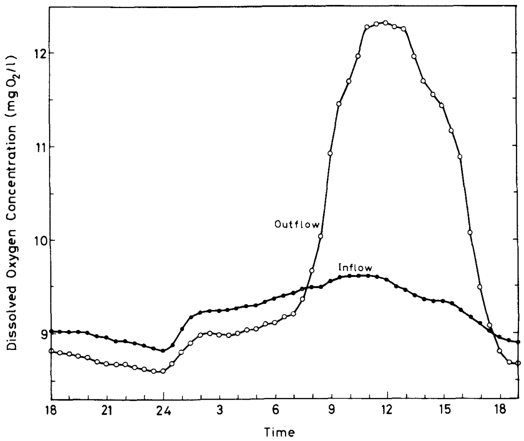

Fig. 3. Diurnal changes of dissolved oxygen concentrations in inflow and outflow seawater of the assimilation chamber on fine day (Feb. 1–2, 1979).

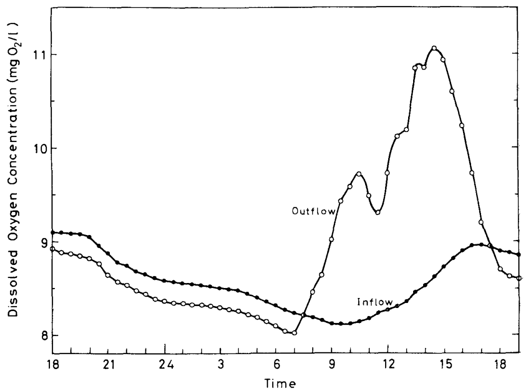

Fig. 4. Diurnal changes of dissolved oxygen concentrations in inflow and outflow seawater of the assimilation chamber on cloudy-fine day (Feb. 2–3, 1979).

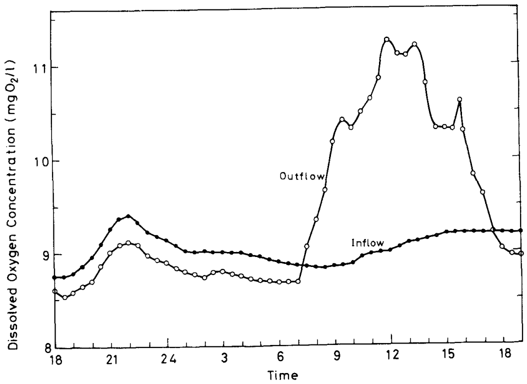

Fig. 5. Diurnal changes of dissolved oxygen concentrations in inflow and outflow seawater of the assimilation chamber on cloudy day (Feb. 18–19, 1979).

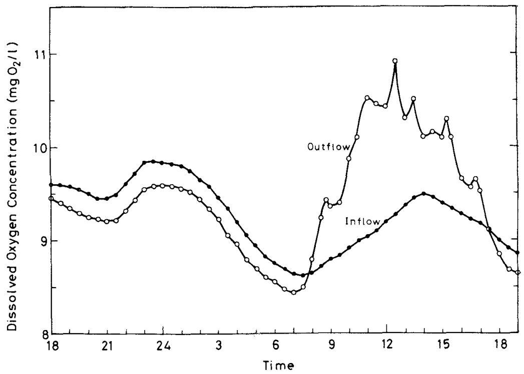

Fig. 6. Diurnal changes of dissolved oxygen concentrations in inflow and outflow seawater of the assimilation chamber on rainy day (Feb. 9–10, 1979).

estimating the diffusion rate, a transparent acrylic board was tightly set on the water surface and O_2 production by *Monostroma* population was measured. Under the same conditions of light and water temperature, but without a transparent acrylic board, O_2 production was also measured. The results are shown in Fig. 7a and b respectively. From these data the diffusion rate of dissolved oxygen was calculated as shown in Fig. 7c. Approximately 0.6% of dissolved oxygen was diffused at 110% saturation level, and approximately 3% at 135% saturation level.

The photosynthetic and respiratory rates

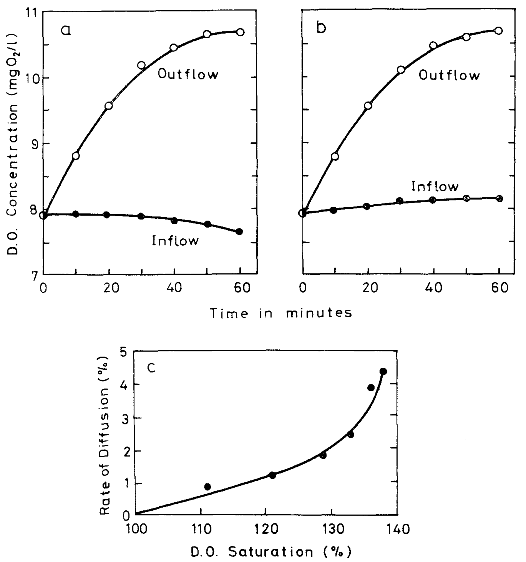

Fig. 7. Changes of dissolved oxygen concentrations in inflow and outflow seawater of the assimilation chamber with a transparent acrylic board on the water surface (a) and without it (b), and the calculated diffusion rates (c).

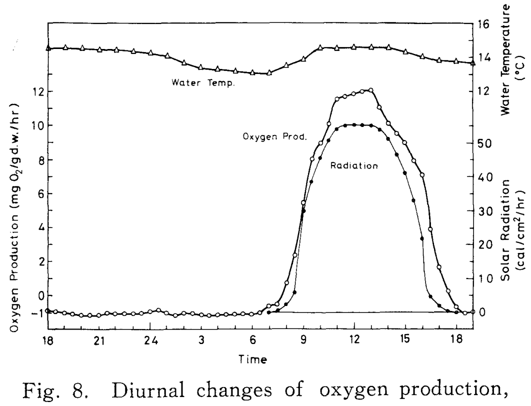

Fig. 8. Diurnal changes of oxygen production, solar radiation and water temperature on fine day (Feb. 1-2, 1979).

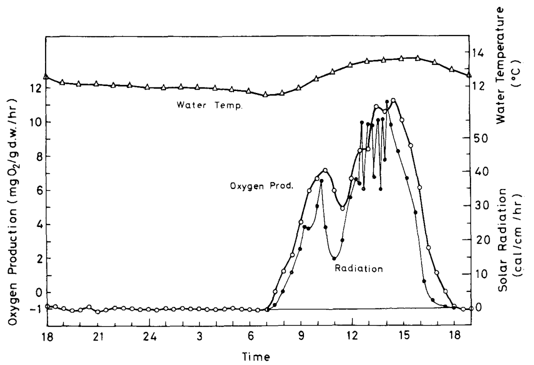

Fig. 9. Diurnal changes of oxygen production, solar radiation and water temperature on cloudy-fine day (Feb. 2-3, 1979).

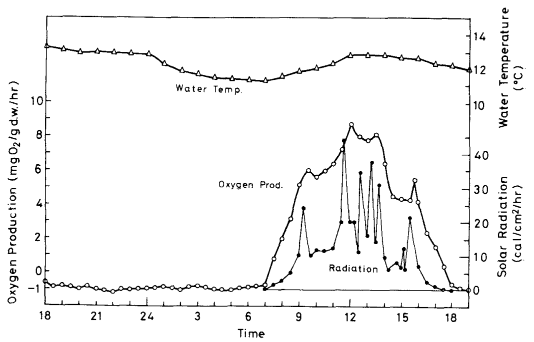

Fig. 10. Diurnal changes of oxygen production, solar radiation and water temperature on cloudy day (Feb. 18-19, 1979).

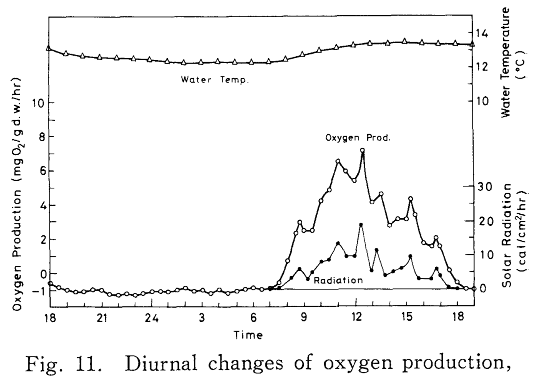

Fig. 11. Diurnal changes of oxygen production, solar radiation and water temperature on rainy day (Feb. 9-10, 1979).

(mgO_2/g(d. w.)/hr) were calculated from the difference in oxygen concentration between inflow and outflow seawater (Figs. 3-6), the diffusion rate from water surface (Fig. 7c) and the volume of inflow seawater. The obtained diurnal changes are illustrated in Figs. 8-11 together with the diurnal changes in solar radiation (cal/cm^2/hr) and water temperature (°C). Respiratory rate in the night was kept almost constant at a level of ca. 1.0 mgO_2/g (d. w.)/hr. After sunrise the photosynthetic oxygen production increased with increase in solar radiation. However, the record of the oxygen concentration seems to be delayed 15-20 min as compared with the actual change in solar radiation possibly due to a partial exchange of seawater in the assimilation chamber. On fine day a maximum net photosynthetic activity of 12.1 mgO_2/g(d. w.)/hr was reached at 55 cal/cm^2/hr at noon (Fig. 8). Water temperature was high at noon and low early in the morning, but the difference was not so large, normally less than 2°C.

Fig. 12 shows a relationship between the solar radiation and the photosynthetic rate, and the efficiency of gross production for four types of weather. The data on fine and cloudy-fine days and those on cloudy and rainy days were plotted respectively in the same figures. However, six points corresponding to the six peaks of solar

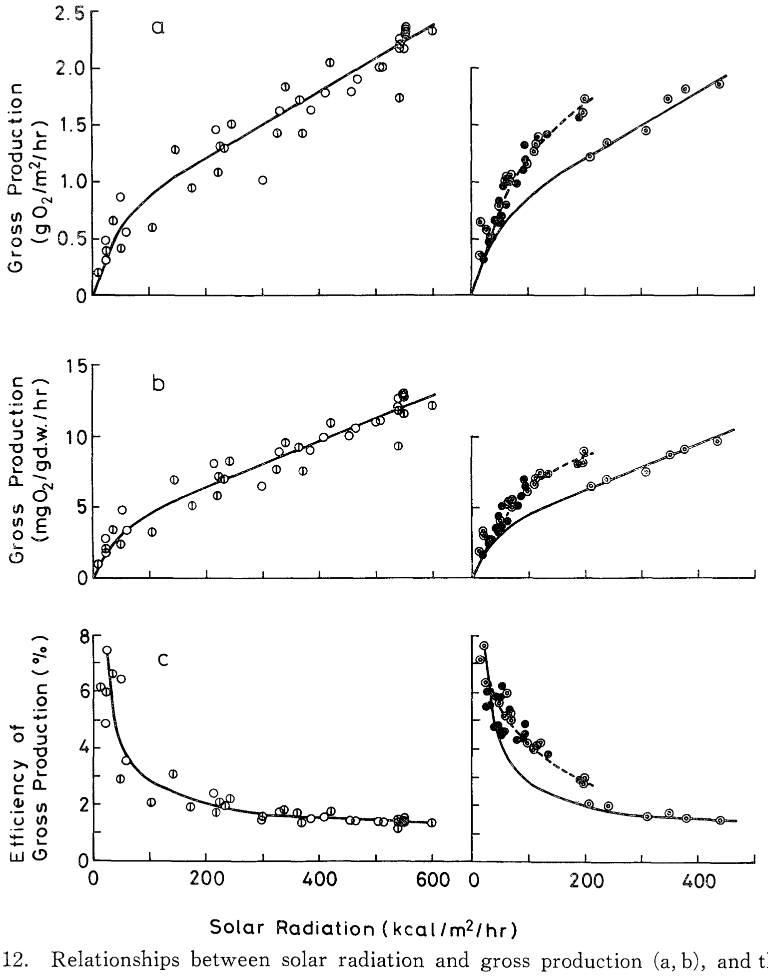

Fig. 12. Relationships between solar radiation and gross production (a, b), and the efficiency of gross production (c) on fine (○) and cloudy-fine (⦶) days (solid line), and on cloudy (◎) and rainy (●) days (broken line).

Table 1. Comparisons of the daily gross production (P_g), net production (P_n), respiration (R), P_n/P_g ratio and energy efficiency of the *Monostroma* population under different solar radiation.

	Standing Stock g(d.w.)/m²	Solar Radiation kcal/m²/day	P_g gO₂*	P_g g**	P_n gO₂*	P_n g**	R gO₂*	R g**	P_n/P_g	Efficiency % P_g	Efficiency % P_n
Fine	180	3490	16.0	13.4	11.7	9.8	4.3	3.6	0.73	1.6	1.2
Cloudy-fine	185	2630	13.4	11.3	9.0	7.6	4.4	3.7	0.67	1.8	1.2
Cloudy	192	1230	12.0	10.1	7.4	6.2	4.6	3.9	0.61	3.4	2.1
Rainy	190	660	8.5	7.1	3.9	3.3	4.6	3.9	0.46	4.5	2.1

$gO_2^* = gO_2/m^2$ $g^{**} = g(d.w.)/m^2$

radiation higher than 200 kcal/m²/hr on cloudy day (Fig. 10) can be included in the figures for fine and cloudy-fine days because the direct solar radiation at those points was as high as on fine or cloudy-fine day. When the solar radiation was lower than 200 kcal/m²/hr, the photosynthetic rates were apparently higher on cloudy and rainy days than on fine and cloudy-fine days (Fig. 12). The energy efficiency of gross production was calculated as the percent of the solar radiation received, assuming that the photosynthetic O_2 production of 1 g is equivalent to 3.5 kcal (RYTHER 1959). As can be seen in Fig. 12c, the efficiency was appreciably high at lower solar radiation and it decreased sharply and then gradually to a constant level of 1.5% as the solar radiation increased up to 300–600 kcal/m²/hr.

Table 1 shows the summary of the present productivity study. Standing stock of the *Monostroma* population used was almost at the same level, 180–192 g(d. w.)/m². Daily solar radiation ranged from 660 kcal/m² on rainy day to 3490 kcal/m² on fine day. Gross and net production and respiration expressed in gO_2 were converted to those in dry weight as 1 gO_2 is equivalent to 0.84 g dry matter. The daily gross production and net production were low, 7.1 and 3.3 g(d. w.)/m² respectively, on rainy day. They reached 13.4 and 9.8 g(d. w.)/m² respectively on fine day. Daily respiration was almost the same, 3.6–3.9 g(d. w.)/m², irrespective of weather conditions. The ratio of net to gross production (P_n/P_g) was low, 0.46, on rainy day, and it increased to 0.73 on fine day. The energy efficiency of gross production was low, 1.6%, on fine day and high, 4.5%, on rainy day. The efficiency of net production was 1.2% on fine and cloudy-fine days and 2.1% on cloudy and rainy days.

4. Discussion

Estimations of the primary productivity of aquatic algal populations have generally been based on measurements of the changes in dissolved oxygen concentration in ambient water, which were caused by the algal photosynthesis and respiration under the stationary condition (IKUSIMA 1965, SATOMI *et al.* 1967). IKUSIMA (1967, 1970) developed the mathematical formulation to calculate the amount of daily photosynthesis in submerged plants at various depths under different weather conditions on the basis of photosynthesis-light curve. ODUM (1956) and EDWARDS and OWENS (1962) employed the twin oxygen curve technique, which was based on the diurnal changes in the dissolved oxygen concentration in water between an upstream station and a downstream station. In the present study the method employed for continuously measuring the population photosynthesis of *Monostroma* was similar in principle to the twin oxygen curve technique.

YOKOHAMA (1973) and MAEGAWA and ARUGA (1974) obtained the light-saturated rate of photosynthesis, 28–30 mgO_2/g(d. w.)/hr, by using single fronds of *Monostroma*. In the present study no light-saturation was observed in the photosynthesis-light curves of a *Monostroma* population up to the highest solar radiation of 55 cal/cm²/hr or 600 kcal/m²/hr (cf. Fig. 12), and the highest gross photosynthesis obtained was 12.1 mgO_2/g(d. w.)/hr or 2.3 gO_2/m²(net area)/hr, which was about a half the corresponding rate for single fronds. photosynthetic rate of *Porphyra* population measured by

SATOMI *et al.* (1967) and that of *Vallisneria* population measured by IKUSIMA (1966) were $3.0\ gO_2/m^2/hr$ and 12–18 mg/g(d. w.)/hr, respectively. These values compare well with those obtained for *Monostroma* population in the present study.

Photosynthetic rate of *Monostroma* population on cloudy and rainy days, when diffuse light occupied a greater part of solar radiation, was higher than that on fine and cloudy-fine days, within the range lower than 200 kcal/m^2/hr. The same trend was recognized more clearly in terrestrial plants (KUMURA 1968); i. e. the population photosynthetic rate was consistently higher when the proportion of diffuse light was higher even under the same total light intensity. It was mainly based on more favorable light distribution within a population.

It was reported that the maximum standing stock of cultivated *Monostroma* population could reach 450–600 g/m^2 (MAEDA and OHNO 1972, MAEGAWA and ARUGA 1974). In cultivation grounds the harvest is carried out before the standing stock reaches a maximum. So, such a high standing stock as mentioned above is not observed generally in cultivation grounds. In the present study, the standing stock of *Monostroma* used for estimation was 180–192 g/m^2 just before harvest.

Daily net production, 9.8 g (d. w.)/m^2/day, of *Monostroma* population obtained on fine day in the present study was well equivalent to that of *Porphyra* population, 12.0 g(d. w.)/m^2/day, reported by SATOMI *et al.* (1967), and that of the most terrestrial plant communities (RYTHER 1959). However, it was higher than that of submerged plant communities, 6 g(d. w.)/m^2/day, obtained by IKUSIMA (1966).

From Fig. 12 it is noted that efficiency of gross production of *Monostroma* population was slightly higher than that mentioned by EDWARDS and OWENS (1962). In Table 1 the efficiency of daily net production, particularly on fine and cloudy-fine days, was equivalent to the maximum values found in most terrestrial plant communities, although the efficiency of gross production was at the level of average values.

The net production and its energy efficiency of *Monostroma* population are comparatively high to those of terrestrial plant communities even at low temperature in the winter cultivation season. This is so even though the photosynthetic rate is similar to that of submerged plant population in which it is 50–100% of the rate of land plants. Probably, this is mainly due to the fact that *Monostroma* population has not such non-photosynthetic tissues as roots and stems which are major components of terrestrial plants but is composed almost entirely of photosynthetic tissues. Thus, the 24 hr respiratory loss is small, so that the ratio of the net production to the gross production, P_n/P_g, shows a high value of 0.73 on fine day (Table 1), which has not been observed in terrestrial plant communities.

The net production and its energy efficiency in *Monostroma* population, therefore, attain such high values as mentioned above in spite of low temperature in the cultivation season. The daily net production ranged from 3.3 to 9.8 g(d. w.)/m^2/day and its energy efficiency varied from 2.1 to 1.2% according to weather conditions. It is concluded that the maximum rate of daily net production and its efficiency of *Monostroma* population in cultivation ground are almost at the same level as the maximum values found in most terrestrial plant communities mainly because of the low respiratory loss.

5. Summary

Diurnal changes in the population photosynthesis of cultivated *Monostroma* were investigated in relation to various weather conditions. The gross and net production and their energy efficiency were estimated.

(1) For measuring the population photosynthesis a large assimilation chamber was devised. Seawater was circulated in the chamber. Continuous measurements of photosynthesis, respiration and solar radiation were carried out for 25 hr on fine, cloudy-fine, cloudy and rainy days.

(2) Changes in photosynthetic rate showed a trend similar to that in solar radiation. The maximum photosynthetic rate of $12.1\ mgO_2/g$ (d. w.)/hr was reached under a solar radiation of 55 cal/cm^2/hr at noon on fine day. Respiratory rate in the night was kept at a constant

level of ca. 1.0 $mgO_2/g(d.w.)/hr$.

(3) The daily gross production and net production were 13.4–7.1 and 9.8–3.3 g(d.w.)/m^2/day, respectively. They varied according to the weather conditions.

(4) In spite of the low temperature condition of the cultivation season, maximum daily net production and its energy efficiency of *Monostroma* population were almost at the level equivalent to the maximum values observed in terrestrial plant communities. This high productivity was mainly attributed to a high P_n/P_g ratio, that is, the low respiratory loss.

Acknowledgement

The author wishes to express his sincere thanks to Dr. Y. ARUGA, Tokyo University of Fisheries, for valuable advice and encouragement. Thanks are also due to Mr. A. NAKANO who kindly helped the author in the experiments, and to Miss KATHLEEN TORKKO who kindly corrected English of the manuscript. This research was supported by a grant from Mie Prefecture.

References

BUESA, R.J. (1977): Photosynthesis and respiration of some marine plants. Aqua. Bot., **3**, 203–216.

DOTY, M.S. (1971): The productivity of benthic frondose algae at Waikiki beach, 1967. Univ. Hawaii, Bot. Sci. Paper, **22**, 1–119.

EDWARDS, R.W. and M. OWENS (1962): The effects of plants on river conditions IV. The oxygen balance of a Chalk Stream. J. Ecol., **50**, 207–220.

IKUSIMA, I. (1965): Ecological studies on the productivity of aquatic plant communities I. Measurment of photosynthetic activity. Bot. Mag. Tokyo, **78**, 202–211.

IKUSIMA, I. (1966): Ecological studies on the productivity of aquatic plant communities II. Seasonal changes in standing crop and productivity of a natural submerged community of *Vallisneria denseserrulata*. Bot. Mag. Tokyo, **79**, 7–19.

IKUSIMA, I. (1967): Ecological studies on the productivity of aquatic plant communities III. Effect of depth on daily photosynthesis in submerged macrophytes. Bot. Mag. Tokyo, **80**, 57–67.

JOHN, D.M. (1971): The distribution and net productivity of sublittoral populations of attached macrophytic algae in an estuary on the Atlantic coast of Spain. Mar. Biol., **11**, 90–97.

KING, R.J. and W. SCHRAMM (1976): Photosynthetic rate of benthic marine algae in relation to light intensity and seasonal variation. Mar. Biol., **37**, 215–222.

KUMURA, A. (1968): Studies on dry matter production of soybean plant (111). Photosynthetic rate of soybean plant population as affected by proportion of diffused light. Jap. Journ. Crop Sci., **37**, 570–582.

MAEDA, M. and M. OHNO (1972): On the productivity of *Monostroma* (green algae) community in the natural and cultivated ground. Rep. Usa Mar. Biol. Stat., **19**, 1–13.

MAEGAWA, M. and Y. ARUGA (1974): Studies on the growth and the variation of photosynthetic activity of cultivated *Monostroma latissimum*. La mer, **12**, 27–43.

ODUM, H.T. (1957): Primary production in flowing waters. Limnol. & Oceanogr., **1**, 102–117.

RYTHER, J.H. (1956): Potential productivity of the sea. Science, **130**, 602–608.

SATOMI, M., S. MATSUI and M. KATADA (1967): Net production and the increment in stock of the *Porphyra* community in the culture ground. Bull. Jap. Soc. Sci. Fish., **33**, 167–175.

YOKOHAMA, Y. (1973): A comparative study on photosynthesis-temperature relationships and their seasonal changes in marine benthic algae. Int. Revue ges. Hydrobiol., **58**, 463–472.

養殖ヒロハノヒトエグサ個体群の光合成と物質生産の測定

前　川　行　幸

要旨: 養殖ヒロハノヒトエグサ個体群の光合成の日変化と物質生産について，特に天候との関係を中心に研究を行った。個体群光合成測定のため大型同化循環水槽を作製し，流入海水と流出海水の溶存酸素の差および通水量から光合成速度および呼吸速度を求めた。測定は，快晴，晴れ一時曇り，曇り，雨の四つの天候について25時間連続して行った。

日中の光合成速度の変化は太陽放射の変化とよく一致し，快晴日の正午に 55 cal/cm^2/hr で 12.1 mg O_2/g(d.w.)/hr の最大光合成速度を示したが，光飽和には達していなかった。夜間の呼吸量は 1.0 mg O_2/g(d.w.)/hr でほぼ一定していた。

日総生産量と日純生産量はそれぞれ 13.4-7.1 g(d.w.)/m^2/day および 9.8-3.3 g(d.w.)/m^2/day で，天候条件により変化した。総生産と純生産のエネルギー効率は，快晴日でそれぞれ 1.6% および 1.2%，雨天日でそれぞれ 4.5% および 2.1% であった。養殖ヒロハノヒトエグサ個体群が，冬季の養殖期間の低い環境水温にもかかわらず，陸上の草原群落に匹敵する高い日純生産やエネルギー効率を示すことができるのは，高い P_n/P_g 比（快晴日において 0.73)，すなわち，低い呼吸損失によるものと考えられる。

La mer (Bulletin de la Société franco-japonaise d'océanographie)
Tome 18, N° 3, pp. 125 à 130, Août 1980

Some Modifications of the Grain Density Autoradiography in the Study of Phytoplankton Production*

Yoshio OGAWA** and Shun-ei ICHIMURA**

Abstract: Sources of inherent errors in the grain density autoradiography for measuring photosynthetic activity of individual species of phytoplankton community were checked using three different species of cultures. The development time of 6-12 min was suitable for obtaining steady grain count. The effect of chemography was reduced by no application of any fixative with gentle suction. Latent image erasure was completely excluded by shortening exposure time less than 7 days. Geometrical effect can be cancelled by counting all grains in a large distance of 40 μm from the cell surface. A good correlation was found between radioactivity/cell and grain counts/cell ($Y=587.06X+0.78$). The conversion of grain counts to absolute disintegration rate would be possible from the above regression correlation. If these careful processes are made, the grain density autoradiography can be employed as a useful measure of photosynthetic activity of phytoplankton species.

1. Introduction

As a useful tool for the determination of photosynthetic activity of individual species in phytoplankton assemblages, the grain density autoradiography has been employed by several investigators (WATT 1971, STULL *et al.* 1973, GUTELMACHER 1975), although BROCK and BROCK (1968) argued that this technique was not suitable for the quantitative study. KNOECHEL and KALFF (1976a, b) emphasized the serious errors arised from each step in the processes of grain density autoradiography and recommended an alternative technique, track autoradiography, for the quantification of individual species productivity. They pursued the population dynamics of freshwater phytoplankton diatom species by the track autoradiography (KNOECHEL and KALFF 1978). PAERL and STULL (1979) found a higher degree of correlation between the techniques of grain density and track autoradiography in study of natural phytoplankton community and claimed the validity of the grain density autoradiography.

As has been criticized by KNOECHEL and KALFF (1976a), the grain density autoradiography is easy technique but as yet its certainty has not been proved sufficiently. The purpose of the present paper is to check potential sources of error cited by KNOECHEL and KALFF (1976a) in the grain density autoradiography and scrutinize the utility of this technique for the study of species dynamics of phytoplankton community.

* Received April 17, 1980

** Institute of Biological Sciences, The University of Tsukuba, Sakura-mura, Ibaraki, 305 Japan

2. Materials and Methods

Unialgal cultures of *Cyclotella*, *Scenedesmus* and *Selenastrum* were used for the present study. Each 100 m*l* of algal suspension was taken in a 200 m*l* Erlenmeyer flask and injected with 0.3 m*l* $NaH^{14}CO_3$ solution having activity of 10 μCi/m*l*. Flasks were then incubated in a water bath under illumination of 30 Klux by white light fluorescent lamps at 20°C. Dark flasks were also prepared as controls. A series of samples were removed from flasks with pipettes at various time periods over 4 hrs. Each 5 m*l* of samples was filtered through a 24-mm HA Millipore filter with gentle suction and then the filter was washed with small volume of distilled water and fumed in HCl vapor. Total radioactivity of ^{14}C incorporated in algal cells was measured by a liquid scintillation counter (Beckman LS 8100). Cell numbers counted with Thoma's haemacytometer before and after the incubation were averaged and the mean cell number was used. Mean radioactivity per cell was calculated from dividing total radioactivity by cell number in the sample. For grain density autoradiographs each 2 ml of remaining samples was immediately filtered through 24-mm HA Millipore filter with gentle suction. In the present experiment no fixative was applied to avoid possible chemography and possible destruction of cells was also prevented. Each filter paper was attached to a microscope slide with 1% gelatin solution. The slide was then dried at 35°C for 24 hrs in an oven and cleared with acetone vapor. SAKURA NR-M2 nuclear emulsion melted at 37°C in a water bath in the dark was poured into a small container for slide dipping. Under the safety light, each slide was dipped in the emulsion for a few seconds and then withdrawn and dried in vertical setting for one hour under a small fan. After drying the slides were placed in a black plastic slide box containing dried silica gel. The boxes were stored at 4°C in a refrigerator during exposure of 2–10 days. Exposed slides were developed in developer (Konidol X Super) in staining vessel with standard vertical holder made of stainless steel. Development time varied from 3 to 24 minutes. Following development the slides were transferred to acetic acid stop bath for one minute and then fixed in acid hardening fixer (Konifix) for 10 min, washed gently in running tap water for 30 min. All the procedures were made in a water bath incubator at 20°C. Autoradiographs prepared in this way were photographed at 780 magnification using a microscope (Nikon Optiphoto) and grains on the photographs were counted. Background counts were estimated from slides prepared for dark bottle samples.

3. Results and Discussion

KNOECHEL and KALFF (1976a) argued that the number of produced grains and their spatial distribution are remarkably affected by the cell size and shape, despite the absolute radioactivity is identical. They proposed to count all grains within a certain distance from the cell including the half-distance, in which more than a half of produced sliver grains was located (SALPETER *et al.* 1969) and distance of 10 μm recommended for getting enough counts.

At the first step of this study, therefore, the distribution of grain around the cell was examined to delineate the area to be counted. Slides used for this experiment were exposed for 2 days and developed for 6 min. Radioactivity incorporated in the cells was 9.23×10^{-2} dpm/cell in *Cyclotella* sample and 8.05×10^{-2} dpm/cell in *Scenedesmus* sample. Grain counting was made on the microscopic photography along the band-area of every 10 μm width from the cell margin to 40 μm distance. As shown in Fig. 1, grains counted were mostly distributed in the area from the cell margin to 10 μm distance with the value of 82.3 in *Cyclotella* ample and 68.3 in *Scenedesmus* sample. The grain density, in which grains counted were ormalized by a unit area and expressed as

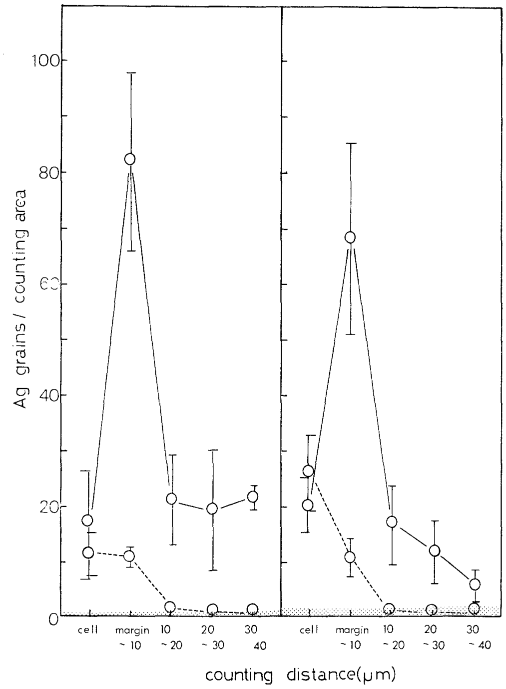

Fig. 1 The distribution of grains over the cell and surrounding area in *Cyclotella* (left) and *Scenedesmus* (right). Solid line, grain counts in each band area; dashed line, grain density/100 μm^2. Shaded place represents background (background grain counts/100 μm^2). Vertical line indicates 95% confidence limits.

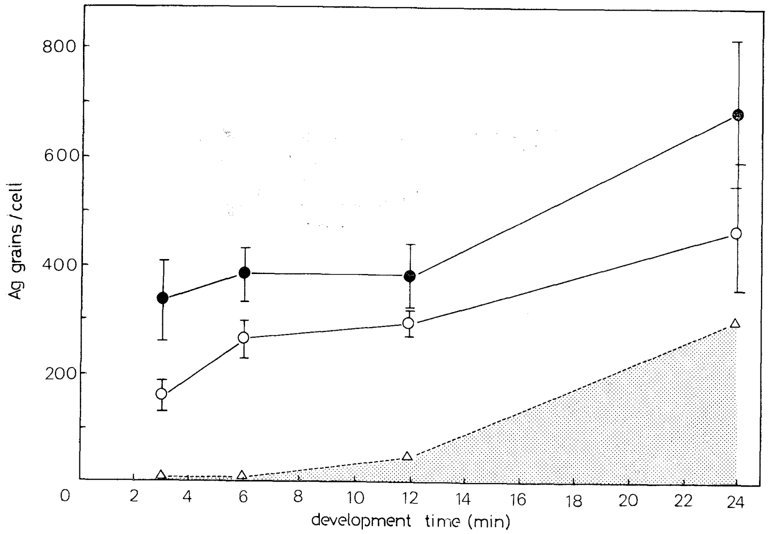

Fig. 2. Relationship between development time (min) and grain counts per cell in *Cyclotella*; 19.8×10^{-2} dpm/cell (○), 32.7×10^{-2} dpm/cell (●). Shaded area represents background counts. Vertical line indicates 95% confidence limits.

counts/100 μm^2, was the highest over the cell and decreased with increase of distance from the cell. The grains were reduced to background level of 1.0 grain/100 μm^2 in the area between 30-40 μm in *Cyclotella* and 1.5 grains/100 μm^2 in the area between 10-20 μm in *Scenedesmus*. This distribution pattern was also the same in the other samples exposed for longer time than 2 days.

It is generally noticed that the maximum path-length of a beta particle originated from a point source in nuclear emulsion is about 100 μm for ^{14}C. However, the grains in the outside of 40 μm from the cell were so small as negligible in the present counting. Therefore, a stable efficient counting will be made to a distance of 40 μm from the cell margin. In the following experiments, we counted all grains lying over the cell and outside of 40 μm from the cell.

It required a long exposure time to develop all latent images, but excess background count due to the prolonged development has led to the difficulty of counting the grains. Fig. 2 shows the relationship between development time (min) and grain count per cell for two samples of *Cyclotella*. The radioactivity was 19.8×10^{-2} dpm/cell in one sample and 32.7×10^{-2} dpm/cell in the other sample. Grain counts were increased with development time in both samples and reached the plateau after 6 min. Grain counts at the plateau were 383.8 grains/cell for high radioactive sample and 264.3 grains/cell for low radioactive sample. After 12 min, grain counts increased and reached the high level of 693.2 grains/cell for the former sample and 477.4 grains/cell for the latter sample. Background count remained at very low level (6.4 count/cell) during the first 6 min, thereafter it increased rapidly. From these results, it is inferred that the development time should not exceed 12 min. We adopted 6 min as development time because of the following reasons; grain count reaches plateau by this time and background count is negligible in contrast to grain counts.

In micro-autoradiography, silver grain had been expected to increase linearly with exposure time. However, prolonged exposure has resulted in the underestimation of grains due to possible latent image erasure of interference of excessively produced grains (ROGERS 1967). Fig. 3 shows the relationship between exposure time and grain counts in *Cyclotella* sample with radioactivity of 9.23×10^{-2} dpm/cell. Grain count proportionally increased with exposure time during the first 7 days, and subsequently it decreased gradually. Thus, it was revealed that exposure time was desirable to be limited at least within 7 days. Furthermore, grain counts per cell were desirable to be less than 450 counts for the exclusion of errors caused by the interference of the grains.

Photosynthetic activity of individual cells in the grain density autoradiography has been calculated from the apportionment of the total radioactivity to grains produced by each cell (WATT 1971, STULL *et al.* 1973, GUTELMACHER 1975). When phytoplankton assemblages consist of delicate species and nanoplankton and they are missed during the processes, this approach leads to an overestimation of the remaining species (KNOECHEL and KALFF 1976a). Thus, it is necessary to convert grain counts directly to absolute disintegration rate (dpm). KNOECHEL and KALFF (1976a) stated that it would be desirable to convert grain count into an absolute disintegration rate through an internal standardization procedure. This is made by the addition of specimens with known activity to the sample. However, another alternative method was examined in the present study because we had no suitable such reference sources. Fig. 4 shows the interrelationship between radioactivity/cell and grain counts/cell. A good correlation was found between the both parameters ($Y=587.06X+0.78$, $r=0.95$), thereby the produced grains will be strictly corresponded to radioactivity incorporated in the cell. It would be possible to convert the grain counts to absolute disintegration rate from the above regression equation.

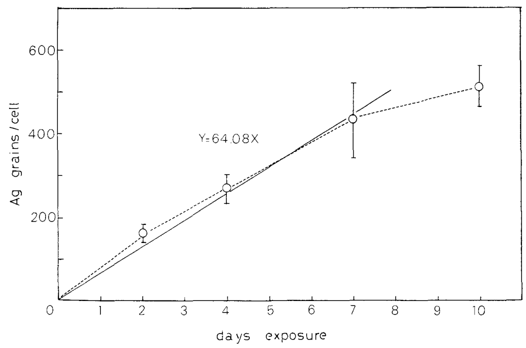

Fig. 3. Relationship between the length of exposure (days) and grain counts per cell in *Cyclotella* (9.23×10^{-2} dpm/cell). Vertical line indicates 95% confidence limits.

KNOECHEL and KALFF (1976a, 1979) criticized the grain density autoradiography and emphasized inherent sources of error in this method. However, most of sources of error may be cancelled by suitable processes. Careful prepa-

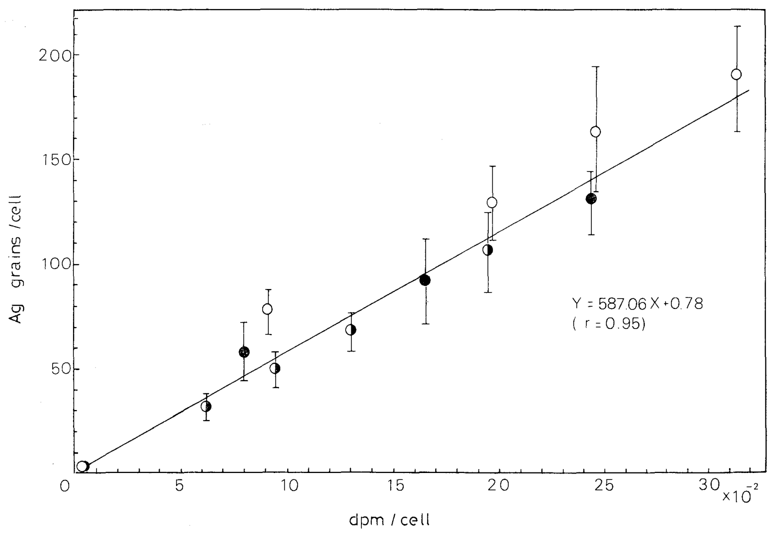

Fig. 4. Relationship between diel radioactivity (dpm)/cell and diel grain counts/cell in three different algal species; *Cyclotella* (○), *Scenedesmus* (●) and *Selenastrum* (◑). Vertical line indicates 95% confidence limits.

ration of samples and proper selection of fixatives are necessary in the grain density autoradiography as well as track autoradiography. Latent image erasure is also serious problem as cited by KNOECHEL and KALFF (1976a). Considerable attention must be payed on the chemography caused by fixatives and the effect of cell size and shape. Chemography was simply corrected by using dark bottle control and the intensive interference of the grain count by chemography is reduced by the present procedure. If the samples are carefully treated, the effect of chemography is probably eliminated. This is evident from a low level of background counts in Fig. 1. The effect of cell size and shape can be cancelled by counting all grains in a large distance of 40 μm from the cell.

It is difficult to convert the grain counts to absolute radioactivity. We calculated the absolute radioactivity from the linear relationship between radioactivity incorporated in the cell and produced grains. ROGERS (1967) has shown that this approach is suitable only for approximate estimation of absolute radioactivity. In this case, the inacuracy may be arised from the cross-fire effect of sources packed closely in tissue section. Since an algal cell is considered to be a single source, the cross-fire effect may be excluded in phytoplankton samples. A regression equation presented in the present study would be useful for the conversion of grain counts to absolute radioactivity of a cell. The grain density autoradiography can be employed as a useful means for measuring photosynthetic activity of individual phytoplankton species if the careful processes are made.

References

BROCK, T. D. and M. L. BROCK (1968): The application of micro-autoradiography techniques to ecological studies. Mitt. Int. Ver. Angew. Limnol., **15**, 1–29.

GUTELMACHER, B. L. (1975): Relative significance of some species of algae in plankton primary production. Arch. Hydrobiol., **75**, 318–328.

KNOECHEL, R. and J. KALFF (1976a): The applicability of grain density autoradiography to the quantitative determination of algal species production: A critique. Limnol. Oceanogr., **21**, 583–590.

KNOECHEL, R. and J. KALFF (1976b): Track autoradiography: A method for the determination of phytoplankton species productivity. Limnol. Oceanogr., **21**, 590–596.

KNOECHEL, R. and J. KALFF (1978): An *in situ* study of the productivity and population dynamics of five freshwater planktonic diatom species. Limnol. Oceanogr., **23**, 195–218.

KNOECHEL, R. and J. KALFF (1979): The advantages and disadvantages of grain density and track autoradiography. Limnol. Oceanogr., **24**, 1170–1171.

PAERL, H. W. and E. A. STULL (1979): In defense of grain density autoradiography. Limnol. Oceanogr., **24**, 1166–1169.

ROGERS, A. W. (1967): Techniques of autoradiography. Elsevier, Amsterdam. 338 pp.

SALPETER, M.M., L. BACHMANN and E.E. SALPETER (1969): Resolution in electron microscope radioautography. J. Cell. Biol., **41**, 1–20.

STULL, E. A., E. DE AMEZAGA and C. R. GOLDMAN (1973): The contribution of individual species of algae to primary production of Castle Lake, California. Int. Ver. Theor. Limnol., **18**, 1776–1783.

WATT, W. D. (1971): Measuring the primary production rate of individual species in natural mixed populations. Deep-Sea Res., **18**, 329–339.

植物プランクトン生産研究のための粒子密度オートラジオグラフ法の改良

小 川 吉 夫, 市 村 俊 英

要旨: 植物プランクトン群集を構成する個々の植物プランクトン種の光合成活性を粒子密度オートラジオグラフ法によって定量する際, その定量性を減少させる諸原因について考察し, それらを解消するための手段を検討した。

現像時間は6～12分が適当であり, これによって安定した銀粒子計数を得ることができた。ケモグラフィーの影響は, 固定剤をいっさい用いずに試料を低圧で沪過することにより排除することが可能である。潜像の退行は, 露光時間が7日以内であれば生じないことが明らかとなった。細胞の大きさ及び形状による銀粒子計数への影響は, 銀粒子計数を細胞の外側 40 μm にまで実施することで解消された。また, 細胞当りの ^{14}C の平均取込み量と細胞当りの銀粒子計数の間に, 高い相関 ($Y=587.06X+0.78$ $r=0.95$) が認められた。この回帰式を用いて銀粒子計数を絶対崩壊量(dpm)に変換することが可能で, 比例配分で求める際に生ずる誤差を除くことができると思われる。

以上のような手続きを考慮すれば, 粒子密度オートラジオグラフ法は, 個々の植物プランクトン種の光合成活性を定量するための有効な手段となり得ると思われる。

La mer (Bulletin de la Société franco-japonaise d'océanographie)
Tome 18, N° 3, pp. 131 à 137, Août 1980

Diffusion of Manganese from Bottom Sediments in Beppu Bay*

Kichiichiro KAWANA**, Takayuki SHIOZAWA**, Akira HOSHIKA**,
Terumi TANIMOTO** and Osamu TAKIMURA**

Abstract: A simultaneous measurement of the concentration of particulate manganese and beam attenuation coefficient was obtained in Beppu Bay. The measured beam attenuation coefficient was then converted to the concentration of particulate manganese using a laboratory calibration curve in the hope that the former can be used as a possible indicator of the latter. The mean flux of manganese across the sediment-water interface from July to October in this bay was estimated to be 12.6 $\mu g\ cm^{-2}\ day^{-1}$. The vertical eddy diffusivity in the bottom water layer was estimated from temporal variation of the vertical distribution of manganese.

1. Introduction

It is often observed that dissolved oxygen content in bottom layer of coastal waters decreases during summer and, as a result, some elements diffuse out of bottom sediments into seawater. Diffusion of manganese from reducing sediments is a well-known phenomenon. The very high concentration of dissolved manganese in pore water of nearshore sediments has been well decumented (CALVERT and PRICE 1972, DUCHART *et al*. 1973). Diffusion of manganese from bottom sediments may be important in the coastal balance of that element. GRAHAM *et al*. (1976) measured the flux of manganese across the sediment-water interface in Narragansett Bay and discussed the effect of that on the coastal manganese balance. KREMLING and PETERSEN (1978) showed that the high concentration of manganese in bottom waters of the Black Sea was caused by diffusion out of bottom sediments. Dissolved manganese diffused into bottom water may be oxidized as it comes into contact with more oxidized water and precipitate as particulate form. YEATS *et al*. (1979) reported that maximum concentration of dissolved manganese in the Gulf of St. Lawrence was observed close to sea bottom whereas the highest concentration of particulate manganese occurred 30–100 meters above the bottom. The elevated concentrations were attributed to diffusion of dissolved manganese from bottom sediments and its subsequent precipitation in the water column.

Beppu Bay is located at the western part of the Seto Inland Sea of Japan and is 60 to 70 meters deep, whereas at its mouth it is only 40 meters deep. In early summer a strong thermocline is formed at a depth around 50 to 60 meters and inhibits mixing between top and bottom layers, resulting in depletion of dissolved oxygen content from the bottom layer. SHIOZAWA *et al*. (1977), in their study of this bay, reported an observation of a coincident occurrence of manganese diffusion and depletion of oxygen content. They concluded that dissolved manganese was oxidized slowly as it came into contact with more oxidized water and precipitated as particulate manganese which was sharply concentrated around the thermocline.

We report herein measurements of the beam attenuation coefficient of seawater in this bay which exhibits a sharp peak value at the same depth of the peak concentration of particulate manganese and an investigation of the exact relation between the concentration of particulate manganese and the beam attenuation coefficient; the latter as a possible indicator of the former. We will estimate the flux of manganese across the sediment-water interface in this bay and the vertical eddy diffusivity in the bottom water layer from temporal variation of the vertical

* Received January 10, 1980
** Government Industrial Research Institute of Chugoku, Hiromachi 15000, Kure City, Hiroshima, 737-01 Japan

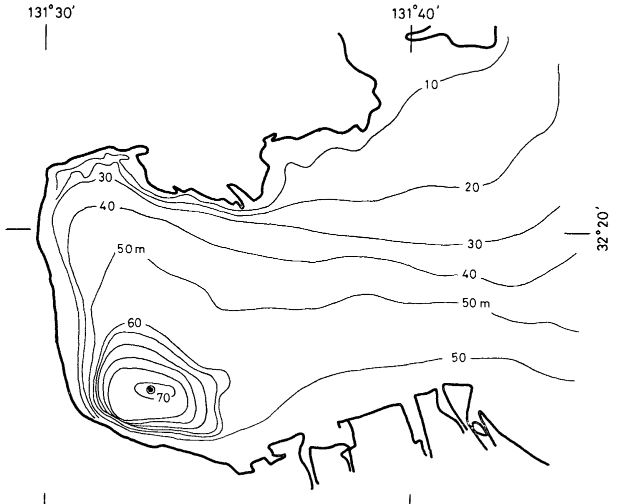

Fig. 1. Sampling station.

distribution of manganese.

2. Method

Water samples were collected with a 6-liter Van-Dorn sampler and immediately filtered through 0.45-μm Millipore filters. The filtrate was analyzed for dissolved manganese. Each filtrate was acidified with concentrated hydrochloric acid to a pH of approximately 2.0. Concentration of dissolved manganese was determined within a month of sampling in the laboratory by the atomic absorption procedure, using DDTC-MIBK extraction. Very high concentrations of dissolved manganese were obtained by a colorimetric procedure, using formaldoxime. Samples collected on the filters were used to determine concentration of particulate manganese. To each sample was added 5 ml of concentrated nitric acid and the solution was dried up. To this sample was added 2 ml of concentrated hydrochloric acid and the solution was dried up again. Finally to each sample was added 0.1 ml of concentrated hydrochloric acid and the solution was diluted with distilled water to 10 ml. Samples thus treated were analyzed by the atomic absorption procedure. Concentration of total manganese was obtained as the sum of dissolved and particulate manganese.

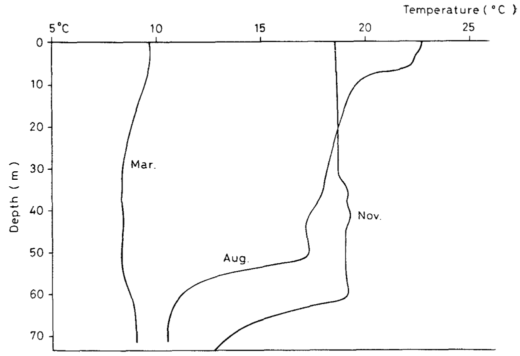

Fig. 2. Vertical distributions of water temperature in August and November 1976 and March 1977 in Beppu Bay.

The beam attenuation coefficient of seawater was measured by an *in situ* beam transmittance meter. The general outline of this apparatus is the same as the one described by JERLOV (1976). In our meter the light path is 50 cm.

3. Results and discussion

Sampling station was taken at the center of the deep in Beppu Bay (Fig. 1). Water samples were collected on July 4, August 4, October 7, November 20, 1976 and March 20, 1977. Fig. 2 shows vertical distributions of water temperature obtained on August 4, November 20 and March 20. A strong thermocline is observed at a depth around 50 to 60 m from August to November.

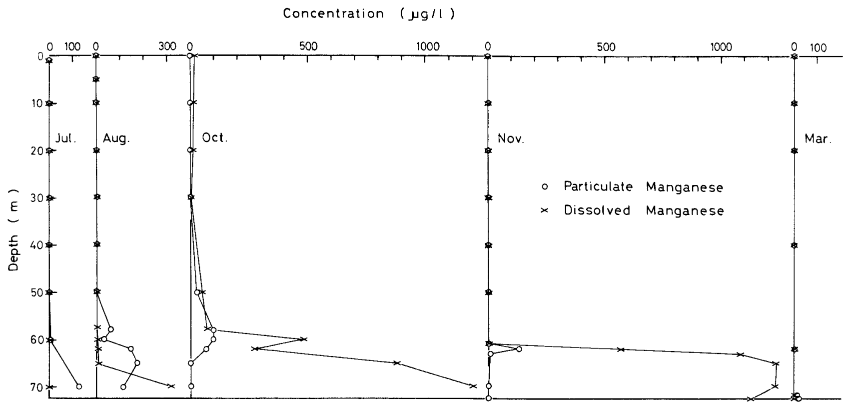

Fig. 3. Vertical distributions of dissolved and particulate manganese on July 4, August 4, October 7 and November 20, 1976 and March 29, 1977 in Beppu Bay.

This thermocline inhibits mixing between top and bottom waters and results in a coincident occurrence of oxygen depletion in the bottom water and manganese diffusion from bottom sediments.

Fig. 3 shows vertical distributions of manganese concentration in dissolved and particulate phases. Fig. 3 shows that manganese diffuses out of sediments and the concentration in dissolved phase increases from July to November, due to the persistent thermocline during this season. Part of dissolved manganese is oxidized slowly in seawater and precipitates as particulate manganese. The particulate manganese then is transported downward by the gravity and dissolves again as it makes contact with deoxidized water. Therefore, the vertical distribution of particulate manganese is determined by that of dissolved oxygen content.

(1) *Beam attenuation coefficient and particulate manganese*

Vertical distributions of beam attenuation coefficient of seawater are given in Fig. 4 which shows, except for surface layer, uniform values down to a depth of about 55 m, below which sharp peaks are observed. These peaks coincides with the peak concentrations of particulate manganese. HOSHIKA *et al.* (1978) observed that the precipitate of iron was concentrated also around the thermocline, although its concentration was lower than particulate manganese. We therefore examined the relation between the concentration of particulate manganese and the beam attenuation coefficient in the laboratory.

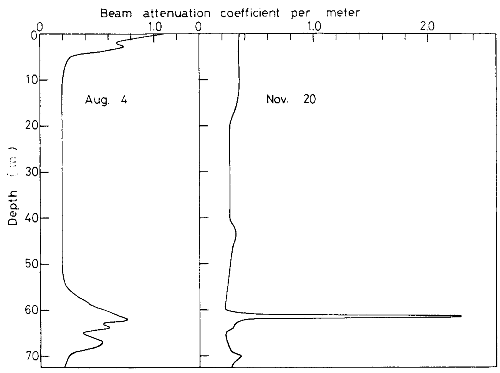

Fig. 4. Vertical distributions of beam attenuation coefficient on August 4 and November 20, 1976.

Particulate manganese in seawater most probably consists of MnO_2. Particulate manganese was prepared as MnO_2 in the laboratory by the method due to WEIJDEN (1976), i.e. 0.1 mole manganese chloride and 0.065 mole potassium permanganate were allowed to react in 400 ml of 1 mole acetic acid at 60°C. The diameter of particulate manganese thus formed was measured by a Coulter counter and was in the range of 3 μm to 10 μm. The beam transmittance meter was submerged in distilled water and the laboratory-formed particulate manganese was added to it. The water was then filtered through a 0.45-μm Millipore HA filter. Concentration of the particulate manganese was determined by the same

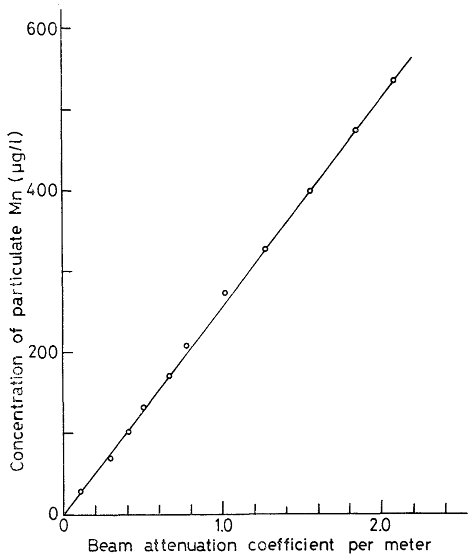

Fig. 5. Relation between concentration of particulate manganese and beam attenuation coefiicient.

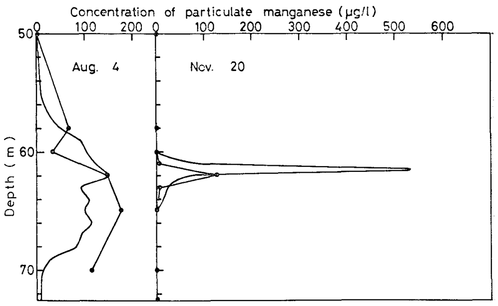

Fig. 6. Comparison of vertical distributions of particulate manganese converted from the beam attenuation coefficient and these measured. Filled marks indicate meaured values.

procedure as was employed for the Beppu Bay sample.

The relation between the concentration of particulate manganese and the beam attenuation coefficient, which is shown in Fig. 5, follows a straight line within the experimental range. We wish to estimate concentration of particulate manganese from beam attenuation coefficient measured *in situ*, say Fig. 4, using an experimental result of Fig. 5. The excess beam attenuation coefficient of peak values which appears below a depth of 55 m over uniform values above this depth is converted to concentration of particulate manganese.

Fig. 6 shows comparison of vertical distribution of particulate manganese thus converted and those measured. In November 20 data, the converted concentration of particulate manganese is higher than the measured. The peak beam attenuation coefficient measured on November 20 was found at a depth of 61.5 m and a thickness of the concentrated layer was only in the range of 1 m. Water sample we collected at this depth, on the other hand, had a concentration of particulate manganese considerably smaller than the peak value because water was sampled through a layer of about 1 m. Exclusive to this depth, the converted concentration agrees qualitatively with the measured. We therefore conclude that, using the beam transmittance meter, concentration of particulate manganese in Beppu Bay can be estimated easily and continuously in depth, whereas such is not the case with water sampling method.

SPENCER *et al.* (1971, 1972) found existence of particulate manganese just above the oxygen zero boundary in the Black Sea, which was the world's largest anoxic basin. There, the oxygen zero boundary was dome shaped, being at 110 m depth in the center of the basin and at about 275 m toward the shelves. On the other hand, according to the vertical distribution of beam attenuation coefficient in the central region of the Black Sea reported by NEUYMIN (1970), a thin layer of large beam attenuation coefficient was observed at depth of 120 to 170 m. This layer lay directly under the region of unstable temperature gradient which formed the lower boundary of the intermediate cold water. As this layer appears to coincide with the layer of manganese precipitating, we believe that the Black Sea is possibly another example where particulate manganese distribution can be inferred from beam attenuation coefficient.

(2) *The flux of manganese across the sediment-water interface*

The flux of manganese across the sediment-water interface is estimated as the following. Manganese transported upward across the thermocline may be oxidized and precipitate as particulate manganese, because of the oxygenated

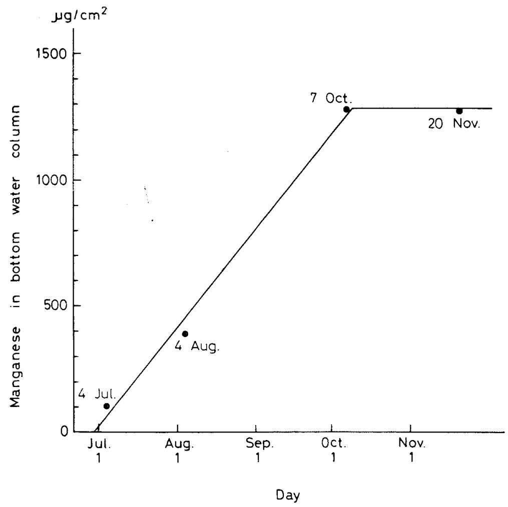

Fig. 7. The amount of total manganese in bottom water column per unit area below the thermocline.

top water. The precipitate may be transported again in the bottom water by its gravity. The amount of manganese in top water column above the thermocline is relatively small compard to that in bottom water column. Therefore, we assume herein that upward flux of manganese across the thermocline is of negligible order. The flux of manganese across the sediment-water interface is an increasing rate of total manganese in bottom water column per unit area below the thermocline. The amounts of total manganese in bottom water column per unit area in each month are given in Fig. 7. Fig. 7 shows that the amount of total manganese in bottom water column increases from July to October at a constant rate. The mean flux of manganese across the sediment-water interface during this season can be determined by least square method, which yields $12.6\,\mu g\,cm^{-2}\,day^{-1}$. This flux is a few times as large as the result of GRAHAM *et al.* (1976) in Narragansett Bay. It is also recognized from Fig. 3 that diffusion of manganese from bottom sediments sets in at the end of June.

From October to November, the amount of total manganese in bottom water column is almost unchanged. It is confirmed by our observed result in 1977 that the amount of manganese after November remains at the same level. It may be considered that diffusion from bottom sediments is completed before November.

We will analyze herein temporal variation of the vertical distribution of total manganese from July to November. We consider now the bottom water layer below the thermocline, in which manganese enters at a constant rate F_0 over unit area of sea bottom and there is no diffusion across the thermocline. We take an origin at the top of the thermocline and the z axis in the downward direction. The distance from the origin to sea bottom is taken to be l. l in this paper is determined to be 15 m which is the average value obtained from the vertical distributions of temperature in July, August and November. A part of dissolved manganese diffused into bottom water is oxidized and precipitated as particulate manganese. We assume that the effect of settling velocity of particulate manganese on the transport of total manganese can be neglected. Assuming also that the horizontal gradient of concentration and the vertical water movement are of negligible order, the diffusion equation of total manganese in the bottom water is given as follows:

$$\frac{\partial S}{\partial t}=K\frac{\partial^2 S}{\partial z^2}, \qquad (1)$$

where S is total manganese concentration, z is distance from the origin, t is time and K is the vertical eddy diffusivity. The boundary conditions may be written as follows:

$$K\frac{\partial S}{\partial z}=F_0 \qquad z=l \qquad t\geqslant 0 \qquad (2)$$

$$\frac{\partial S}{\partial z}=0 \qquad z=0 \qquad t\geqslant 0 \qquad (3)$$

If the initial concentration is zero throughout the bottom water and K is a constant value, we obtain the following solution.

$$S(z,t)=\frac{F_0 l}{K}\left\{\frac{Kt}{l^2}+\frac{3z^2-l^2}{6l^2}-\frac{2}{\pi^2}\times \sum_{n=1}^{\infty}\frac{(-1)^n}{n^2}\exp\left(-\frac{Kn^2\pi^2 t}{l^2}\right)\cos\frac{n\pi z}{l}\right\} \qquad (4)$$

Diffusion of manganese from sea bottom may be completed before November as mentioned

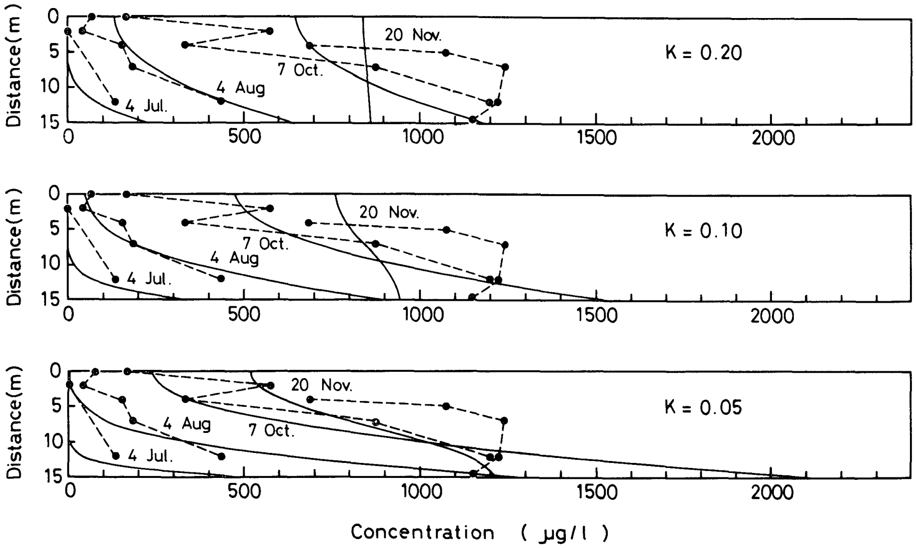

Fig. 8. Comparisons of temporal variation of vertical distribution of measured manganese and theoretical result.

above. In case of no diffusion from bottom sediment, the boundary condition at $z=l$ may be written as follows:

$$\frac{\partial S}{\partial z}=0 \qquad z=l \qquad (5)$$

When diffusion of manganese from sea bottom is completed, the vertical distribution in bottom water is taken as $f(z)$. The vertical distribution after the time t' from the completion may be obtained as follows:

$$S(z,t')=\frac{1}{l}\int_0^l f(z')dz'+\frac{2}{l}\sum_{n=1}^{\infty}\exp\left(-\frac{Kn^2\pi^2t'}{l^2}\right)\times\cos\frac{n\pi z}{l}\int_0^l f(z')\cos\frac{n\pi z'}{l}dz' \qquad (6)$$

Assuming from the result of Fig. 7 that diffusion of manganese from bottom sediment sets in on June 29 and is completed on October 10, we calculate the vertical distribution of total manganese at July 4, August 4 and October 7 from (4) and November 20 from (6). Comparisons of calculated results for $K=0.05$, 0.1 and 0.2 $cm^2\,sec^{-1}$ and measured values are shown in Fig. 8. Fig. 8 shows that the temporal variation of vertical distribution of measured values agrees qualitatively with the theoretical prediction. The theoretical concentration in November is lower than the measured value. This difference may be caused by the following reason. The distance l between the top of the thermocline and sea bottom varies with time, whereas in the theoretical result, Fig. 8, l is assumed constant. The practical distance in November is less than that constant. Therefore, the theoretical result may be lower than the measured value. The vertical eddy diffusivity in the bottom water layer is estimated to be 0.1–0.2 $cm^2\,sec^{-1}$. ROETHER *et al.* (1970) and ROOTH and OSLAND (1972) estimated the eddy diffusivities, which ranged from 0.2 to 0.75 $cm^2\,sec^{-1}$, in the thermocline from the tritium distribution. EPPLEY *et al.* (1979) calculated the eddy diffusivities in the thermocline of coastal water off southern California ranging 0.05 to 0.6 $cm^2\,sec^{-1}$ from nitrate data. KING and DEVOL (1978) calculated also a similar range of values (0.05–1.1 $cm^2\,sec^{-1}$) in the eastern tropical Pacific. The eddy diffusivity in the bottom water layer is of the same order as the recent calculated results in the thermocline.

References

CALVERT, S. E. and N. B. PRICE (1972): Diffusion and reaction profiles of dissolved manganese in the

pore waters of marine sediments. Earth Planet. Sci. Lett., **16**, 245-249.
DUCHART, P., S. E. CALVERT and N. B. PRICE (1973): Distribution of trace metals in the pore waters of shallow water marine sediments. Limnol. Oceanogr., **18**, 605-610.
EPPLEY, R. W., E. H. RENGER and W. G. HARRISON (1979): Nitrate and phytoplankton production in southern California costal waters. Limnol. Oceanogr., **24**, 483-494.
GRAHAM, W. F., M. L. BENDER and G. P. KLINKHAMMER (1976): Manganese in Narragansett Bay. Limnol. Oceanogr., **21**, 665-673.
HOSHIKA, A., O. TAKIMURA and T. SHIOZAWA (1978): Vertical distribution of particulate manganese and iron in the Beppu Bay. J. Oceanogr. Soc. Japan, **34**, 261-264.
JERLOV, N. G. (1976): Marine Optics. Elsevier, Amsterdam. 231 pp.
KING, F. D. and A. H. DEVOL (1979): Estimates of vertical eddy diffusion through thermocline from phytoplankton nitrate uptake rates in the mixed layer of the eastern tropical Pacific. Limnol. Oceanogr., **24**, 645-651.
KREMLING, K. and H. PETERSEN (1978): The distribution of Mn, Fe, Zn, Cd and Cu in Baltic seawater; a study on the basis of one anchor station. Mar. Chem., **6**, 155-170.
NEUYMIN, H. G. (1970): Inhomogeneities of optical properties in deep ocean water. J. Opt. Soc. Am., **60**, 690-693.
ROETHER, W., K. O. MUNNICH and H. G. OSTLUND (1970): Tritium profile at the North Pacific (1969) GEOSECS Intercalibration Station. J. Geophys. Res., **75**, 7672-7675.
ROOTH, C. G. and H. G. OSTLUND (1972): Penetration of tritium into the Atlantic thermocline. Deep-Sea Res., **19**, 481-492.
SHIOZAWA, T., K. KAWANA, A. HOSHIKA, T. TANIMOTO and O. TAKIMURA (1977): Vertical distribution of heavy metals and their seasonal variations in Beppu Bay. J. Oceanogr. Soc. Japan, **33**, 350-356.
SPENCER, D. W. and P. G. BREWER (1971): Vertical advection diffusion and redox potentials as controls on the distributon of manganese and other trace metals dissolved in waters of the Black Sea. J. Geophys. Res., **76**, 5877-5892.
SPENCER, D. W., P. G. BREWER and P. L. SACHS (1972): Aspects of the distribution and trace element composition of suspended matter in the Black Sea. Geochem. Cosmochim. Acta, **36**, 71-86.
VAN DER WEIJDEN, C. H. (1976): Experiments on the uptake of zinc and cadmium by manganese oxides. Mar. Chem., **4**, 377-387.
YEATS, P. A., B. SUNDBY and J. M. BEWERS (1979): Manganese recycling in coastal waters. Mar. Chem., **8**, 43-55.

別府湾における海底堆積物からのマンガンの拡散

川名吉一郎，塩沢孝之，星加　章，谷本照己，滝村　修

要旨: 瀬戸内海の別府湾で，海水の消散係数と粒子態マンガンの測定を行なった。底層水中に見られた消散係数の極大値は粒子態マンガンによるものと考えられたので，実験で求めた検量線から消散係数の極大値を粒子態マンガン濃度に変換した。変換された濃度は実測値とよく一致しており，別府湾では，消散係数は粒子態マンガンのよい指標になることがわかった。

7月から10月にかけての海底からのマンガンの溶出量は 12.6 $\mu g\ cm^{-2}\ day^{-1}$ であった。また，底層での鉛直拡散係数がマンガンの鉛直分布の時間変動から推定された。

La mea (Bulletin de la Société franco-japonaise d'océanographie)
Tome 18, N° 3, pp. 138 à 152, Août 1980

寄　　稿

透明度測定に関する諸問題の考察*

福田雅明**，津田良平***

Consideration of Problems in Transparency Measurements*

Masaaki FUKUDA** and Ryohei TSUDA***

Abstract: The theory and practice of transparency measurements are discussed. The Secchi disk is a popular instrument for measuring transparency because of its simple structure and the universal results it gives on the optical characteristics of seawater.

It is proven, in theory, that the disappearance depth of the Secchi disk, i.e. the transparency, is little influenced by the personal threshold of visibility or the reflectance of the disk. Using a black disk together with a Secchi disk, the threshold, the same value as used in meteorology, and the back scattering function were evaluated. The decrease of transparency from reflected sky light and the transparency in the case of an inclined rope are discussed theoretically.

In order to examine the size effect of Secchi disks, some experiments were carried out, and it was found that the size of the disks had very little influence on the measurements (of the transparency). Using factors obtained before, the fading and the contrast of the Secchi disk were calculated. The results agree closely with the results of the measurements.

1. はしがき

透明度板を用いて透明度を測定する方法は，古くから海洋観測に用いられてきた。最近，色々精巧な測定器が開発され，海中の光の測定や濁りの測定に利用されて来た。しかし，それらは必ずしも誰でもが利用できる普及した測定器とはなっていない。透明度は，ロープと 30 cm の白円板，そして，下に錘りを付けるだけのもので手作りでも製作でき，持ち運びが容易である。測定は夜でなければ誰にでもできるので，測明度の測定は一般の海洋観測では必ず測定項目に組込んでいる。このように一般化された理由は前に述べたほかに，透明度が天候や測定者によってあまり大きく左右されず，海水中の光の透過率や散乱率（いずれもその海水固有の性質）に大きく依存するからである。この特徴は，後で詳細に述べるが，海水の性質を観測し，海況を論ずる時に，客観的指標として利用できる値を得ることを示しているので，透明度測定が衰えることなく続いているものと考えられる。

このように便利で信頼性のある測定法の透明度に関する理論があまりない。竹内 (1950)[1] は光の波長が透明度に及ぼす影響について論じた。NANNITI (1953)[2] は，光の海水中での消散係数，散乱係数，透明度板の反射率，海面での反射率，測定者の眼の識別閾値をパラメータに透明度の式

* 1979年9月20日受理 Received September 20, 1979
** 日本原子力研究所東海研究所環境安全研究部
〒319-11 茨城県東海村白方白根 2-4
Japan Atomic Energy Research Institute, Tokai-mura, Naka-gun, Ibaraki-ken, 319-11 Japan
*** 近畿大学農学部水産学科，〒577 大阪府東大阪市小若江 3-4-1 Faculty of Agriculture, University of Kinki Kowakae 3-4-1, Higashi-Osaka City, Osaka, 577 Japan

を導き観測値と比較して論じた。TYLER (1968)[3]は透明度板による透明度から光束消散係数と分散光消散係数の和の推算を行った。

透明度板は白色 30 cm の円板と決められているが，筆者等は竹内[1]の色付透明度板の考えをさらに進めて，黒色の透明度板ならば透明度がどうなるかについて考えて見た。さらに，現場で観測する時の条件や状態を考慮した透明度の問題について，理論的面と測定結果とから検討を行った。

「海洋観測指針」(気象庁 1970)[4]によると，透明度の測定は次のようである。直径 30 cm の白色の平らな円板を海水中に降ろし，見えなくなる限界の深さを m 単位で表わすとなっている。板の表面は白色のつや消しラッカーで塗装し，よごれがないようにする。測定には，日陰で太陽や天空の海面からの反射のない（船影を利用するなど）海面を通して透明度板を見るようにする。表面に薄く濁った水が浮んでいるなど，水が一様でない場合には透明度を測っても大して意味がない。透明度板が鉛直に下がらないで斜めにロープが傾いている時は，透明度板の水深を透明度とせず，繰り出したワイヤの長さを透明度とし，ワイヤの傾角を付記する。

以上が，測定法であるが，この中にいくつかの問題点を含んでいる。すなわち，30 cm 以外の大きさの透明度板を使用した場合，白色以外の色を付けた場合，天空の海面からの反射光が目に入った場合（実際の観測には良くある），表層でなく中間あるいは下層に濁った又は澄んだ水があるような場合，透明度板のロープがかなり傾いた場合等である。そのほか，太陽高度，雲の状態，浅い水深，波のある場合等多くの問題がある。

これ等の問題のうち，透明板の色については竹内 (1950)[1]が研究しているので，ここでは割愛する。また，鉛直的に海中の状況が一様でない場合，太陽高度，雲の状態，浅い水深，波のある状態などについては，それらの条件があまり複雑なのでこの論文ではふれないことにする。

透明度の問題は海洋における水塊分析，水中懸濁物の解析等に応用することができる。特に，沿岸域においては水の性質の変化が大きいので透明度がそれらの良い指標になる。このような簡単な器具は誰にでも作ることができるので，産業と結び付く沿岸の環境問題においては良い測定機器となるのであろう。

環境問題に関しては，生態系との関係が重要であるから，海中照度と生物との関係，懸濁物とモニタリングの関係などが直接的に関連を持ってくる。さらに，上空から海水中の観測をしたり，染料拡散実験等の解析にも透明度の問題は応用され得る。

透明度の問題は基礎的なものであるが，その応用は非常に広く，この理論をさらに発展することにより，原子力も含めた環境調査の解析の良い手法となると考えられる。

2. 透明度の理論

2.1 白色透明度板

Fig. 1 に示すような透明度測定のモデルを考える。天空よりの入射光束は一部海面で反射しながら海中に投入する。海中に投入された光は，海水とその中の懸濁物質とによってその一部が消散さ

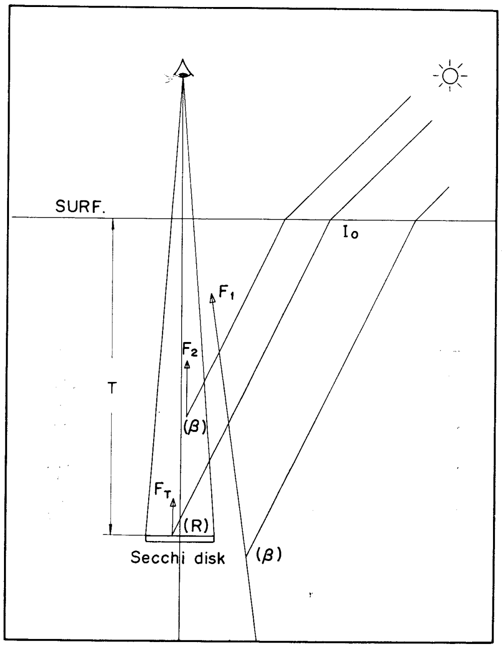

Fig. 1. Schematic diagram of transparency measurement.

れたり吸収されたりしながら下方に進む。下方に進む光の照度は照度計により測定され，照度の深さによる減衰率から分散光消散係数 $K(\mathrm{m}^{-1})$ が計算される。理論的には，K を与えることにより，ある深さ（Tm）の下向きの光の照度が計算される。

$$I(T)=I_0\exp(-KT) \qquad (1)$$

ここで，I_0 は海面直下の照度である。この透明度の理論においては，海面が滑らかであり，海水は表面から無限大の深さまで光学的に均一であると仮定する。

透明度板上 ds の面積に投射される光の照度を Ids とすれば，海面の方向への透明度板の輝度は次式で表わされる。

$$E_T=\frac{AIds}{\pi ds}=\frac{A}{\pi}I_0\exp(-KT) \qquad (2)$$

ここで，A は反射係数 (str^{-1}) である。

透明度板から反射された光は海水中で消散されながら上方に進み，眼に入って網膜上に像を結ぶ。その像の照度は，

$$F_T=\frac{\pi}{4}E_T\left(\frac{\phi}{f}\right)^2\exp(-\alpha T)$$
$$=\frac{A}{4}I_0\left(\frac{\phi}{f}\right)^2\exp\{-(\alpha+K)T\} \qquad (3)$$

で計算される。ここで，ϕ は眼の有効口径 (m)，f は眼の焦点距離 (m)，α は光束消散係数 (m^{-1}) である。この計算では，海中から空中に出る時の光の反射・屈折は省略した。この光は眼で像を結ぶ光なので α を消散係数として用いる。

海面から下方に進む光は海中の懸濁物等によって眼の方向に散乱され，その一部は眼に入射され，網膜に像を結ぶ。海中で散乱された光が懸濁物によってさらに散乱された光もあるが，ここでは多重散乱は考えないことにする。簡単のため，眼は海面にあると仮定する。

眼に入る光を2つに分ける。1つは透明度板上の海水から来る光 (F_2) であり。もう1つは透明度板の周りから来る光 (F_1) である。前者は眼の網膜上で透明度板から来る光に加算される。この加算のされ方は，正確には，4. の透明度板のボケの問題で述べるような重ね合わせを行うが，ここでは近似的に散乱した方向の網膜上に像を結ぶと仮定して行う。

透明度板が見えなくなるのは，透明度板の方向から来て網膜上に結んだ像の照度 (F_T+F_2) と，透明度板の周辺から来た光の網膜上の照度 (F_1) との差を F_1 又は (F_T+F_2) で割った値が，ある値 (σ) より小さくなった時であると考えられている。すなわち，

$$\gamma=\frac{F_T+F_2-F_1}{F_1}\leq\sigma \qquad (4)$$

である。ここで，σ は識閾 (threshold) であり，透明度板が見えなくなった時，丁度，$\gamma=\sigma$ となる。

F_1，F_2 の値は次式で計算される。

$$F_1=\frac{\pi}{4}I_0\beta\left(\frac{\phi}{f}\right)^2\int_0^\infty\exp\{-(\alpha+K)z\}dz$$
$$=\frac{\pi}{4}\frac{I_0\beta}{(\alpha+K)}\left(\frac{\phi}{f}\right)^2 \qquad (5)$$

$$F_2=\frac{\pi}{4}\frac{I_0\beta\left(\frac{\phi}{f}\right)^2}{(\alpha+K)}[1-\exp\{-(\alpha+K)T\}] \qquad (6)$$

ここで，β は下向きに進む光の眼の方向への散乱係数 ($\mathrm{m}^{-1}\cdot\mathrm{str}^{-1}$) である。$\beta$ は正確には散乱角によるが，この問題では後方散乱のみを問題にするので，方向依存性がないものと仮定する。

透明度板が見えなくなった時の深さを Tm とすれば，(2)，(4)，(5)，(6) 式から次の関係式が導かれる。

$$\frac{\left(\frac{A}{\pi}-\frac{\beta}{\alpha+K}\right)\exp\{-(\alpha+K)T\}}{\frac{\beta}{\alpha+K}}=\sigma \qquad (7)$$

$$(\alpha+K)T=\ln\left(\frac{\frac{A}{\pi}-\frac{\beta}{\alpha+K}}{\frac{\sigma\beta}{\alpha+K}}\right) \qquad (8)$$

2.4 で述べるように，$\beta/(\alpha+K)$ は A/π に比べ2桁以上小さい値をとるので省略すると，(8) 式は

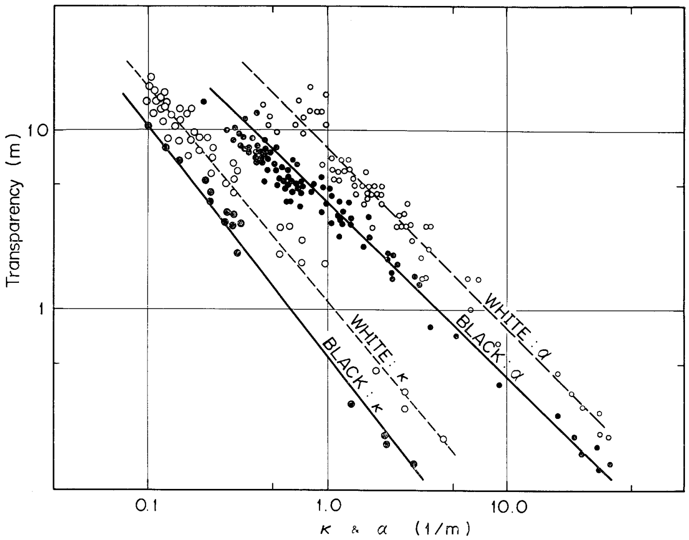

Fig. 2. Relationship between transparency and beam-extinction coefficient, and diffused-light extinction coefficient.

$$(\alpha+K)T=\ln\frac{A/\pi}{\sigma\beta/(\alpha+K)} \qquad (9)$$

となる。

いま，(9) 式において，透明度板の反射係数 A の値，または，識閾の値が2倍または半分に変化したと仮定すると，$(\alpha+K)T$ の値は約0.69増加または減少する。$(\alpha+K)T$ の値は，多くの観測の結果約9.5であるから (Fig. 2)，その変化率は10％以下である。すなわち，透明度の測定は，透明度板の反射率が多少変化しても，あるいは観測者によって識閾が多少変化しても，透明度の測定値に与える変動は非常に小さい。このことから透明度の測定は普遍性のある測定法と言える。

2.2　黒色円板による透明度

透明度板が白色でなければならない事はない。透明度の波長による変化の研究は TAKENOUCHI (1950)[5] によって色々と行われた。ここで思い切って黒色（反射率≒0の板）透明度板を使用した場合の検討を行う。

黒い透明度板上からの光の方が周辺からの光よりも弱いので，(4) 式を

$$\frac{F_1-(F_T+F_2)}{F_1}\leq\sigma \qquad (10)$$

と書くことができる。この式を白色板と同様に書き直し，透明度板の反射率をゼロ($A=0$)とすれば，

$$(\alpha+K)T_B=\ln\frac{1}{\sigma} \qquad (11)$$

となる。すなわち，黒色板透明度と $(\alpha+K)$ の積は，識閾だけの函数になる。識閾は定数と考えられている (MIDDLETON 1935)[6]。

黒い透明度板を用いて透明度を測定すると，その理論式が非常に簡単になり，透明度の深さは$(\alpha+K)$に逆比例するという関係になる。黒の透明度は白の透明度の50～70％であるので，より浅い層の海水の状態しか情報は得られないが，測定した透明度の値から直ちに $(\alpha+K)$ を推定できるという利点がある。透明度測定の時，黒い透明度板を用いた透明度測定をもっと普及させるべきであると考える。

2.3　観測データとの比較

Fig. 2 は色々な海域で観測された透明度と消散係数(α および K)の関係を示したものである。白い透明度板を用いて測定した透明度 (T) と光束消散係数 (α) との関係を示したものが一番上部に，黒い透明度板で測定した透明度(T_B)と光束消散係数 (α) との関係が2番目に，白色板の透明度 (T)

と分散光の消散係数 (K) との関係が3番目に，黒色板の透明度 (T_B) と分散光の消散係数 (K) との関係が一番下に示されている。

調査海域は東海村沖，琵琶湖，紀伊浦神湾，ベーリング海である (福田 1957)[7]。透明度の極端に小さな所は，水槽の内部に鏡を張り付けて濁った所の測定を行った。

これらの測定結果から，消散係数と透明度との関係を近似的に求めた。白色透明度板と光束消散係数の場合，

$$\alpha \cdot T_W = 8.0 \qquad (12)$$

黒色透明度板と光束消散係数の場合，

$$\alpha \cdot T_B = 3.5 \qquad (13)$$

白色透明度板と分散光消散係数の場合，

$$K \cdot T_W = 1.5 \qquad (14)$$

黒色透明度板と分散光消散係数の場合，

$$K \cdot T_B = 0.4 \qquad (15)$$

である。

(11), (13), (15) 式を用いると，

$$\ln(1/\sigma) = (\alpha + K) \cdot T_B = 3.9 \qquad (16)$$

であるから，$\sigma = 0.02$ となる。この値は気象で測定され，よく視程の問題に用いられる識閾の値 0.02〜0.05 (正木 1968)[8] によく一致している。海の中の視程の問題にも，気象など空中で用いる識閾の値を用いてもよいことがわかった。

2.4　後方散乱係数の推定

光散乱を測定するのは簡単ではない。精密な測定器を必要とする。透明度の理論において，極めてラフではあるが後方散乱の概念を導入してあるので，その係数の値を求めてみた。後方散乱係数は，Fig. 7 に見られるように，前方散乱に比べ角度による値の変化が小さい。さらに，上方から下方に向う光も必ずしも太陽からの平行光ばかりとは限らないので，後方散乱係数は平均的な値を考えることとする。

(11) 式から $\sigma = \exp\{-(\alpha + K) \cdot T_B\}$ であるので，(7) 式を次のように書き変えることができる。

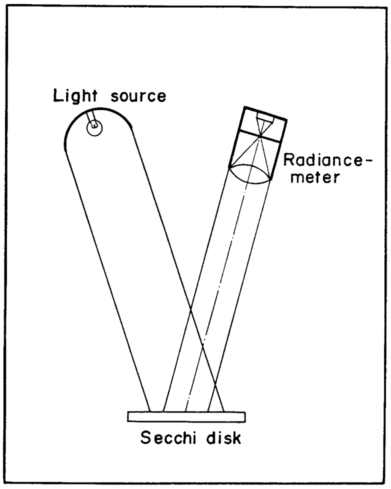

Fig 3.　Method of reflection-factor measurement.

$$\frac{\beta}{(\alpha+K)} = \frac{\dfrac{A}{\pi}\exp\{-(\alpha+K)T_W\}}{\exp\{-(\alpha+K)T_W\}+\exp\{-(\alpha+K)T_B\}} \qquad (16)$$

ここで，T_W は白色板を用いた透明度，T_B は黒色板を用いた透明度である。

白色透明度板の反射係数 A は，Fig. 3 に示すような方法で測定した。透明度板に直角方向から 60° 位までの入射角，反射角の範囲では反射係数はほぼ一定の値をとる。A の値として約 $8.0 \cdot 10^{-3}$ str^{-1} を得た。

$(\alpha+K)T_W$ および $(\alpha+K)T_B$ の値を定数とし，それぞれ Fig. 2 から 9.5, 3.9 とする。これから，$\beta/(\alpha+K)$ は $9.5 \cdot 10^{-6}$ str^{-1} となる。

2.5　海面反射が透明度に与える影響

普通，透明度を測定するには船上から海中をのぞき込むのであるから，海面に空中から投射した光の一部は反射され目に入る。Fig. 1 のモデルにおいて，F_1, F_T にそれぞれ F_R (海表面からの反射光) を加えたものになる。

すなわち，

$$\gamma = \frac{F_T + F_2 - F_1}{F_1 + F_R} \leq \sigma \qquad (17)$$

である。前と同様の計算を行うと，

$$(\alpha+K)T_W=\ln\frac{\dfrac{A}{\pi}-\dfrac{\beta}{(\alpha+K)}}{\sigma\left(\dfrac{\beta}{\alpha+K}+\dfrac{E_{SK}}{I_0}R\right)} \tag{18}$$

となる。ここで，E_{SK}/I_0 は天空の輝度と太陽からの入射光（海面下における）の照度との比，R は海面での天空光の反射率である。海中から空中へ出る時の反射は透明度に与える影響が小さいと考え省略する。

R はスムーズな海面を考えると近似的に0.02として良い。E_{SK}/I_0 は，測定すると約 0.008 str^{-1} である。$A=8.0\cdot10^{-3}\,str^{-1}$，$\beta/(\alpha+K)=9.5\cdot10^{-6}\,str^{-1}$，$\sigma=0.02$ とすれば，海面反射が無い場合の $(\alpha+K)T_W$ の値は 9.5 となるが，海面反射を眼に入れた場合は 6.6 となる。

黒色透明度板を用いた時の天空光の海面反射の影響も同様に計算できる。(10) 式に海面反射の天空光を入れると，

$$\frac{F_1(F_T+F_2)}{F_1+F_R}\leq\sigma \tag{19}$$

となる。左辺と右辺が等しいとして書き直すと，

$$(\alpha+K)T_B=\ln\frac{\dfrac{\beta}{(\alpha+K)}}{\sigma\left(\dfrac{\beta}{\alpha+K}+\dfrac{E_{SK}}{I_0}R\right)} \tag{20}$$

となる。白色透明度板で計算したと同じ条件で (20) 式を計算すると，海面反射が無い場合の $(\alpha+K)T_B$ の値は 3.9 であるが，反射光を入れると約 1.0 となる。

透明度を測定する時，眼に海面から反射した天空光を入れて測定した場合，天空光を入れない場合（海面からのぞき箱で透明度板を見る場合）の白板では約 30％（8 m の透明度のとき），黒板では約 74％（4 m の透明度のとき）透明度が減少することが計算から推定される。

1977年12月，紀伊浦神湾の観測において，白色透明度の測定を空中からとのぞき窓を用いたものとで行った。その結果を Table 1 に示す。空中からの観測には眼に天空光が入っている。この結果，空中からのはのぞき窓の値より 10～20％ 減少した値を得た。この値は，計算値より小さいが，表面の状況によりこの位の値になる可能性はある。

Table 1. Comparison of transparency measured with and without the peep box.

	Transparency (white) in m				
Without peep box	16.5	11.2	8.2	4.5	2.3
With peep box	20.0	14.0	9.0	5.2	3.0

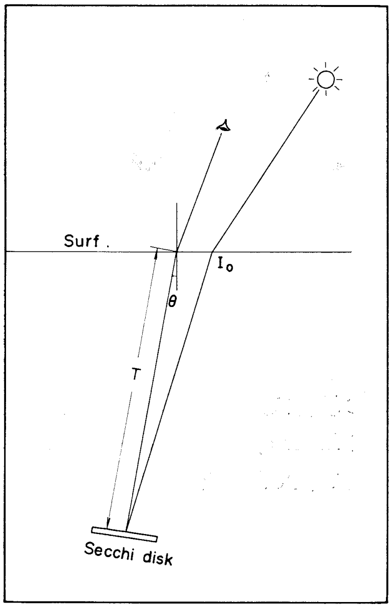

Fig. 4. Transparency measurement in case of inclined rope from vertical.

2.5 ロープに傾斜がある場合の透明度

海で透明度を測定する時，よく出逢う問題に，風などのため船が流され，透明度板からのロープが鉛直方向から角度を持つことがある。図で示すと，Fig. 4 のような場合である。このモデルでも (4) 式を適用することができる。

$$F_1=\frac{\pi}{4}I_0\beta\left(\frac{\phi}{f}\right)^2\int_0^\infty \exp\{-(\alpha+K\cos\theta)z\}dz$$
$$=\frac{\pi}{4}\frac{I_0\beta}{(\alpha+K\cos\theta)}\left(\frac{\phi}{f}\right)^2 \tag{21}$$

$$F_2=\frac{\pi}{4}\frac{I_0\beta\left(\dfrac{\phi}{f}\right)^2}{(\alpha+K\cos\theta)}$$
$$\times[1-\exp\{-(\alpha+K\cos\theta)T\}] \tag{22}$$

$$F_T=\frac{A}{4}I_0\left(\frac{\phi}{f}\right)^2\exp\{-(\alpha+K)T\} \qquad (23)$$

であるから，(8) 式に相当するものが次のように書ける。

$$(\alpha+K\cos\theta)T=\ln\left(\frac{\dfrac{A}{\pi}-\dfrac{\beta}{\alpha+K\cos\theta}}{\dfrac{\sigma\beta}{\alpha+K\cos\theta}}\right) \qquad (24)$$

同様に，(11) に相当するものとして，

$$(\alpha+K\cos\theta)T_B=\ln\frac{1}{\sigma} \qquad (25)$$

を得る。K は α の約 10～20％ であるから，60° ロープが傾斜したとしても，$(\alpha+K\cos\theta)\cdot T_B$ の $(\alpha+K)T_B$ からの違いはせいぜい 5～10％ 位である。

白色板の場合は，黒色板の場合より複雑であるが，$\beta/(\alpha+K\cos\theta)$ の値はほぼ一定で A に比べはるかに小さい値であると考えられるから，

$$(\alpha+K\cos\theta)T_W=\ln\frac{A/\pi}{\sigma\beta/(\sigma+K\cos\theta)} \qquad (26)$$

と書ける。黒色板と同様に K は α に比べ小さいので，ロープの傾斜が多少あっても鉛直下に下ろした時とあまり変わりないと考えられる。

透明度を測定する時は，ロープに傾斜があっても透明度としてロープのくり出した長さをとるのが正しいと考えることができる。

ロープに傾斜がある時，透明度にはここで考えられた以外の要素が影響すると思われる。例えば，傾斜する場合は必ず強い風があるために海面に波がある。波は海表面付近に泡などを作る。海面に斜めにロープが入っているので視野に天空光の海面反射が入る。透明度板が水平でなく傾いている。などの事がらが透明度に影響を与えるはずである。しかし，これらの事がらを一緒にして解析を行うのは今の所困難である。

3. 透明度板の大きさ

透明度板は 1.2 で述べたように白色ペンキぬりの 30 cm の円板であるが，この大きさを変えた場合透明度の値に影響を与えるかどうかを海で観測した。透明度が異なった場合，目に見える透明度板の大きさは違ってくるのでその影響がどのようにあるかを調べることにも関連している。

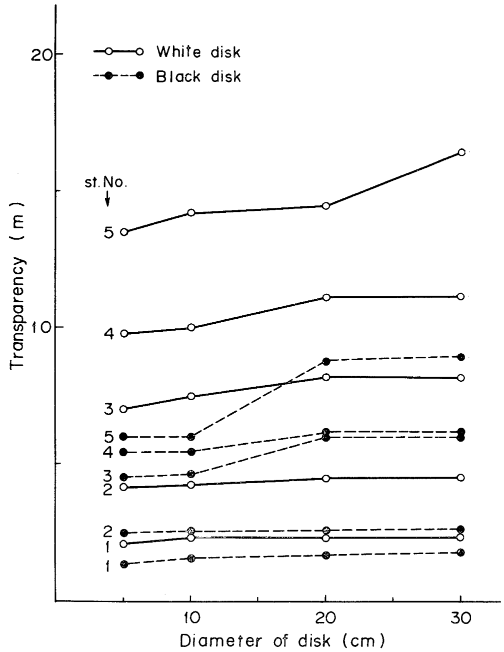

Fig. 5. Variation of transparency with size of Secchi disks.

実験は紀伊浦神湾において 1977 年 12 月と 1978 年 5 月の 2 回にわたって行われた。

透明度板は白と黒のプラスチックの円板で，5, 10, 20, 30 cm の 4 種類を作った。この円板に普通の透明度板のような形にロープと重りを付けて測定を行った。

測定は透明度板の見える場所が船のかげに入るようにして行った。測定の結果を Fig. 5 に示す。横軸に円板の大きさ，縦軸に透明度の値をとってある。黒の透明度は白の透明度の 50～70％ の値をとる。

Fig. 5 を見ると，円板の大きさが大きくなるに従って若干透明度が増大しているが，それほど大きなものではない。ほとんどが 10％ 以下である。一番透明度の大きい所で，5 cm から 30 cm の透明度板で 18～25％ 増大している。この場合，透明度板の直径が 6 倍変化したのであるから，普通

の (30 cm) 透明度板を用いた場合，16 m の深さの透明度板と 96 m の深さの透明度板の大きさに相当する。

このように考えると透明度が深くなったために透明度板が小さく見え，それによって透明度の値に影響を与えるという事は考慮する必要がないものと考えられる。この結論は HOLMES (1970)[9] の観測結果と一致する。

4. 透明度板のボケの問題

透明度が見えなくなるのは，(4) 式で示される識閾がある値以下になった時起ると考えられるが，スリ硝子などを通して物を見た時に生ずると同様のボケが透明度測定においても影響を与えるのではないかと考え検討を試みた。

4.1 透明度板のボケの計算

Fig. 6 に示すモデルに従って F 面上に透明度板の像がどのように写るかを計算する。

F は目の網膜又はカメラのフィルムに相当するものであり，透明度板の像はここに結ぶ。L は眼球またはカメラのレンズである。SF は海面で，この計算では簡単のため海面で反射した天空からの光は L に入らないものとする。

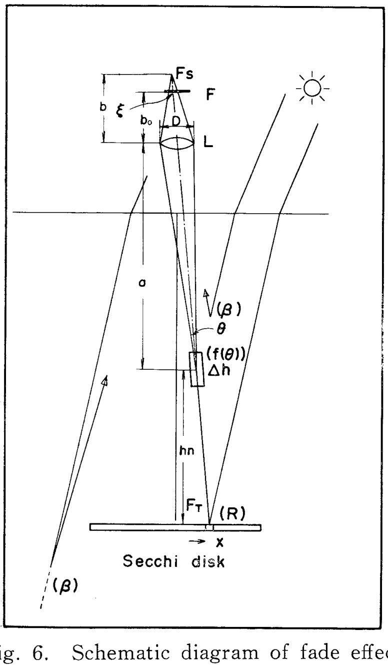

Fig. 6. Schematic diagram of fade effect calculation.

海面は滑らかな平面とする。S の透明度板から反射された光は海面に到達するまでに消散されて行くが，消散されたもののいくらかは海水中の物質により散乱されて L の中に入る。L に入った光は散乱された深さによって F よりも後の方に像を結ぶので，F の上には広がりをもった(ボケた)像が写る。S の深さは Z とし，この深さは任意に(透明度より浅く) 取る。

いま，海面から I_0 の入射光があるとする。透明度板上の照度は (1) 式で，透明度板の輝度は (2) 式で計算される。透明度板微小部分 dx から上に向う光が，透明度板から h_n の高さにある所と $h_n+\varDelta h$ の高さの間で消散する光は，

$$\varDelta E_{S_n}=\frac{E_T}{h_n{}^2\pi}\times[\exp(-\alpha h_n)-\exp\{-\alpha(h_n+\varDelta h)\}] \quad (27)$$

である。この光の大部分 (70～95％) が散乱され，残りの小部分が吸収されるものと考えられる。

光の散乱角度分布は色々な人達 (KULLENBERG 1968[10]，SASAKI 1968[11]) によって報告されているが，測定海域によっても違い，定まったものではない。ここで考えたのは，前方散乱の強い場合

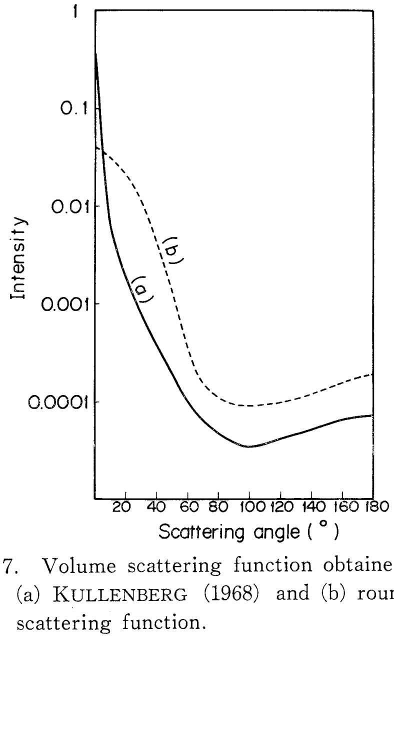

Fig. 7. Volume scattering function obtained by (a) KULLENBERG (1968) and (b) roundish scattering function.

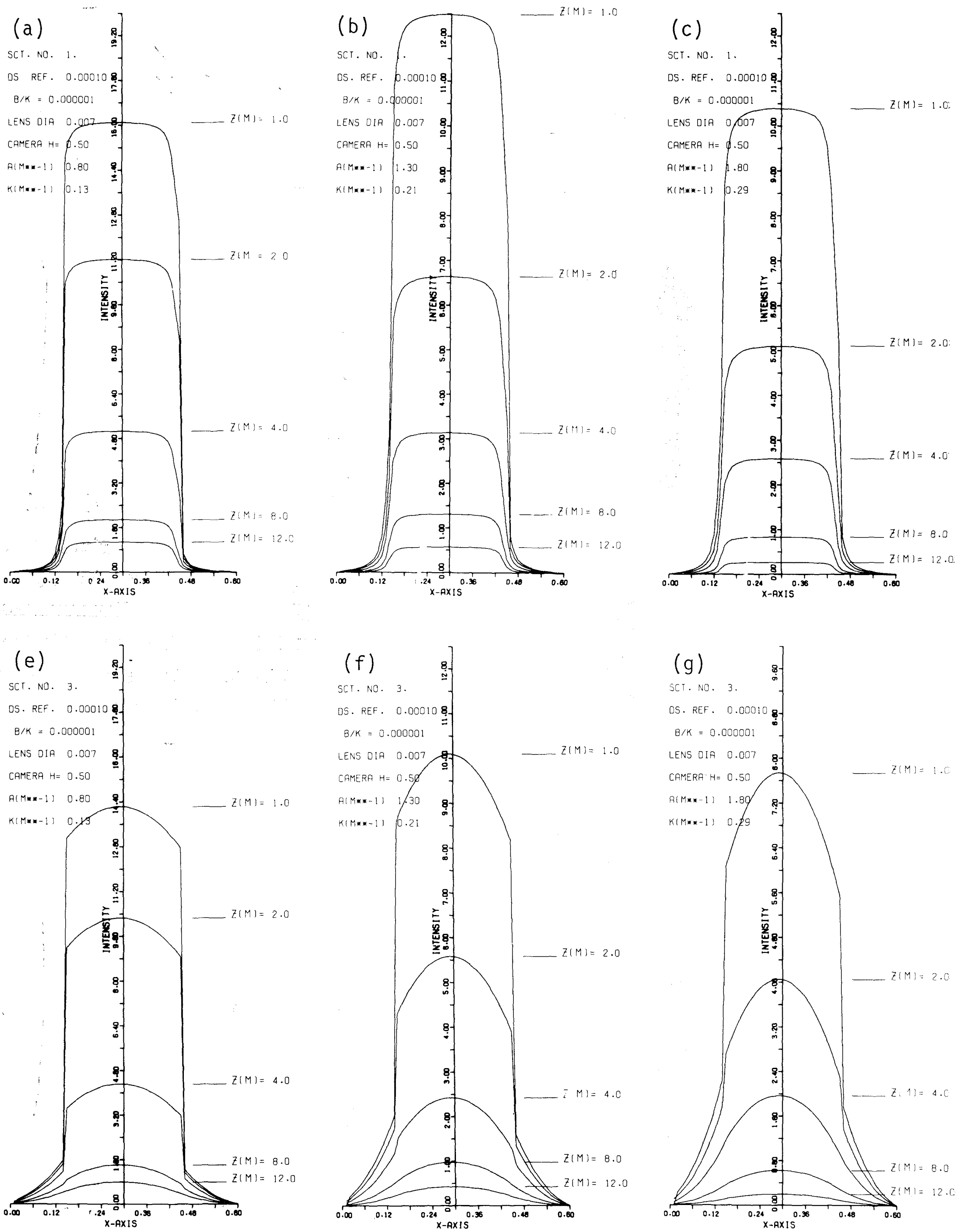

Fig. 8. Calculated light intensity of the Secchi disk faded by the scattering.

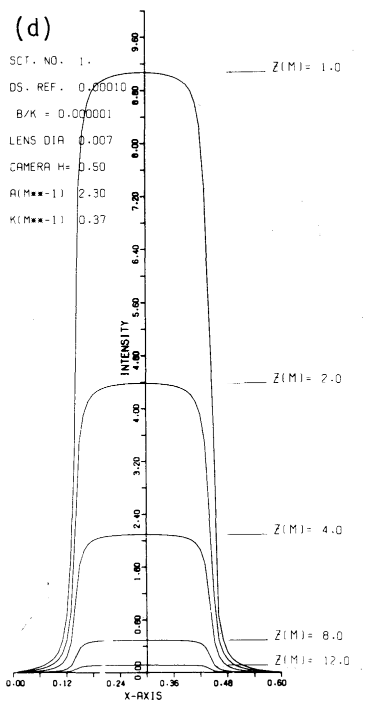

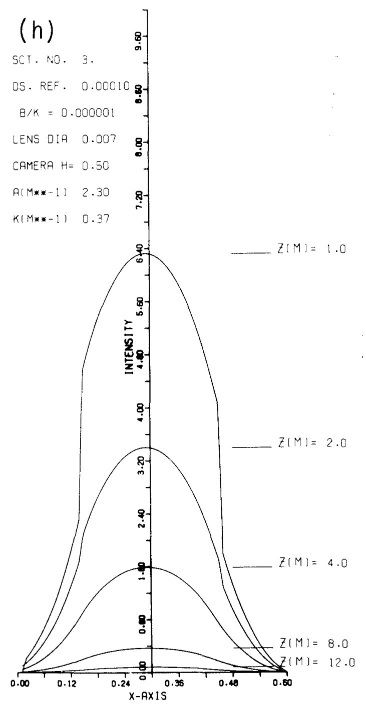

(a) Kullenberg's scattering function, $\alpha=0.8\ m^{-1}$ $K=0.13\ m^{-1}$, $\beta/k=10^{-6}$, $R=10^{-4}$

(b) Kullenberg's scattering function, $\alpha=1.3\ m^{-1}$ $K=0.21\ m^{-1}$, $\beta/k=10^{-6}$, $R=10^{-4}$

(c) Kullenberg's scattering function, $\alpha=1.8\ m^{-1}$ $K=0.29\ m^{-1}$, $\beta/k=10^{-6}$, $R=10^{-4}$

(d) Kullenberg's scattering function, $\alpha=2.3\ m^{-1}$ $K=0.37\ m^{-1}$, $\beta/k=10^{-6}$, $R=10^{-4}$

(e) roundish scattering function, $\alpha=0.8\ m^{-1}$ $K=0.13\ m^{-1}$, $\beta/b=10^{-6}$, $R=10^{-4}$

(f) roundish scattering function, $\alpha=1.3\ m^{-1}$ $K=0.21\ m^{-1}$, $\beta/k=10^{-6}$, $R=10^{-4}$

(g) roundish scattering function, $\alpha=1.8\ m^{-1}$ $K=0.29\ m^{-1}$, $\beta/k=10^{-6}$, $R=10^{-4}$

(h) roundish scattering function, $\alpha=2.3\ m^{-1}$ $K=0.37\ m^{-1}$, $\beta/k=10^{-6}$, $R=10^{-4}$

（Fig. 7 の a 線と，丸い形に近い散乱分布を示す場合（Fig. 7 の b 線）とである。その強さはいずれも懸濁物の濃度に比例するものと考えられる。

散乱した光が L のレンズを通し F に受光される割合は非常に少さい。この割合は θ に関係する。

$$\theta=\tan^{-1}(D/a) \qquad (28)$$

である。ここで a は散乱した所から L までの距離である。

L で受光される光の割合は，散乱光の角度分布を θ まで積分したものに比例する。すなわち，

$$\Delta E_S=\Delta E_{Sn}Z\int_0^{\theta}f(\theta)d\theta \qquad (29)$$

である。ここで，$f(\theta)$ は光角度散乱係数で，$\int_0^{2\pi}f(\theta)d\theta=1$ とする。

このような散乱光が一つの光軸について，深さ Z から海面まであるので積分する必要がある。すなわち，

$$F_S(x)=\int_0^Z \Delta E_S dz=\int_0^Z \Delta E_{Sn}\int_0^{\theta}f(\theta)d\theta dz \qquad (30)$$

と表わされる。ここで $F_S(x)$ は透明度板の微小部分 dx から放出された光によるものである。

光角 θ 内に散乱された光は，レンズ L によって L から b なる距離の所（F 上）に像を結ぶ。F 上では幅 ξ の中に投影される。正しくはこの ξ 中での光の分布は一様ではないが，近似的にこの幅内に一様な強さで分布すると仮定する。そうすると，散乱光が F 上に与える単位長の照度は，

$$dF_{f1}(x)=F_S(x)/\xi \qquad (31)$$

となる。海面の屈折を省略すれば，

$$b_0=(Z+h)\cdot F_c/(Z+h-F_c) \qquad (32)$$

$$b=a\cdot F_c/(a-F_c) \qquad (33)$$

$$\xi=D\cdot(b-b_0)/b \qquad (34)$$

である。ここで，h は海面からのレンズ L の高さ，F_c はレンズの焦点距離，D はレンズの直径，a はレンズから散乱物までの距離である。

この $dF_{f1}(x)$ は透明度板上の各点から来る光なので，F 上の光の分布を求めるには透明度板全体について積算する必要がある。積分の式は，

$$F_f=\int_{-X_0/2}^{X_0/2}dF_{f1}(x) \qquad (35)$$

となる。

透明度板からレンズ L を通して F に像を結ぶ光（散乱を受けずに直接レンズに到着する光）は，(3) 式で計算される。

このほか，F 面に投射される光は，(5) 式で表わされるバックグラウンドの光と，(6) 式で表わされる透明度板と海面の間の水により散乱される光とがある。

さらに，バックグラウンドの光のうち透明度板より深い所から来る光は，(27)～(35) 式で計算されると同様の散乱を受けるので，それを加算しなければならないが，計算して見ると，小さい値なので省略してもさしつかえない。

バックグラウンドから来る光（E_B），透明度板と海面の間の海水で散乱された光（E_{up}），透明度板から直接レンズに到着する光（F_T），透明度板からの光が海中で散乱されてからレンズに到着した光（F_f），を各方向においてそれぞれ加算し，フィルム上の透明度板の像の光の強さが計算される。

この方法を用い，計算機により透明度板のフィルム上の光の強さを計算した例を挙げる。

透明度板の反射係数を $8\cdot10^{-3}$ str^{-1}，レンズの直径を 1.4 cm，レンズの焦点距離を 5 cm，レンズの水面からの高さを 0.5 m，$\beta/(\alpha+K)$ を $9.5\cdot10^{-6}$ str^{-1} とし，Kullenberg の光角度散乱係数（Fig. 7のa 線）と，丸味の形の散乱係数(Fig. 7のb 線)の 2 つの例について，それぞれ，光束消散係数を 0.8, 1.3, 1.8, 2.3 m^{-1} とし，透明度板を 1, 2, 4, 8, 12 m の深さに置いて写真を撮った時のフィルム面上の光の強さを計算し，Fig. 8 (a)～(h) に示した。横軸は透明度板の位置にもどしたスケールに換算してあるので，透明度板の深さに関係なく横軸の長さが比較できる。縦軸はフィルム面の光の強さを比較しやすいように，一番右端の値（最少値）を全部の値から引き去り，見やすくしてある。実際には，深い所の測定値の方が一般に高

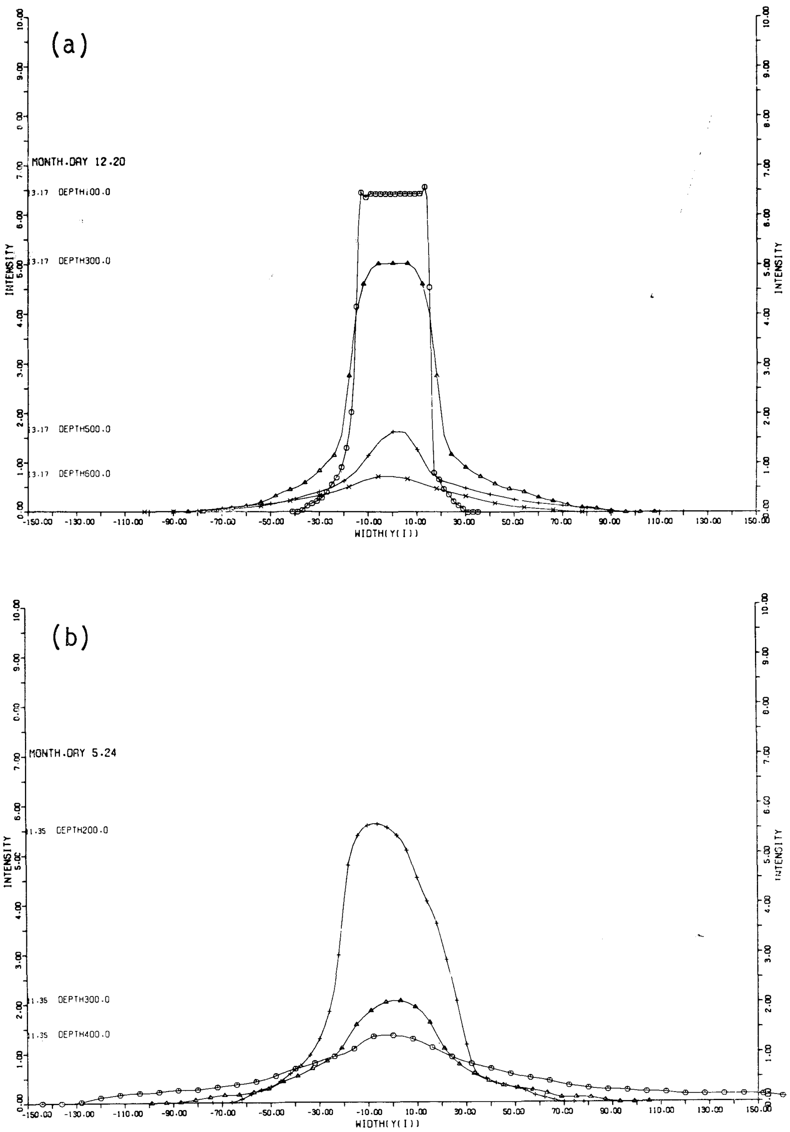

Fig. 9. Measured light intensity of the Secchi disk faded by the scattering, at the Kii-Uragami Bay on (a) Dec. 20, 1977 and (b) May 24, 1978. Depth and width in cm.

い値を示す。

4.2 議　論

紀伊浦神湾の観測において透明度板を水中カメラで海面から撮影し，そのフィルム上の感光濃度を測定した。その結果を Fig. 9 (a) と (b) に示す。

計算結果では，同じ消散係数のうち深さを変化させると分布の形をあまり変えず強さだけが変化している。しかし，観測結果では，深くなるにつれて分布の形が丸味を帯びてくる。この原因として考えられるのは，この計算では，深さや消散係数が大きくなっても散乱係数が同じであるとして行ったが，実際の海では多重光散乱があるため，散乱角度分布が次第に丸味のある分布になってくることである。

光の濃度分布は，計算結果と観測結果が比較的によく合う。このことは，この様なモデルを用い

ることと，この計算に用いたパラメータの値がよく現象を表わしていると考えられる。

Fig. 8 (a)～(d) と Fig. 8 (e)～(h) の間には，光の分布が角形と丸味をもったものとの違いがある。前者はシャープな形の Kullenberg 散乱で，後者は丸味をもった散乱の時の分布である。すなわち，同じ消散係数であっても，光散乱の分布が丸味をもつほど (粒度の小さい懸濁物ほど) 写真の像の辺の形が丸味を帯びて (ボケて) くる。

この計算結果から，(4) 式の γ (コントラスト) を求めて図に示すと Fig. 10, Fig. 11 のようになる。ただし，この中には天空からの光の海面での反射も含まれている。Fig. 10 は Kullenberg 散乱，Fig. 11 は丸味の散乱のケースである。γ が 0.02 の所を見ると，α の値 0.8 m^{-1} で α と深さ T_W の積は 8.5 となり，α の値 2.3 m^{-1} では 12.0 となる。これらの値はかなりちらばっているが，測定結果 (Fig. 2) では，α と T_W の積は 5.0 から 20.0 の間にちらばっている。両者の間にはよい一致が見られる。

これらの結果は，前に述べた透明度板の理論的解析ともよく一致している。

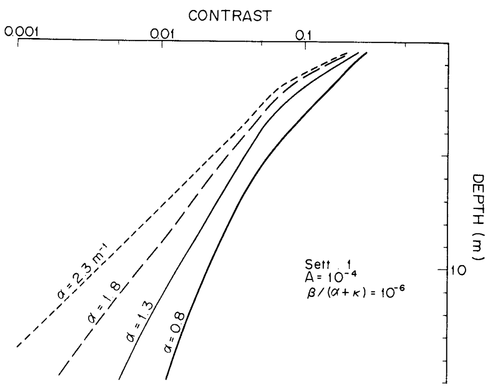

Fig. 10. Variation of calculated contrast value of Secchi disk (Kullenberg's scattering function).

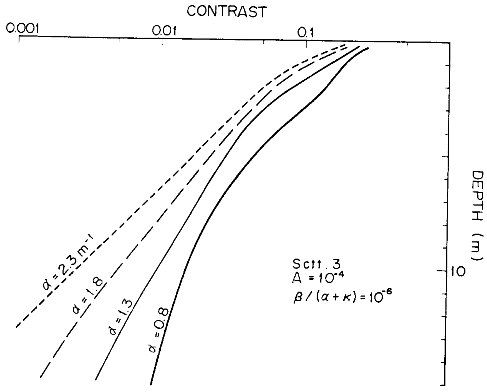

Fig. 11. Variation of calculated contrast value of Secchi disk (roundish scattering function).

5. まとめ

海洋観測に広く用いられている透明度の測定を理論的に解析し，その実用性と問題点に関し議論を行った。

上空から海中に光が投射され，透明度板で反射され，海中で吸収・散乱されながら眼に到着する光と，海水中で散乱されて眼に到着する光の組合せのうち，透明度板上の方向から来る全部の光と周辺からくる光の差を周辺からくる光の値で割った値 (コントラスト) が人間の識閾 (threshold) より小さくなった時に透明度板が見えなくなると考えられている。この定義に基いて，下に進む光は分散光消散係数を，上向きの光は光束消散係数で減衰するとし，海水中で後向きの消散係数と両消散係数の和との比を一定と仮定して式を作った。これから，もしも透明度板が黒で反射率 0 の場合には，黒い透明度板の観測結果から識閾を計算することができ，データからその値は 0.02 となった。これは気象で測定された値とよく一致する。

白い透明度板の式において透明度と消散係数との関係及び板の反射係数を与えてやると，海中の後方散乱係数を計算することができる。白色透明度板の反射係数は測定によると $8.0\cdot10^{-3}$ であったので，後方散乱係数は $9.5\cdot10^{-6}$ を得た。

透明度測定は船上から海中をのぞくので，どうしても海面で反射した天空光が目に入りやすい。船のかげ又はのぞき眼鏡で海中を見た場合と反射した天空光を目に入れた場合とで，どの位透明度の値に違いがでるかを計算して見た。白色透明度板で 8 m の透明度の海では約 30% 天空光を目に入れた方が減少し，黒色透明度ではその値が 74% 減少する。実際の海での測定では，白色透明度板

で10～20％減少した値を得た。

海洋観測において透明度を測定するのに，透明度板が流れてロープに傾斜がつく事がしばしばある。この様な場合の透明度に及ぼす影響を推定した。黒色透明度板の場合，ロープが60°傾斜したとしても，ロープのくり出した長さを透明度として鉛直になった時のせいぜい5～10％位しかその値は減少しない。白色透明度板の場合は，その値にほとんど変化はない。すなわち，ロープのくり出した長さを透明度とすれば良いことになる。しかし，ロープが傾く時は海面の状況がおだやかでないので，その他の原因による誤差が生ずる事を考慮する必要がある。

透明度が大きくなると透明度板が小さく見え，そのために透明度の値に影響を与えるかも知れないという問題を解明するために，直径 5,10,20,30 cm の円板の透明度板で測定を行った。円板の直径が小さくなると若干（10％位まで）透明度が減少する傾向があるが，問題にしなくてもよいものと考えられるような結果を得た。

透明度板が見えなくなるのはコントラストの問題として扱って来たが，我々が日常経験することで，光が散乱されたりするため物体の姿が端からぼけ，次第に判別付かなくなる現象もある。この現象に数値解析を行った。光消散係数，光散乱係数，透明度板の反射率，後方散乱係数，レンズの大きさ，透明度板の深さ等をパラメータとして計算を行った。2.3，2.4，2.5 の各項で求められたパラメータの値を用いた計算結果が，透明度板を写真に撮ってその光の分布を測定した結果とよく合った。しかし，測定した結果においては透明度板の端の光の分布が海水が濁ったり深くなるに従いかなり早く丸味を帯びた形（ボケて来る）になりやすいが，計算上では中々そうなりにくい。この原因としては，光の散乱角度分布が濁るに従い多重散乱のため丸味を帯びた分布になってくるからと推定される。

この計算手法を用いても，コントラスト 0.02 付近の値が，透明度の深さと一致し，前の理論計算結果とよく合う。

以上の事がらを総合して，透明度は簡単に誰でも測ることができ，古くからデータを得られている重要なパラメータである。その値は普遍性があり，いつ何処で誰が測っても比較し得る。さらに，黒い透明度板を用いることにより，その海水の光学的性質の一部を解析することができるようになる。透明度は海水の汚れの大きい沿岸において良い指標になると考えられる。しかし，透明度板は透明度の深さまでの海水の平均的光学的性質を表わしているものであるから，それ以上のもの（例えば層状になっている濁りの分布等）は議論することはできない。沿岸海洋において環境汚染等の調査を行う機会が増えると考えられるが，透明度は有効なパラメータであるので大いに観測することをすすめる。そして，そのデータをさらに物理・化学・生物学的に解析を進めることにより，海洋環境の解明に役立つものと信ずる。

謝　辞

この論文を書くに当って御助言をいただいた東海大学教授竹内能忠博士，芝浦大学教授井上直一博士に心からの感謝の意を表する。海洋観測に助力をいただいた近畿大学の学生諸君，原研において観測を手伝っていただいた原研原子炉計測研究室山田政治，放管第1課小畑一一の両氏に謝意を表する。この研究を進めるに当って御助言をいただいた理化学研究所岡見登，岸野元彰両氏に謝意を表する。

文　献

1) 竹内能忠（1952）：海中照明及びそれに関連する諸現象に関する研究．研究時報，**4**，268-321.
2) NANNITI, T. (1954): A theory on the transparency of sea water. Papers Meteorol. Geophys., **3**, 195-201.
3) TYLER, J.E. (1968): The Secchi disc. Limnol. Oceanogr., **13**, 1-6.
4) 気象庁（編）（1970）：海洋観測指針．日本海洋学会．427 pp.
5) TAKENOUCHI, Y. (1950): On the transparency of sea water. Oceanogr. Mag., **2**, 129-135.
6) MIDDLETON, W.E.K., (1935): Visibility in Meteorology. Univ. Toronto Press. 69 pp.
7) 福田雅明，勝木　茂（1957）：海洋調査漁業試験要報（北大水産学部）第1号，p. 188-190.

8) 正木　光（1968）：気象光学．光学技術ハンドブック（久保田広ほか編），朝倉書店，p. 1109-1123.
9) HOLMES, R. W., (1970): The Secchi disk in turbid coastal waters. Limnol. Oceanogr., **15**, 688-694.
10) KULLENBERG, G. (1968): Scattering of light by Sargasso Sea water. Deep-Sea Res., **15**, 423-432.
11) SASAKI, T., N. OKAMI and S. MATSUMURA (1968): Scattering function for deep sea water of the Kuroshio. La mer, **6**, 165-176.

La mer (Bulletin de la Société franco-japonaise d'océanographie)
Tome 18, N° 3, pp. 153 à 155, Août 1980

日仏海洋学会賞受賞記念講演

海洋光学に関する一連の研究*

岡　見　　　登**

Une Série des Recherches sur l'Optique Océanographique*

Noboru OKAMI**

この度，私は日仏海洋学会賞を受賞させて頂き，非常に光栄に存じ心から感謝致しております。受賞の対象となった『海洋光学に関する一連の研究』は私一人で行なった研究ではなく，本学会の会長の佐々木忠義先生を中心として，先生の御指導のもとに大柴五八郎，渡辺精一両先輩と協力して行なった20数年に亘る研究と佐々木先生と大柴，渡辺両先輩が理化学研究所を去られた後，今日なお良き協同研究者として海洋光学の研究をともに続けている岸野元彰，竹松伸，杉原滋彦諸兄と協力して行なった研究であります。したがって，本日の栄誉は私が代表して頂いたのだときもにめいじ，佐々木先生はじめ協力していただいた諸兄に心から感謝致して居る次第でございます。また，佐々木先生が理研を去られた後，私達の研究室の主任となられた宇野木早苗先生に深く感謝の意を表したいと思います。先生は私達の海洋光学の研究に良き理解をしめされ，適切な御助言と暖かい御激励を頂きました。心から御礼を申し上げます。では，私の海洋光学に関する一連の研究はどのような道をたどってきたかを述べさせて頂きます。

私の海洋光学への研究は昭和24年水中光源の海中の配光曲線の測定から始まりました。この時使用した測器は，私が入所する前に佐々木先生達が研究製作した光電管を用いた水中輝度計でした。輝度と照度の違いを完全に理解できたのは，その後水中分光放射照度計を研究室で製作したときです。受光器には光電子増倍管を用い，受光部の最上部には余弦集光器としてオパールガラスを取付けました。受光部の角特性の測定を行ない，かなり良い結果を得たときはじめて，照度計の具備しなければならない必要条件と輝度計と照度計の違いを理解することが出来ました。オパールガラスと使用した5枚の色フィルターの分光透過率は，当時初台にあった工業試験所で，我が国に初めて輸入されたG.E.の自記分光光度計で測定してもらいました。すばらしい装置があるものだと驚いたことも今はなつかしい思い出の一つとなっております。完成した水中分光放射照度計を用いて昭和28年から芦の湖や黒潮流域で各層の分光エネルギー分布の測定を行ないました。そして，測定結果を考察することによって海の濁りの問題，海洋生物の光環境の問題などその後の研究へと発展しました。昭和27年から30年にわたって私達の研究室は"潜水探測機くろしお号"による漁場調査の研究に参加致しました。この研究で私は海中の明るさの変化や海中の光の色を自からの目で観察する機会を得ました。相模湾の海中で見たあざやかなコバルトブールの水の色，このときマリンスノーと名付けられた大型の海中懸濁物など水中で観察した色々な現象は今でも忘れることができません。そして，この時の海中での観察が次の

---

* 1980年5月30日，日仏会館(東京)にて講演
Résumé de la conférence faite le 30 Mai 1980 aprés la remise du Prix de la Sociéte franco-japonaise d'océanographie

** 理化学研究所　Institut de Recherche Physique et Chimique

研究の手がかりとなったのです。私達はこの“くろしお号”を使って海中輝度の角度分布の測定を噴火湾と陸奥湾で行ないました。そして，この測定は，その後船上からの遠隔操作によって任意の深さの輝度分布を測定することのできる測器の開発研究へと発展しました。この測器を用いた測定結果は，近年実施している海の色のリモートセンシングの研究にも今なお役立っております。また，輝度分布の理論計算を行ない，実測値と比較して検討しました。このとき，Schuster の二流モデルを適用して導いた海中放射の伝達方程式は，近年の海の色のスペクトルの理論計算にも適用して居ます。

輝度分布の理論計算の段階で海水による散乱光の角度分布の値が必要になりました。そこで，この値を測定するために散乱光度計を自作しました。完成した装置を用いて測定した最初の試水は，佐々木先生がフランス海軍のバチスカーフに搭乗して日本海溝に潜水された際に，3000 m の深海から採取したものでした。佐々木先生から与えられたテーマは深海水の濁りの測定でした。私はこの研究では懸濁粒子の光散乱に Mie の散乱理論を適用して計算した散乱光の角度分布と実測した角度分布を比較することによって，懸濁物の粒径と屈折率を推定しました。山口成人先生，，小川智哉氏にお願いして，電子回折やX線回折によって懸濁物の種類の同定を行なうなど，光散乱の研究は当初考えてもいなかった方向に発展しましたが，ここで得た研究成果は海の濁りの概念を把握するのに大変役立ちました。

昭和38年岸野君が入所して以来二人で始めた研究は種々の海域の海水の光学的性質の測定です。散乱係数，吸収係数，消散係数などを測定するのに必要な測器はそれまでに研究開発したものを用いました。東支那海，日本海，豆南海域，三河湾と測定した海域はかぎられてはいますが，測定値は透明度，水色の理論計算にも用い，結果の考察はその後の海の色の研究へと発展致しました。

海の色の詳細な研究には高分解能の水中分光放射計が必要です。そこで，当時わが国唯一の装置であった北海道大学水産学部の回折格子分光器を用いた水中分光放射計をお借りして，この装置で豆南海域，日本海，三河湾で各層の分光放射照度の測定を行ない，海中光の色と水色を C.I.E. 表色系で求めました。

水色とは海面直上から見た海の色で，水色の測定には古くからフォーレルとウーレの水色計が用いられています。そこで，フォーレルとウーレの水色標準液の色を C.I.E. 表色系で求め，これと現場で測定した分光放射照度から求めた水色とを比較検討しました。その結果，フォーレル水色計の色は現場の分光測定から求めた水色とかなり良く一致するが，ウーレ水色計の方は高番号の標準液で色の分離が悪く，標準液の入っているアンプルを見る目の位置に十分注意しないと二つないし三つの水色番号の標準液が同一の色に見えることがわかりました。また，ウーレの標準液の明るさと現場の海の明るさにはかなりの差があって，このことが水色計による水色と現場の分光測定から求めた水色が異る原因の一つになることもわかりました。

海面直上から見た海の色は海面からの反射光によってあまり影響されないと考えると，海中に入射した太陽と空からの光が，海中の懸濁粒子や水分子によって後方に散乱されて再び空気中に戻って来たとき，どのようなスペクトル組成になっているかによって海の色は定まります。海中を透過する光は水分子，鉱物質やプランクトンとその分解物などの懸濁粒子，海水中の溶存物質の吸収と散乱によって減衰します。したがって，これらの物質の質と量によって海中光のスペクトル組成はさまざまに変化して海の色を変えていることが考えられます。そこで，懸濁物や溶存物質の光学特性と濃度の関係をモデル化して，幾種類かの海水の光学的性質のモデルを作り，このモデルについて海の色のスペクトルの理論計算を行ない，懸濁物や溶存物質の濃度によって海の色の主波長がどのように変化するかを調べました。海の色の主波長は植物プランクトンのもつクロロフィルの濃度と黄色物質と呼ばれている溶存物質の濃度が増すと，短波長より次第に長波長側に移って行きます。このことから，外洋の青い海から沿岸の緑の

海に色が変わるのは植物プランクトンや溶存物が増加するためであることは明らかです。クロロフィルの濃度が 50 mg/m^3 ぐらいになると海中から空気中に出て来る光が海面反射光に比べて小さくなるために，海の色の測定結果に海面反射光の影響を無視することができなくなることもわかりました。

近年，航空機や人工衛星による海の色のリモートセンシングによって，海中のクロロフィル量や懸濁物の濃度を求めようとする研究が諸外国において活発に行なわれています。前記した海面直上の海の色のスペクトルとクロロフィルや溶存物質の濃度の関係は，高々度から行なう海の色のリモートセンシングの基礎資料として活用することができます。私達は種々の海域で懸濁物，溶存物質の光学特性を調べ，海の色のリモートセンシングの問題に適用すべく更に研究を進めています。

お　知　ら　せ

本学会が協賛団体の一員となっている講演会が下記の通り開かれますのでお知らせします。

理化学研究所科学講演会

日　時　昭和55年10月30日（木）　13時開場，13時20分開会
場　所　経団連会館　14階ホール（東京都千代田区大手町）
後　援　科学技術庁
協　賛　関連学・協会

	予定時刻
挨　拶	(13:20～13:40)
	宮島龍興（理事長）
計算機による数式処理とその応用	(13:40～14:40)
	後藤英一（主任研究員）
分子設計 分子の構造と機能はどこまで解明されたか	(14:40～15:40)
	長倉三郎（主任研究員）
光合成と生命	(16:00～17:00)
	柴田和雄（招聘研究員）

聴講無料

連絡先　〒351　埼玉県和光市広沢2-1
理化学研究所　普及部
Tel. 0484-62-1111 内線 2362

学 会 記 事

1. 昭和55年5月28日，東京水産大学において編集委員会が開かれ，第18巻第3号の編集を行った。

2. 昭和55年5月28日，東京水産大学において評議員会が開かれた。
   1) 会務報告，編集報告が行われた。
   2) 昭和54年度の収支決算および昭和55年度の予算案が審議された。
   3) 学会賞受賞候補者として岡見登氏が推薦され，受賞者として決定された経過が報告された。
   4) 役員および編集委員の選出が行われた。
   5) 昭和55年度学会賞受賞候補者推薦委員15名を下記の通り選出した。
   阿部友三郎，有賀祐勝，石野 誠，井上 実，宇野寛，岡見 登，草下孝也，斎藤泰一，星野通平，多賀信夫，高野健三，根本敬久，松生 洽，丸茂隆三，森田良美
   6) 会則第4条に基づく分科会として日仏海洋協力機構部会を設けることが決定され，西村実氏を部会長とすることが承認された。
   7) 本学会創立20周年記念事業を行うこととし，同記念事業委員会を発足させることが決まった。
   8) 学会誌の1論文あたりの印刷制限ページ数を10ページにあらためること，および1号あたりの単価を第18巻第3号から1,200円とすることが承認された。

3. 昭和55年5月30日，日仏会館会議室において第21回総会が開かれ，次の報告並びに審議が行われた。
   1) 昭和54年度の会務並びに会計報告が行われた。なお，別表の収支決算が承認された。
   2) 編集委員長(代理)から，学会誌第17巻の編集経過報告が行われた。第17巻は総ページ数231ページで，その内訳は原著論文24篇(和文13，英文10)，資料1篇，記念講演1篇，寄稿1篇，雑録1篇，その他学会記事などである。
   3) 学会賞受賞者として岡見登氏が決定に至る経過が報告された。
   4) 昭和55年度予算案について審議の結果，別表の通り承認された。これと関連して，会費値上げについて審議の結果，正会員会費を年額 4,500円，賛助会員会費を1口年額 10,000 円とすることが承認された。
   5) 昭和55，56年度の評議員が選出された。

昭和54年度収支決算

収　入

事　項	決算額(円)	備　考
前年度繰越金	15,990	
会　費	1,370,800	
賛助会費	535,000	
学会誌売上	139,220	
広告料	189,900	
計	2,250,910	

支　出

事　項	決算額(円)	備　考
学会誌等印刷費	1,969,400	
送料通信費	183,370	
編集費	4,000	
事務費	19,700	
交通費	10,000	
会議費	63,890	
次年度繰越金	550	
計	2,250,910	

昭和55年度収支予算

収　入

事　項	予算額(円)	備　考
前年度繰越金	550	
会　費	1,755,000	
賛助会費	700,000	
学会誌売上	140,000	
広告料	480,000	
計	3,075,550	

支　出

事　項	予算額(円)	備　考
学会誌等印刷費	2,070,000	
送料通信費	200,000	
編集費	20,000	

事	務	費	500,000
交	通	費	40,000
会	議	費	60,000
予	備	費	185,550
	計		3,075,550

また，常任幹事，庶務幹事，編集幹事，幹事，監事が承認された。（いずれも本誌159ページの役員名簿を参照）

6) 編集委員長および編集委員が承認された。（本誌表紙裏の編集委員会名簿を参照）

7) 創立20周年記念事業委員会委員長および委員が次の通り承認された。

委員長: 久保田　穰

委員: 阿部友三郎，有賀祐勝，石野　誠，井上　実，岩崎秀人，岩下光男，宇野　寛，岡部史郎，岡見登，加藤重一，川原田　裕，草下孝也，西條八束，関　文威，高木和徳，高野健三，高橋　正，田畑忠司，辻田時美，冨永政英，奈須敬二，樋口明生，深瀬　茂，淵　秀隆，増田辰良，松生　洽，丸茂隆三，三浦昭雄，森川吉郎，柳川三郎，山中鷹之助

8) 分科会「日仏海洋協力機構部会」の設立について報告があった。

4. 総会終了後，引続き学会賞の授与が行われた。

昭和55年度学会賞受賞者: 岡見　登氏(理化学研究所)
受賞課題: 海洋光学に関する一連の研究（別項「推薦理由書」参照)。会長から岡見氏に賞状，メダルおよび賞金が授与され，続いて受賞記念講演が行われた。

5. 講演終了後，懇親会が開かれ盛会であった。

6. 昭和55年5月30日，日仏会館会議室において昭和55年度日仏海洋学会学術研究発表会が次の通り開かれた。

プ　ロ　グ　ラ　ム

午前の部

1. 海水の泡沫性―その経時変化について―
 ………………阿部友三郎，○森　幹樹(東理大・理)
2. Water Table に関する一考察
 …阿部友三郎，山本秀行，○新井正一(東理大・理)
3. 打ち上げ波の挙動 (2)
 ………………阿部友三郎，○山本秀行(東理大・理)
4. Slick 生成の一機構―風による表面膜の挙動実験
 ………………阿部友三郎，○高山晴光(東理大・理)
5. 固定波面上の流れの特性
 ………………阿部友三郎，○中島光雄(東理大・理)
6. 浮防波堤の消波効果に関する実験的研究
 ―重連ポンツーンの場合
 ………………………加藤重一，○土屋　達(東水大)
7. 海水中の濁度構成物質の光学的特性とそのモデル化の研究…竹松　伸，岸野元彰，岡見　登(理研)
8. 魚類の視力と水中の濁りとの関係
 ………………………○島津仁一，松生　洽(東水大)

午後の部

9. 中部北西太平洋の深層水……須藤英雄(東海区水研)
10. 北浦の帆曳網に関する研究　1. 帆曳網漁法
 ……R. LeBrasseur，岩見啓夫，
 ○関　文威(筑波大・生科系)，浜田篤信(茨城水試)
11. 北浦の帆曳網に関する研究　2. 帆曳網漁業の変遷
 ……関　文威，岩見啓夫，○R. LeBrasseur
 (筑波大・生科系)，浜田篤信(茨城水試)
12. 北浦の帆曳網に関する研究 3. 帆曳網漁業の生物学
 …………………○岩見哲夫，阿部宗明，関口晃一，
 関　文威(筑波大・生科系)
13. スサビノリの赤色型と緑色型突然変異体の遺伝子分析結果について…○国藤恭正，三浦昭雄(東水大)
14. スサビノリの色彩変異体による自殖率の推定の試み…………○三浦昭雄，国藤恭正(東水大)
15. 伊勢湾における界面活性剤MBASの分布と赤潮………………安達六郎(三重大・水産)
16. 底生無脊椎動物幼生の運搬制限と浅海系底生生物相の局地的固有性について
 ………………………………堀越増興(東大・海洋研)
17. 太平洋およびインド洋の熱帯域で採集された有鐘繊毛虫の一新種……○谷口　旭(東北大・農)，
 羽田良禾(広島修道大)
18. 西部北太平洋における浮遊性軟体類の分布
 ……○アメリア松原(東水大)，山路　勇(新日気)，
 村野正昭(東水大)

第21回総会

学会賞授賞

学会賞受賞記念講演

海洋光学に関する一連の研究………岡見　登(理研)

7. 新入会員（正会員）

氏　名	所　　属	紹介者
服部　寛	東海大学海洋研究所	元田　茂
今脇資郎	京都大学理学部	國司秀明
COGNIE, Daniel	CNEXO	宇野　寛
前川行幸	三重大学水産実験所	有賀祐勝

小川吉夫　　筑波大学生物科学系　　市村俊英

8. 退会者

正会員：横平　弘，神吉孝信，小林　貴，日精鋼業KK（開発部）

9. 会員の住所・所属の変更

氏　名	新住所または所属
赤松英雄	〒305 茨城県筑波郡谷田部町長峰1-1 気象研究所海洋研究部
岡田　操	〒062 札幌市豊平区水車町3-5-18後藤ビル ㈱水工リサーチ
武田恵二	〒031 八戸市新井田字小久保尻1-228
関川　正	〒300-12 茨城県稲敷郡牛久町牛久3464-4
久米恒雄	〒113 東京都文京区本郷7-3-1 東京大学工学部化学工学科　第6研究室内
松本　勝	〒271 松戸市松戸3-113 松戸コープ 705
森実庸男	〒798-01 愛媛県宇和島市下波5516 愛媛県水産試験場
杉村行勇	〒305 茨城県筑波郡谷田部町長峰1-1 気象研究所地球化学研究部

10. 交換及び寄贈図書

1)	日本航海学会論文集	第 62 号
2)	航　海	第 63，64 号
3)	研究実用化報告	Vol. 29 No. 3, 4
4)	鯨研通信	第 334，335 号
5)	英国産業ニュース	5，6月号
6)	水産養殖	Vol. 2 No. 3
7)	海洋時報	第 17 号
8)	海洋学報	Vol. 1 No. 1
9)	海洋文選	1978. 1
10)	農業土木試験場報告	第19，20号
11)	広島県水産試験場事業報告	昭和53年度
12)	海洋産業研究資料	Vol. 11 No. 3，4
13)	広島日仏協会報	No. 76
14)	Bulletin of the National Science Museum, Series A (Zoology)	Vol. 6 No. 1
15)	Bulletin D'Information	N° 131
16)	Science et Pêche	N° 297，298，299
17)	La gazette	N° 34
18)	Revue des Travaux de l'Institut des Pêches maritimes	Tome 17 Fasc. 1, 2
19)	Annexe a la Revue des Travaux	Tome 42 N° 1, 2
20)	Triennial Report	76-78

日仏海洋学会賞受賞候補者推薦理由書

氏　　名：岡見　登（理化学研究所）

題　　名：海洋光学に関する一連の研究

推薦理由：岡見登氏は1953年以来海洋光学に関する研究とこの研究に必要な光学的計測器の開発研究を一貫して行ない顕著な業績を上げた。論文目録にその一部を掲載したが業績は30数編にのぼる。

岡見氏が中心になって進めた海洋光学の研究は，先ず海洋光学測器の開発から始められた。水中照度計，水中輝度計，水中濁度計などは戦後諸外国に先がけて光電子増倍管を使用して電子回路を海洋測器に導入した。これらを用いて進められた水中照度・分光エネルギー分布，輝度分布，海中偏光及び海水の光学的性質などの研究は，いずれも貴重な成果であり，外国文献にもしばしば引用されている。更に海中懸濁物の光散乱現象に対してMieの理論を適用し，懸濁物の屈折率と粒径を推定する方法は，海洋光学の研究において先駆的なものであり高く評価されている。

最近は海洋環境保全や海洋開発に関連して，海の色や透明度・海の濁りについての研究を進め，成果を上げている。更に発展して海洋環境の海の色によるリモートセンシング技術の実用化の基礎として，海の色と懸濁物質や溶存物質の濃度の関係の解明に鋭意努力して居り，学会発表などでも注目を浴びている。

このように岡見登氏は現在も新しい方向への研究開拓に意欲的に取り組み，且つその業績は海洋学・水産学にとって極めて顕著であり，本委員会はこれに対して同氏を本賞の受賞者として推薦する次第である。

学会賞受賞候補者推薦委員会

委員長　松　生　　洽

主要論文・著書

原　著

1955：芦ノ湖の水中照度と水温の垂直分布について．科研報告，**31**，25.

1955：Measurement of the angular distribution of submarine daylight. Jour. Sci. Res. Inst., **49**, 103.

1955：Optical properties of the water in the Kuroshio Current. Rec. Oceanogr. Works Japan, **2**, 1.

1955：On the vertical distribution of the intensity of illumination in the water and water temperature of Lake Ashinoko. Rec. Oceanogr. Works Japan, **2**, 57.

1957：Measurements of the angular distribution of daylight in the sea. Rec. Oceanogr. Works

Japan, Special No. **1**, 42.
1957: Optical properties of the water in the Kuroshio Current (II). Rec. Oceanogr. Works Japan, **3**, 92.
1958: Spectral energy distribution of submarine daylight off Kii Peninsula. Rec. Oceanogr. Works Japan, Special No. **2**, 120.
1958: Angular distribution of daylight intensity in horizontal plane. Jour. Sci. Inst., **52**, 71.
1959: Measurements of submarine light polarization. Rec. Oceanogr. Works Japan, **5**(1), 91.
1960: Angular distribution of scattered light in deep sea water. Rec. Oceanogr. Works Japan, **5**(2) 1.
1962: Studies on suspended particles in deep sea water. Sci. Pap. Inst. Phys. Chem. Res., **37**, 77.
1968: Scattering function for deep sea water of the Kuroshio. La mer, **6**, 165.
1968: Optical properties of the water in adjacent regions of the Kuroshio. Jour. Oceanogr. Soc. Japan, **24**, 45.
1970: Examination of inorganic suspended matter in sea water by means of X-ray diffraction. La mer, **8**, 1.
1971: The distribution of suspended matter in sea water off the coast of Tokai-mura. La mer, **9**, 18.
1972: Optical properties of the water in adjacent regions of the Kuroshio (II). La mer, **10**, 89.
1975: フォーレルとウーレ水色標準液の色と海の色について．日仏海洋学会誌，**13**，172.
1977: 海の色のスペクトルについて．沿岸海洋研究ノート，**15**，56.
1979: 海水中の濁度構成物質の光学的特性とそのモデル化の研究（I）．日仏海洋学会誌．**17**，117.

資　料

1978: Measurements of spectral irradiance in the seas around the Japanese Islands. Tech. Rep. Phys. Oceanogr. Lab. IPCR, No. 2, 1.
1978: 海水の光学的特性に関する研究（その 2）―海中及び海面直上における放射輝度の伝達に関する研究．
昭和52年度　海洋遠隔探査（海洋リモートセンシング）技術の研究．研究成果集　科学技術庁研究調整局宇宙開発課 21.

著　書

1972: 海洋学講座第14巻海洋測定法．東京大学出版会，p. 107.

日仏海洋学会役員

深瀬　茂，福島久雄，淵　秀隆，星野通平，増沢譲太郎，増田辰良，松生　洽，丸茂隆三，三浦昭雄，三宅泰雄，村野正昭，元田　茂，森川吉郎，森田良美，森安茂雄，安井　正，柳川三郎，山路　勇，山中鷹之助，山中一郎，山中　一，吉田多摩夫，渡辺精一

（五十音順）

マルセル・ジュグラリス，ジャン・アンクティル，ロジェ・ペリカ

賛　助　会　員

旭化成工業株式会社	東京都千代田区有楽町 1-1-2　三井ビル
株式会社内田老鶴圃新社　内田悟	東京都千代田区九段北 1-2-1　蜂谷ビル
株式会社　オーシャン・エージ社	東京都千代田区神田美土代町 11-2　第1東英ビル
株式会社　大林組	東京都千代田区神田司町 2-3
株式会社　オセアノート	東京都千代田区平河町 1-4-3　伏見ビル
小樽舶用電機株式会社	小樽市色内町 3-4-3
株式会社　オルガノ	東京都文京区本郷 5-5-16
株式会社　海洋開発センター	東京都港区赤坂 1-9-1
社団法人　海洋産業研究会	東京都港区新橋 3-1-10　丸藤ビル
協同低温工業株式会社	東京都千代田区神田佐久間町 1-21　山伝ビル
協和商工株式会社	東京都豊島区目白 4-24-1
小松川化工機株式会社	東京都江戸川区松島 1-342
小山康三	東京都文京区本駒込 6-15-10　英和印刷社
三信船舶電具株式会社	東京都千代田区神田 1-16-8
三洋水路測量株式会社	東京都港区新橋 5-23-7　三栄ビル
シュナイダー財団極東駐在事務所	東京都港区南青山 2-2-8　DF ビル
昭和電装株式会社	高松市寺井町 1079
新日本気象海洋株式会社	東京都世田谷区玉川 3-14-5
株式会社　鶴見精機	横浜市鶴見区鶴見町 1506
東亜建設工業株式会社	東京都千代田区四番町 5
株式会社　東京久栄	東京都中央区日本橋 3-1-15　久栄ビル
東京製綱繊維ロープ株式会社	東京都中央区日本橋室町 2-6　江戸ビル
株式会社　東邦電探	東京都杉並区宮前 1-8-9
中川防蝕工業株式会社	東京都千代田区神田鍛冶町 2-2-2　東京建物ビル
日本アクアラング株式会社	神奈川県厚木市温水 2229-4
日本テトラポッド株式会社	東京都港区新橋 2-1-13　新橋富士ビル9階
社団法人　日本能率協会	東京都港区芝公園 3-1-22　協立ビル
日本プレスコンクリート株式会社	東京都中央区日本橋本石町 1-4
深田サルベージ株式会社	東京都千代田区神田錦町 1-9-1　天理教ビル8階
藤田潔	東京都新宿区四谷 3-9　光明堂ビル　株式会社ビデオプロモーション
藤田峯雄	茨城県北相馬郡藤代町大字毛有 850　株式会社 中村鉄工所
フランス物産株式会社	東京都千代田区神田小川町 3-20-2　増淵ビル
古野電気株式会社	東京都中央区八重洲 4-5　藤加ビル
丸文株式会社	東京都中央区日本橋大伝馬町 2-1-1
三井海洋開発株式会社	東京都千代田区霞ケ関 3-2-5　霞ケ関ビル 3002 号室
宮本悟	東京都中央区かちどき 3-3-5　かちどきビル　㈱ 本地郷
吉野計器製作所	東京都北区西ケ原 1-14
株式会社　離合社	東京都千代田区神田鍛冶町 1-10-4
株式会社　渡部計器製作所	東京都文京区向丘 1-7-17

OCEANIS

Volume 5, 1979-80

Fasc. 1	:	Biologie des Crustacés (C. Razouls, B. Casanova); Morphologie des siphons chez les Lamellibranches (J.-M. Amouroux) ········ 35 F (Biology of Crustacea. A study of the siphons of some bivalve molluscs)
Fasc. 2	:	Nutrition des animaux marins envisagée du point de vue de la mariculture: Vertébrés (3) (G. Peres, S. Kaushik, J. Koenig, G. Zwingelstein) ········ 35 F (Nutrition of marine animals from the point of view of mariculture)
Fasc. hors-série	:	Les indicateurs de niveaux marins (Groupe Nivmer) ········ 60 F (Indicators of sea levels)
Fasc. 3	:	Comptes rendus des Journées Aquariologiques de l'Institut Océanographique (15-16 décembre 1978) (J. Arnoult, D. Terver, M. Hignette, J. Voss, M. Tassigny, R. Pourriot, J. Auffret) ········ 35 F (Workshop on aquariology)
Fasc. hors-série	:	ATP Océanographie chimique, Actes du Colloque (7-8 décembre 1978) ········ 60 F (Acts of the Symposium on chemical oceanography)
Fasc. 4	:	Les courants profonds (G. Grau, J.-R. Vanney, L. Dangeard, J.-P. Barusseau) ··· 35 F (Deep currents)
Fasc. 5	:	Osmorégulation chez les animaux euryhalins (G. Charmantier, P. Thuet, P. Payan & M. Bornancin). Ecophysiologie des milieux lagunaires (H. Boutiere, M. Amanieu, J. Ferraris & O. Guelorget) ········ 40 F (Osmoregulation in euryhaline animals. Ecophysiology in lagoons)
Fasc. 6	:	Le volcanisme sous-marin (G. Bellaiche & J.-L. Cheminee, F. Pineau, A. Lecaille, M. Selo & D. Storzer, C. Mevel, J.-N. Valette) ········ 40 F (Submarine volcanism)

Volumes 1, 2, 3, 4 (1975-1978)
Fascicules disponibles. Demander la liste complète à

OCEANIS
Institut Océanographique
195, rue Saint-Jacques
75005 PARIS

昭和 55 年 8 月 25 日 印刷　　うみ　　第 18 巻
昭和 55 年 8 月 28 日 発行　　　　　　第 3 号

定価 ¥ 1,200

編集者　冨　永　政　英
発行者　佐　々　木　忠　義
発行所　日　仏　海　洋　学　会
財団法人 日仏会館内
東京都千代田区神田駿河台2-3
郵便番号:1 0 1
電話 : 03 (291) 1 1 4 1
振替番号:東京 9 6 5 0 3

印刷者　小　山　康　三
印刷所　英　和　印　刷　社
東京都文京区本駒込 6-15-10
郵便番号:1 1 3
電話 : 03 (941) 6 5 0 0

第 18 巻　第 3 号

目　次

Tome 18　N° 3

SOMMAIRE